Influence of Waves on Air-Sea Transfers of Energy and Momentum

Dissertation

zur Erlangung des Doktorgrades

an der Fakultät für Mathematik, Informatik und Naturwissenschaften

Fachbereich Erdsystemwissenschaften

der Universität Hamburg

vorgelegt von

Janina Tenhaus

Hamburg, 2025

Fachbereich Erdsystemwissenschaften

Datum der Disputation:	08.07.2025
Gutachter der Dissertation:	Prof. Dr. Carsten Eden Dr. Marc P. Buckley
Zusammensetzung der Prüfungskommission:	Prof. Dr. Carsten Eden Prof. Dr. Juan Pedro Mellado González Dr. Marc P. Buckley Dr. Martin Gade Prof. Dr. Babette de Wolff
Vorsitzender des Fach-Promotionsausschusses Erdsystemwissenschaften:	Prof. Dr. Hermann Held
Dekan der Fakultät MIN:	Prof. Dr.-Ing. Norbert Ritter

Eidesstattliche Versicherung | Declaration on Oath

Hiermit erkläre ich an Eides statt, dass ich die vorliegende Dissertationsschrift selbst verfasst und keine anderen als die angegebenen Quellen und Hilfsmittel benutzt habe. Sofern im Zuge der Erstellung der vorliegenden Dissertationsschrift generative Künstliche Intelligenz (gKI) basierte elektronische Hilfsmittel verwendet wurden, versichere ich, dass meine eigene Leistung im Vordergrund stand und dass eine vollständige Dokumentation aller verwendeten Hilfsmittel gemäß der Guten wissenschaftlichen Praxis vorliegt. Ich trage die Verantwortung für eventuell durch die gKI generierte fehlerhafte oder verzerrte Inhalte, fehlerhafte Referenzen, Verstöße gegen das Datenschutz- und Urheberrecht oder Plagiate.

Bielefeld, 01.04.2025

Abstract

Small-scale, coupled wind-wave dynamics within the atmosphere-ocean boundary layer control energy and momentum fluxes across the air-water interface. To date, these complex physical interactions between wind and waves remain poorly understood.

The present work aims to provide a better understanding through two experimental studies: novel high-resolution in-situ airflow observations, and velocity measurements within the first micrometers to centimeters above and below laboratory surface gravity waves, both using the particle image velocimetry (PIV) technique.

A remotely operated, large-field-of-view PIV system was installed on a single pile platform in the Odra Lagoon, Germany. We observe modulations of the airflow by locally generated wind waves, including sheltered regions downwind of wave crests, where the wind speed is reduced, for a wave age $c_p/u_* = 14.16$, where c_p is the peak wave phase speed and u_* is the air friction velocity. After averaging all instantaneous velocity fields, we find direct evidence of a critical layer, where the wind speed equals the wave speed, and the wave-coherent vertical velocity is phase shifted. The shape and phase of the vertical velocity eigenfunction show partial agreement with linear wave growth theory. In addition, the estimated dimensionless wave growth rate using different approaches is in agreement with previous studies.

Using a combination of high-resolution PIV and large-field-of-view laser-induced fluorescence (LIF) measurements at the University of Miami's SUSTAIN air-sea interaction facility, we are able to resolve viscous stresses above and below wind-generated waves. Strong along-wave modulations of both the air-side and water-side viscous stresses are directly observed for a young wave age $c_p/u_* = 1.92$. On the air side, the modulation exhibits a clear horizontal asymmetry accompanied by an increase in the standard deviation past the wave crest, caused by airflow separation events. In contrast, the water-side phase-averaged viscous stress shows less asymmetry and the standard deviation peaks just at the crest, a possible result of microscale wave breaking. We further focus on the influence of individual wave slopes on the viscous and turbulent stresses. For steep instantaneous waves, we observe airflow separation and increased turbulence for both sides of the air-water interface, which occurs in concert with a dramatic drop in viscous stress below zero. With increasing wave slope, we observe important changes in the relative contributions of viscous stress to both wave growth and surface current generation (wind drift). While viscous stress has a dominant contribution to surface currents in flat wave conditions, it contributes mostly to wave growth as waves steepen. However, this contribution remains very small. The relative contribution of viscous stress to wave growth decreases with increasing wave slope, while that of form (pressure) stress increases.

Zusammenfassung

Die kleinskalige, gekoppelte Wind-Wellen-Dynamik in der Atmosphäre-Ozean-Grenzschicht bestimmt die Energie- und Impulsübertragung an der Wasseroberfläche. Diese komplexen physikalischen Wechselwirkungen zwischen Wind und Wellen sind bisher nur unzureichend erforscht.

Die vorliegende Arbeit soll durch zwei experimentelle Studien zu einem besseren Verständnis beitragen. Dazu werden neuartige hochauflösende in-situ Luftströmungsmessungen und Geschwindigkeitsmessungen in den ersten Mikrometern bis Zentimetern ober- und unterhalb von Schwerewellen in einem Wind-Wellenkanal durchgeführt, beides unter Verwendung der Particle Image Velocimetry (PIV) Technik.

Ein ferngesteuertes PIV-System mit großem Sichtfeld wurde an einem Pfahl im Oderhaff, Deutschland, installiert. Wir beobachten Modulationen der Luftströmung durch lokal erzeugte Windwellen, einschließlich Bereiche im Windschatten der Wellenberge, in denen die Windgeschwindigkeit verringert ist, für ein Wellenalter $c_p/u_* = 14{,}16$, wobei c_p die maximale Wellenphasengeschwindigkeit und u_* die Luftreibungsgeschwindigkeit ist. Nach Mittelung aller momentanen Geschwindigkeitsfelder finden wir direkte Hinweise auf eine kritische Grenzschicht, in der die Windgeschwindigkeit der Wellengeschwindigkeit entspricht und die wellenkohärente Vertikalgeschwindigkeit phasenverschoben ist. Form und Phase der vertikalen Geschwindigkeits-Eigenfunktion stimmen teilweise mit der linearen Wellenwachstumstheorie überein. Außerdem entspricht die dimensionslose Wellenwachstumsrate, die mit verschiedenen Ansätzen berechnet wurde, den Ergebnissen früherer Studien.

Mit einer Kombination aus hochauflösenden PIV- und großflächigen laserinduzierten Fluoreszenzmessungen (LIF) in dem SUSTAIN Wind-Wellenkanal der Universität Miami konnten wir die viskosen Spannungen ober- und unterhalb windgenerierter Oberflächenwellen berechnen. Starke Modulationen der viskosen Spannungen sowohl auf der Luft- als auch auf der Wasserseite entlang der Wellen werden für ein junges Wellenalter $c_p/u_* = 1{,}92$ beobachtet. Auf der Luftseite zeigt die Modulation eine deutliche horizontale Asymmetrie, begleitet von einem Anstieg der Standardabweichung hinter dem Wellenberg, der durch Strömungsablösungen verursacht wird. Im Gegensatz dazu weist die phasengemittelte viskose Spannung auf der Wasserseite eine geringere Asymmetrie auf, und die Standardabweichung ist am Wellenberg am höchsten, was ein mögliches Ergebnis von mikroskaligen Wellenbrechen ist. Wir konzentrieren uns außerdem auf den Einfluss der einzelnen Wellensteigung auf die viskosen und turbulenten Spannungen. Bei steilen Wellen beobachten wir eine Trennung der Luftströmung und eine erhöhte Turbulenz auf beiden Seiten der Luft-Wasser-Grenzfläche, was mit einem Abfall der viskosen Spannung unter Null einhergeht. Mit zunehmender Wellensteigung zeigen sich signifikante Änderungen

in den relativen Beiträgen der viskosen Spannung sowohl zum Wellenwachstum als auch zur Erzeugung von Oberflächenströmungen. Während die viskose Spannung bei flachen Wellen einen dominanten Beitrag zur Oberflächenströmung liefert, trägt sie bei steileren Wellen hauptsächlich zum Wellenwachstum bei. Dieser Beitrag bleibt jedoch sehr gering. Der relative Beitrag der viskosen Spannung zum Wellenwachstum nimmt mit zunehmender Wellensteilheit ab, während der Beitrag der Normalspannung (Druck) zunimmt.

Mensch, das bisschen Mathe muss man zu schätzen wissen
Wer hätte damit rechnen können, auch ich will nur den letzten Bissen

Dendemann, Ich dende also bin ich.

Nomenclature

Latin Letters

a	Wave amplitude	m
c	Wave speed	m/s
D	Water depth	m
f	Frequency	Hz
g	Gravitational acceleration	m/s^2
k	Wavenumber	1/m
p	Pressure	Pa
t	Time	s
u, v, w	Horizontal, cross-tank, and vertical velocity	m/s
u_*	Friction velocity	m/s
u_d	Wind-induced drift	m/s
u_s	Surface velocity	m/s
U	Wind speed	m/s
U, W	Tangential and normal velocity	m/s
U_{10}	Wind speed at 10 m height	m/s
$\hat{w}$	Vertical eigenfunction	m/s
x, y, z	Cartesian coordinates	-
X, Z	Curvilinear coordinates	-
z_0	Roughness length	m
z_c	Critical layer height	m
z_i	Inner layer height	m

Greek Letters

β	Wave growth rate	-
γ	Surface tension	N/m
ζ	Flat surface vertical coordinate	m
η	Surface elevation	m
κ	von Kármán constant	-
λ	Wavelength	m
μ	Dynamic viscosity	kg/(ms)
ν	Kinematic viscosity	m^2/s

ρ	Density	kg/m^3
σ	Intrinsic angular frequency	1/s
τ_k	Kolmogorov time scale	s
τ_p	Particle relaxation time	s
τ_t	Turbulent stress	Pa
τ_v	Viscous stress	Pa
τ_w	Wave-coherent stress	Pa
ϕ	Phase	-
ω	Angular frequency	1/s

Indices

0	Air-water interface
a	Air
f	Flat
s	Steep
i	Control variable
$inst$	Instantaneous
m	Measured
N	Neutral
p	Peak
v	Viscous
w	Water

Abbreviations

DNS	Direct numerical simulation
LIF	Laser-induced fluorescence
NSS	Non-separated sheltering
PIV	Particle image velocimetry
PSD	Power spectral density
WBL	Wave boundary layer

Contents

1 Introduction

1.1 Motivation

In a closed system such as the atmosphere-ocean system, the total amount of energy is conserved. The vast majority of the energy input to the ocean comes from winds (~20 TW), with much smaller inputs from tides (~3.5 TW) and geothermal heating (~0.05 TW). It is not surprising, then, that the mechanical action of the wind on the wavy sea surface, and the subsequent energy dissipation through wave breaking, accounts for most of the kinetic energy in the ocean (80 %) (numbers taken from Wunsch and Ferrari (2004)). Therefore, the energy and momentum fluxes across the air-sea interface, controlled by small-scale (<O(cm)) processes, are important for the global energy budget and play an integral role in the atmosphere-ocean coupling. An incomplete understanding of their interactions reduces the predictive power of climate models. A comprehensive investigation of the turbulent boundary layer above and below ocean surface waves, the so-called wave boundary layer (WBL), is required.

Surface gravity waves are moving multi-scale undulations of the sea surface that, in the linear approximation, generally follow a dispersion relation $\omega^2 = (g + \gamma k^2/\rho)k \tanh(kD)$, where ω is the angular frequency, g is the gravitational acceleration, γ is the air-water surface tension, ρ is the water density, k is the wavenumber, and D is the water depth. Wavelengths ($\lambda = 2\pi/k$) span a range from millimeters to hundreds of meters, depending on the waves' stage of development. In deep water, the phase speed has a minimum for waves with a wavelength of 1.6 cm, which marks the transition between capillary (shorter) and gravity (longer) waves: the phase speed of gravity waves increases with their length, as opposed to capillary waves (Ayet and Chapron, 2022).

The development of ocean surface waves is usually described by the balance of wave energy E

$$\frac{\mathrm{d}E}{\mathrm{d}t} = S_{in} + S_{nl} + S_{diss} \tag{1.1}$$

where S_{in} represents the input of energy by the wind, S_{nl} are the transfers of energy

with other waves due to nonlinear wave-wave interactions, and S_{diss} (a negative quantity) is the energy dissipated by wave breaking (e.g., Komen et al., 1994; Janssen, 2008; Grare et al., 2013b). The evolution of a wave has been mathematically described by separating the sources and sinks into distinct physical processes, among them wave growth.

To date, modern parameterizations of the air-sea fluxes at the ocean surface remain insufficient because the pathways leading to the partitioning of wind energy between wave growth, wave breaking, and current generation once waves are present, are poorly understood (Sullivan and McWilliams, 2010). This is partly due to the technical challenges in observing and measuring the physics in the complex, highly dynamic two-phase flow regime. High-resolution velocity measurements within the first millimeters to centimeters of the coupled wind-wave boundary layers are required to capture small-scale turbulence and to elucidate the energy and momentum pathways at the interface.

1.2 Dissertation Overview

This dissertation investigates experimentally the influence of waves on air-sea transfers of energy and momentum. It aims to study the mechanisms of energy input S_{in} by the wind into the upper ocean through wave growth and the dynamics of microscale wave breaking. For this purpose, field and laboratory experiments were conducted using the particle image velocimetry (PIV) technique, which allows for a two-dimensional visualization and quantification of the velocity field with a high spatial resolution. These are documented in three research papers presented in chapters 3, 4, 5 of this thesis, respectively, which are either in preparation for submission or published.

Chapter 2 provides a general theoretical background, since the materials and methods used in this dissertation are described in detail in the three manuscripts and their supplementary materials.

Chapter 3 presents novel in-situ measurements of airflow velocities over wind-generated waves, revealing a direct observation of a critical layer in the vertical wave-coherent velocity field. Evidence is provided for, but not exclusively, Miles (1957) wave growth mechanism.

In chapter 4, instantaneous velocity fields above and below laboratory wind waves are resolved. The viscous stress at the surface sporadically drops to negative values in the event of airflow separation behind wave crests, in conjunction with increased negative turbulent stress for both the air and water sides.

Chapter 5 focuses on the influence of individual wave slopes on the viscous and turbulent stresses above laboratory wind waves, using the same dataset as in chapter 4. We divide waves into groups characterized by the wave slope, and the role of viscous stress in the development of waves and surface currents is examined for flat and steep waves.

Chapter 6 summarizes the scientific findings presented throughout this disserta-

tion, and provides an outlook for future work.

2

Theoretical Background

Surface gravity waves are primarily generated by form stress from airflow over deformations of the water surface, and subsequently dissipate by wave breaking, which transports momentum, energy, and bubbles into the ocean (Sullivan and McWilliams, 2010). The description of the local equilibrium of wind waves with the near-surface turbulence is at the core of parameterizations of air-sea fluxes used in numerical models, including the wind-input (wave growth) and dissipation (wave breaking) terms (Komen et al., 1994; Janssen, 2008; Ayet and Chapron, 2022). In recent years, experimental studies have employed a number of novel techniques and methods to provide a better quantification and understanding of air-sea energy and momentum fluxes that models attempt to reproduce, but some of the observed variability remains unexplained (Ayet and Chapron, 2022).

2.1 Energy and Momentum Input by Wave Growth

The wave boundary layer (WBL) is assumed to be a constant momentum flux layer $\tau(z) = \rho {u_*}^2 = const$, where u_* is the friction velocity, so the mean (averaged over turbulent fluctuations) horizontal velocity as a function of the vertical coordinate $U(z)$ is logarithmic. This assumption of the wind profile is often used in parametrizations (e.g., Janssen and Bidlot, 2023). At low wind speeds, the profile follows the *law of the wall* for turbulent flows above flat, solid, smooth surfaces with a distinct viscous sublayer, buffer, and logarithmic layers. Over the ocean, however, the presence of surface waves influences the structure and dynamics of the atmospheric boundary layer (Belcher and Hunt, 1993), and the aerodynamic roughness of the airflow increases with increasing wind speed (Buckley et al., 2020). The log-law over a rough surface can then be written as (e.g., Kundu and Cohen, 2008)

$$U(z) = \frac{u_*}{\kappa} \ln \frac{z}{z_0} \tag{2.1}$$

where κ is the *von Kármán constant*, z is the distance from the unperturbed air-water interface, and z_0 is the ocean roughness scale, a fitted parameter of O(mm).

The roughness Reynolds number Re_r, sometimes referred to as wall-normalized roughness length z_0^+, describes the dimensionless ratio of the inertial force to the viscous force and therefore the origin of turbulence. It is given by

$$Re_r = \frac{u_* z_0}{\nu} \tag{2.2}$$

where ν is the air kinematic viscosity. According to Kitaigorodskii and Donelan (1984), the ocean surface can be described as smooth when $Re_r \sim 0.1$, transitional when $0.1 < Re_r < 2.2$, and fully rough when $Re_r > 2.2$. In rough flow conditions, the airflow rather separates from the waves, and hence the surface roughness increases in such a way that the roughness elements, on average, extend outside the viscous sublayer, so that the outer flow is perturbed (Yousefi et al., 2020; Buckley et al., 2020).

In the presence of ocean waves, an instantaneous quantity q_{inst} near the wavy interface, for example the streamwise velocity u or vertical velocity w, can be decomposed into a phase-averaged component $\langle q \rangle$, which is the sum of a phase-independent mean $\bar{q}$ and a wave-coherent part $\tilde{q}$, and a turbulent perturbation q'_{inst} (e.g., Phillips, 1977)

$$\begin{aligned} q_{inst} &= \langle q \rangle + q'_{inst} \\ &= \bar{q} + \tilde{q} + q'_{inst}. \end{aligned} \tag{2.3}$$

The existence of wave-induced motions and of an undulating surface has important consequences on the momentum balance of the mean flow (Ayet and Chapron, 2022). The 2D instantaneous momentum balance can be written in Cartesian coordinates as (Buckley, 2015)

$$\frac{\partial}{\partial z}\left(\overline{u'_i w'} + \overline{\tilde{u}_i \tilde{w}} + \overline{p}\delta_{i3} - \nu\left(\frac{\partial \overline{u}_i}{\partial z} + \frac{\partial \overline{w}}{\partial x_i}\right)\right) = 0 \tag{2.4}$$

with the notation $(u_1, u_3) = (u, w)$, pressure p, and *Kronecker delta* δ. Note that for $i = 1$ the pressure term disappears ($\delta_{13} = 0$). Therefore a Cartesian curvilinear coordinate system, that follows the surface near the air-water interface and tends toward the Cartesian coordinate system away from the surface, is often used (e.g., Hara and Sullivan, 2015) to estimate the pressure-form stress.

The balance of vertical fluxes of horizontal momentum, that are relevant to the understanding and modeling of the coupled atmospheric and oceanic boundary layers, can now be decomposed into a turbulent, wave-coherent, and viscous part

$$\begin{aligned} \rho {u_*}^2 &= \tau_t + \tau_w + \tau_v \\ &= \rho\overline{u'w'} + \rho\overline{\tilde{u}\tilde{w}} + \mu\left(\frac{\partial \overline{u}}{\partial z} + \frac{\partial \overline{w}}{\partial x}\right) \end{aligned} \tag{2.5}$$

where μ is the air dynamic viscosity (e.g., Veron et al., 2007). At the top of the WBL, the momentum flux is supported entirely by turbulent stress ($\tau_w = \tau_v = 0$) and at the surface the turbulent stress vanishes and the flux is supported by wave-coherent and viscous stress (Ayet and Chapron, 2022).

A sketch of the motions within the WBL is shown in figure 2.1, including viscous and form stress acting in directions that are tangential and normal to the surface, respectively.

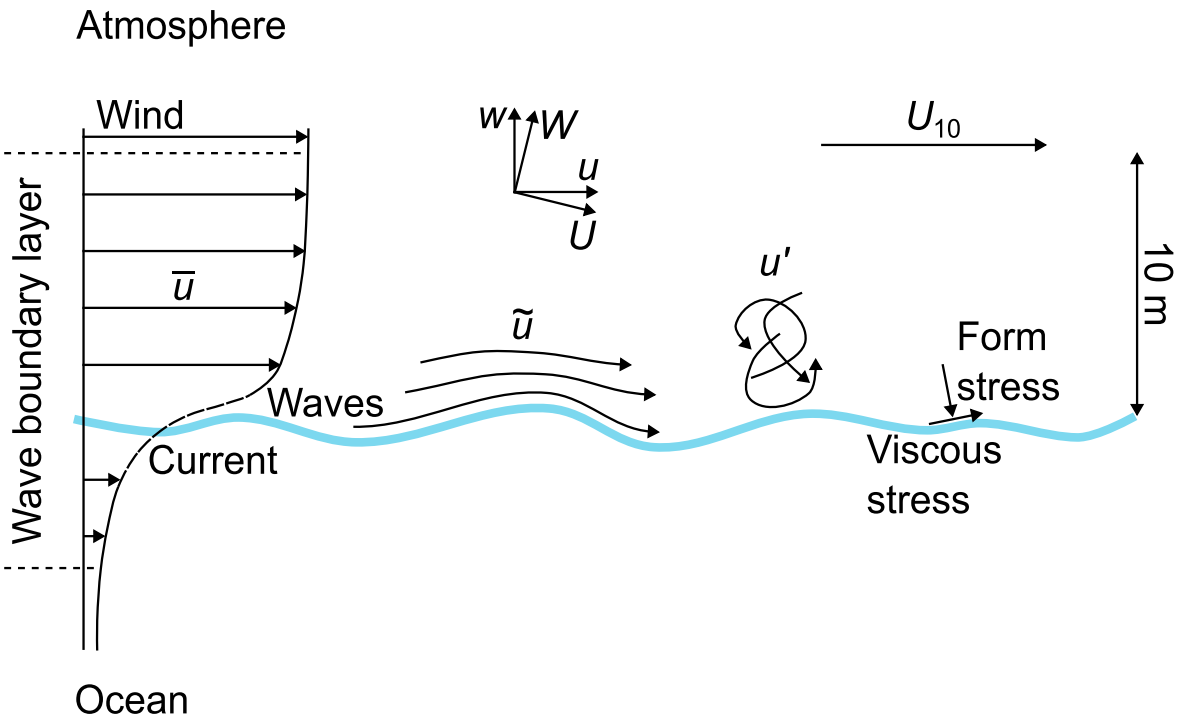

Figure 2.1: Sketch of the quantities within the region affected by the waves, which is called the wave boundary layer (WBL). Viscous and form stress are acting tangential and normal to the surface, respectively.

Equation 2.5 highlights that the impact of waves on the WBL momentum balance occurs through wave-induced stress. As an energy balance reveals, waves extract energy from the mean flow through the work of the wave-induced stress, thereby leading to wave growth (Ayet and Chapron, 2022; Bonfils et al., 2022). Wave growth is the main contribution to the air-water energy and momentum fluxes at high wave slopes, while for small wave slopes the development of surface currents under the action of surface tangential viscous stress is an important quantity as well (Buckley et al., 2020).

A century ago, Jeffreys (1925) introduced the *sheltering mechanism* according to which waves grow due to a pressure asymmetry caused by airflow separation - a reversal in the direction of airflow on the leeside of the pre-existing wave crest, leading to a pressure drop. However, the sheltering coefficient, which describes the proportionality of the aerodynamic pressure to the wave slope, had to be determined experimentally.

Phillips (1957) suggested that for an initial stage of wave growth, waves are generated by resonance between pressure fluctuations in the air and the disturbed water surface. The turbulent pressure fluctuations lead to linear wave growth

with time, as shown experimentally by Zavadsky and Shemer (2017) and recently analytically by Li and Shen (2025), as opposed to observed exponential growth rates of already formed waves (Barnett and Kenyon, 1975).

At the same time, Miles (1957) defined the problem for a later stage of wave growth using stability analysis. The principle of the *critical layer theory* is that for air flowing concurrently with the waves, there exists a critical height z_c, where the wind speed equals the wave speed c ($U(z_c) = c$). An instability occurs at the critical height, caused by the coupling of the airflow shear with the water wave so that the upward motion of the airflow over the wave induces a sinusoidal pressure variation which is balanced by a vortex force that removes energy and momentum from the wind and imparts it to the wave (Lighthill, 1962). The theory builds on the concept of resonant wind-wave interaction, using a quasi-laminar approach, where the viscous and turbulent stresses are neglected.

Belcher and Hunt (1993) argued that for short waves, when the critical height is very close to the surface, Miles (1957) inviscid theory is inappropriate, and extended Jeffreys (1925) sheltering mechanism to a turbulent airflow without separation downwind of wave crests, calling it non-separated sheltering (NSS). The *non-separated sheltering mechanism* describes the wave growth through asymmetrical streamline thinning and thickening in an inner region with depth z_i around a wave crest due to varying pressure gradients. This streamline asymmetry leads to a pressure asymmetry, with higher pressure on the upwind face of the wave, and lower pressure on the downwind face. This turbulence-driven pressure perturbation is, in turn, favorable to wave growth.

According to Belcher and Hunt (1998), wind waves can be classified into three parameter regimes, based on the wave age c/u_* or c/U_{10}, where U_{10} is the wind speed at 10 m height above the still water level, the thickness of the inner layer z_i, and the critical height z_c. For slow waves ($c/u_* \lesssim 15$), of wavenumber k, the critical layer lies within the thin inner region ($kz_i \ll 1, z_c < z_i$); for intermediate waves ($15 \lesssim c/u_* \lesssim 25$), the inner region is thick ($kz_i \sim 1$) and its depth is of the same order of magnitude as the critical height ($z_i \sim z_c$); and for fast waves ($c/u_* \gtrsim 25$), the inner region is thin ($kz_i \ll 1$) and the critical height is far above the surface ($kz_c \gg 1$). Therefore, sheltering mechanisms probably dominate the momentum transfer from wind for young and old waves, whereas the critical layer theory may be important for wave growth for intermediate wave ages (Belcher and Hunt, 1998; Grare et al., 2013a). Figure 2.2 provides a sketch of wave-growth mechanisms for these different stages.

Direct numerical simulation (DNS) results of airflow over monochromatic waves by Sullivan et al. (2000) showed that a region of closed streamlines centered around the critical height, the so-called cat's-eye pattern, is dynamically important at low to moderate values of c/u_* (3.9, 7.8, 11.5). Coherent measurements of winds and waves from the unique research platform FLIP (Floating Instrument Platform) by Hristov et al. (2003) have shown the existence of critical layers within the first few meters above ocean surface waves such that $16 < c/u_* < 40$. This was also confirmed by Grare et al. (2013a) and Grare et al. (2018). Laboratory experiments using particle

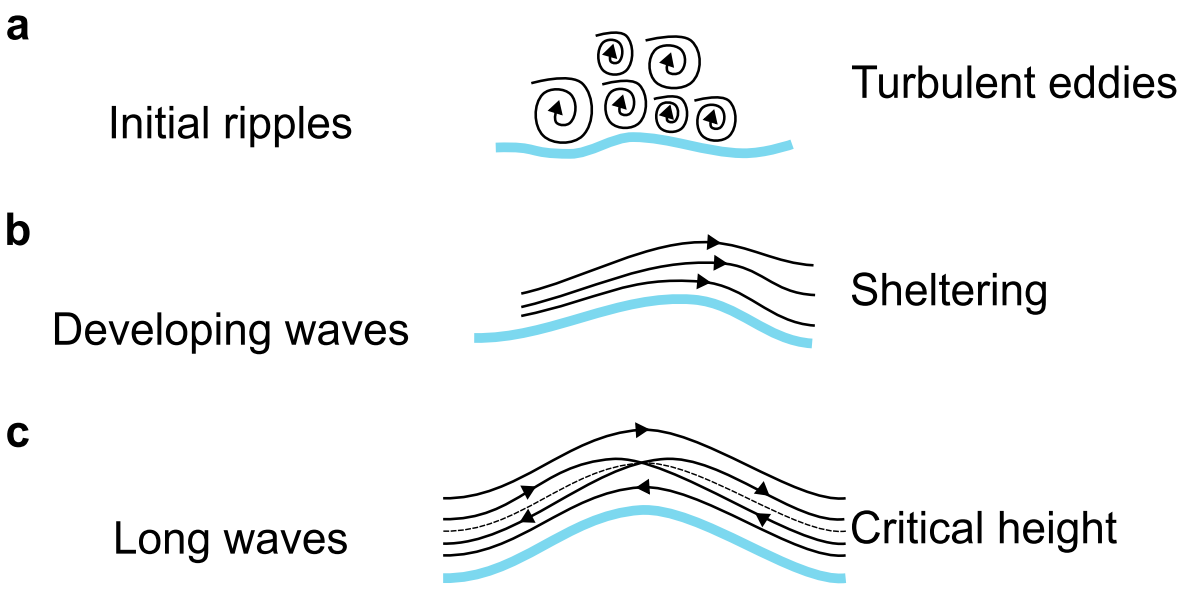

Figure 2.2: Wind-wave-generation mechanisms adapted from Pizzo et al. (2021). **a** Turbulent eddies in the air disturb an initially calm ocean and generate ripples with wavelengths on the order of centimeters (Phillips, 1957). **b** These ripples grow to meter-scale wavelengths, and the wind is sheltered on the leeward side of the wave crest. The pressure difference between the windward and leeward sides of the crest transfers energy from the wind to the wave, causing it to grow (Belcher and Hunt, 1993). **c** The wind speed increases with height above the ocean surface. An instability occurs at the critical height, where the wind speed equals the wave speed, and where a vortex force transfers energy from the wind to the wave (Miles, 1957).

image velocimetry (PIV) and laser-induced fluorescence (LIF) by Buckley and Veron (2016) acquired detailed two-dimensional wind velocity fields in a wind-wave tunnel and observed a distinct critical layer above the air-water surface for a wave age of $c/u_* = 6.3$, which was further investigated by Carpenter et al. (2022). As required by the critical layer mechanism, a significant change in both amplitude and phase of the wave-induced fluctuations crossing the critical layer was directly observed, as well as a step-like distribution of the wave-induced stress that changes sign above the critical height.

For smaller waves, the field measurements compiled by Plant (1982) provided a dependence of wave-growth rate with wave age consistent with the NSS mechanism (but with a difference in magnitude, explained by Kudryavtsev and Chapron (2016)). The Reynolds-averaged Navier-Stokes equation (RANS) numerical simulations of Mastenbroek et al. (1996), which included rapid-distortion effects, also confirmed the NSS mechanism and the vertical distribution of wave-induced perturbations of turbulent stress. Kihara et al. (2007) studied both the critical layer and the NSS mechanisms using DNS and found that the NSS mechanism dominates at wave ages of $2 \leq c/u_* \leq 4$, where the critical height is in the thin inner region, and at $c/u_* \geq 16$, where the critical height is in the outer region far above the inner region. At wave ages of $4 < c/u_* \leq 12$, the critical layer was found to be in the thick inner region

and had a strong link to momentum transfer across the interfacial wave. Recently, Tan et al. (2025) conducted co-located sampling of air pressure, airflow, and water elevation and estimated that the airflow-derived pressure based on NSS accounts for more than 90 % of the momentum transfer until potential airflow separation occurs.

2.2 Dynamics of Microscale Wave Breaking

Wave breaking is an essential component of the sea surface, associated with intense energy dissipation events from the wave field to ocean currents, but also with enhanced air-sea fluxes of heat, mass, and momentum (Melville, 1996). As a rule of thumb, about 90 % of the wave energy generated by the wind is locally lost to the ocean through wave breaking, while the remaining 10 % is either advected away or induces local growth (Janssen et al., 2001). Field measurements indicate that the wave-breaking distribution is strongly correlated with the wind speed, and hence that it can be an important parameter in the determination of the wind-wave equilibrium (Sutherland and Melville, 2013; Sutherland and Melville, 2015). Even if only a small fraction (depending on the wind speed) of the surface waves break, the impact on atmospheric turbulence is significant (Banner, 1990; Kudryavtsev et al., 2014). On the water side, intense mixing is generated within the WBL by wave breaking that extends for some distance below the water surface (Melville et al., 2002; Siddiqui and Loewen, 2007). Breaking is also responsible for generating large increases in the mean flow (Stokes drift) of the wave-affected near surface layer, which then provides a mechanism for the development of strong Langmuir circulations within the surface mixed layer (McWilliams et al., 1997). These Langmuir circulations have been found to redistribute the high turbulent kinetic energy throughout the surface mixed layer of the ocean (Sullivan et al., 2007).

Breakers can be classified into *air-entraining breaking waves*, when large scale waves (wavelengths of O(m)) break, thereby producing a whitecap due to significant air entrainment, which can be quantified, for example, from above-water images of evolving foam (e.g., Callaghan and White, 2009; Callaghan et al., 2016), and *microscale breaking waves*.

Banner and Phillips (1974) introduced the term micro-breaking to describe the breaking of short wind waves without air entrainment prevented by surface tension forces (Banner and Peregrine, 1993). Microscale breaking waves occur at low to moderate wind speeds (i.e., 4-12 m/s) and are typically O(0.1–1 m) in length, a few centimeters in amplitude, and have a bore-like crest directly preceded by parasitic capillary waves riding along the forward face (Jessup et al., 1997). On the ocean surface, microscale breaking waves occur much more frequently than large-scale breaking waves, leading to the suggestion that they may be important in controlling the flux of heat, gas, and momentum across the interface (Banner and Peregrine, 1993; Melville, 1996). This has been confirmed by two sets of laboratory wind wave experiments. Zappa et al. (2001) showed that microscale wave breaking is the physical

process that determines the gas transfer rate at low to moderate wind speeds and Siddiqui et al. (2001) found that the turbulent wakes produced by microscale breaking waves enhance air–water heat and gas transfer rates.

Banner and Phillips (1974) and Phillips and Banner (1974) argued theoretically and experimentally that incipient breaking is characterized by the occurrence of stagnation points at wave crests, while surface wind drift reduces the maximum wave height and wave orbital velocity that can be attained before breaking. Later, Banner and Melville (1976) investigated the air side and concluded that airflow separation requires a stagnation point corresponding to the onset of wave breaking, otherwise continuity of vorticity (shear) across the interface prevents the airflow from separating. A numerical model by Gent and Taylor (1977) supported the theory that airflow separation occurs only in conjunction with wave breaking or with strong near-surface underwater drift currents. Note that recently, Husain et al. (2019) found, using Large Eddy Simulations and laboratory measurements, that for strong winds, wave breaking is a sufficient but not a necessary condition for airflow separation.

Both the critical layer and the non-separated sheltering mechanisms require waves that are not steep. For steep waves, airflow separation can occur, resulting in a sharp pressure drop on the forward face of the wave in concert with a recirculating pattern (Banner and Melville, 1976; Banner, 1990; Reul et al., 1999; Reul et al., 2008). Those transient events are associated with wave slopes ak, where a is the wave amplitude, generally confined between 0.1 and 0.5, which are also often breaking waves (Melville, 1996). Kudryavtsev and Chapron (2016) showed that airflow separations from modulated breaking waves result in strong modulations of the turbulent stress in the inner region of the modulating waves. In turn, this leads to amplify the slope-correlated surface pressure anomalies. As evaluated, such a mechanism can be very efficient to enhance the wind wave growth rate by factor 2 to 3.

3

In-situ Airflow Measurements over Surface Waves using PIV

This chapter is a reprint of the manuscript *"In-situ Airflow Measurements over Surface Waves using PIV"*, which is in preparation for submission.

Citation: Tenhaus, J., Carpenter, J. R., Buckley, M. P. In-situ Airflow Measurements over Surface Waves using PIV. In preparation for submission (2025).

Key Points

- Novel in-situ measurements of airflow velocities over wind waves within the first 80 cm above the water surface
- Direct observation of a critical layer in the vertical wave-coherent velocity field
- Evidence of Miles' wave growth mechanism, but not only

3.1 Abstract

The input of wind energy by wave growth into the ocean is an important process for the global energy budget. However, observing and measuring the near-surface physics remains challenging, especially in field experiments. We captured small-scale motions in the airflow above surface waves. A high-resolution 2D particle image velocimetry (PIV) system was developed for velocity measurements within the first micrometers to centimeters above the wavy interface. The remotely operated, rotatable system was installed on a single pile platform in a lagoon at a fetch of approximately 20 to 25 km. In this study, we focus on a peak wave age (c_p/u_*) of 14.16 with a slope of 0.08 and a 10-m wind speed of 5.69 m/s. We observe modulations of the airflow by locally generated wind waves, including small sheltering events downwind of wave crests. The pattern of the vertical wave-coherent velocity field shows evidence of Miles (1957) critical layer mechanism. In addition, we find dimensionless wave growth rates using different approaches that agree with previous studies.

3.2 Plain Language Summary

Sitting in a boat watching ocean waves grow and break, you might think that these processes should be easy to study, but they are controlled by small-scale motions that are difficult to measure. Using a technique called particle image velocimetry (PIV), we measured airflow motions micrometers to centimeters over the wavy surface by imaging particles generated by fog nozzles and illuminated by a laser sheet. The system was mounted on a single pile platform in a lagoon, remotely controlled, and could be rotated to measure different wind directions. In the instantaneous 2D velocity fields obtained from the images, we observed sheltered regions in the airflow just downwind of wave crests, where the speed of the wind is reduced. After averaging all instantaneous snapshots, we directly observed a critical layer where the wind speed equals the wave speed. This layer has an important influence on the wave growth process. In addition, we calculated wave growth rates using different approaches and found that all were in general agreement with previous studies. In conclusion, we have provided evidence for an important wave growth mechanism, but we assume that it is not the only one for this wind-wave condition.

3.3 Introduction

The exchanges of energy and momentum across the air-sea interface play an important role for the global energy budget (Wunsch and Ferrari, 2004). These fluxes are strongly influenced by the small-scale, turbulent physical interactions between wind and surface waves (Sullivan and McWilliams, 2010). In spite of extensive literature on the topic, the physical coupling mechanisms between wind and waves remain, to date, not fully understood. This is partly due to the challenging nature of airflow structure observations in the immediate vicinity of the wavy water surface (Sullivan and McWilliams, 2010; Pizzo et al., 2021).

While it is generally accepted that a wind wave grows most efficiently when there is a difference in airflow pressure between the upwind and downwind faces of the wave, the physical processes that cause this pressure asymmetry remain unclear. Jeffreys (1925) introduced the sheltering mechanism, according to which, during the early stages of wind wave development, airflow separation on the leeside of waves causes the pressure perturbation. Miles (1957) generalized the problem for a later stage of wave growth using stability analysis (Bonfils et al., 2022). At the critical height, where the wind speed equals the wave speed, an instability occurs, caused by the coupling of the airflow shear with the water wave, which removes energy and momentum from the wind. Belcher and Hunt (1993) argued that for short waves, when the critical height is very close to the surface, Miles (1957) inviscid theory is inappropriate, and extended Jeffreys (1925) sheltering mechanism to a turbulent airflow, calling it non-separated sheltering. A detailed summary of the mechanisms can be found in Ayet and Chapron (2022).

The first two-dimensional airflow measurements over mechanically-generated breaking waves using particle image velocimetry (PIV) by Reul et al. (1999) and Reul et al. (2008) revealed airflow separation past wave crests. Later, Veron et al. (2007) observed a separation of the viscous sublayer from the surface past the crest of wind waves for low to moderate wind speeds. Single point air velocity measurements using a hot wire anemometer by Grare et al. (2013b) above wind waves confirmed that significant levels of viscous stress persist at moderate wind speeds. Recently, airflow measurements as low as 100 µm above the air-water interface using combined PIV and laser-induced fluorescence (LIF) for several different mechanically- and wind-generated waves by Buckley and Veron (2016), Buckley and Veron (2017), and Buckley and Veron (2019) allowed phase-averaging and triple decomposition between the mean, wave-coherent, and turbulent velocity fields. It was shown that airflow separation past young wave crests increased the average intensity of the turbulence generated by detached free shear layers, while airflow separation was rare at low wind speeds and small slopes. For a wave age of 6.3 (determined by the ratio of the peak wave speed c_p to the air friction velocity u_*, c_p/u_*), a distinct critical height above the water surface revealed Miles (1957) theory of a rapid change in flow behavior, including a reversed asymmetry in the wave-coherent vertical velocity field. Furthermore, Buckley et al. (2020) found that the viscous stress (form drag)

dominates at low (high) wave slopes, and that the tangential viscous forcing makes a minor contribution to wave growth. Lately, Funke et al. (2021) developed a pressure reconstruction technique and again found a greater influence of form drag at high wind speeds and wave slopes. Carpenter et al. (2017) and Carpenter et al. (2022) described the critical layer vorticity perturbations in a simple vortex sheet model, and compared a novel wave growth diagnostic with the laboratory observations. It was shown that Miles (1957) mechanism can cause significant wave growth in young wind-generated waves.

Measurements using a vertical array of anemometers by Hristov et al. (2003) and Grare et al. (2013a) over the open ocean from the Floating Instrument Platform (FLIP) provided evidence that Miles (1957) theory is valid for the wave age range $16 < c_p/u_* < 40$, i.e., intermediate to fast (old) waves (Belcher and Hunt, 1998). The wave-coherent velocities changed in amplitude and phase at the critical height. In addition, an upward wave-induced momentum flux was observed for older waves.

Sullivan et al. (2000) reported, using direct numerical simulation (DNS), that slow (fast) moving waves increase (decrease) the form stress. A region of closed streamlines (or cat's-eye pattern) centered about the critical layer height was found to be dynamically important at low to moderate wave ages.

Here, we present in-situ, high-resolution, two-dimensional measurements of the airflow above surface waves using PIV. We show instantaneous velocity fields capturing the rapidly changing turbulent structure. The patterns of the phase-averaged wave-coherent airflow velocity fields reveal a distinct critical layer centimeters above the water surface, and we find that the phase shift of the vertical velocity eigenfunction shows some agreement with the prediction of linear theory. In addition, we find wave growth rates using various approaches, e.g., a pressure reconstruction method, which are in agreement with previous observations compiled by Komen et al. (1994).

3.4 Experimental Methods

3.4.1 Wind and wave measurements

The measurements were obtained from a single pile observational platform, shown in figure 3.1. The platform was installed in the Odra (Szczecin) Lagoon near the Baltic Sea. A weather station (Gill MaxiMet GMX600) was mounted on the top of the pile at 10.5 m to measure wind direction and speed, as well as air temperature and relative humidity. Three-dimensional wind velocity measurements were achieved using a suite of ultrasonic anemometers (two Gill WindMaster 1590-PK-020 and one Campbell Scientific CSAT3B) installed respectively at heights of 9.8 m, 4.3 m, and 1.2 m above the mean water surface. An ultrasonic (Senix ToughSonic 50 TSPC-21S-232) and a laser (Renishaw ILM-500-R) distance sensor, mounted approximately 1.5 m above the water surface, served as single-point wave gauges. Water temperature and density were measured using a PocketFerryBox (4H-Jena Engineering, Germany), and the

mean water depth was estimated using a bottom-mounted acoustic doppler current profiler (Nortek Signature 1000). A Raspberry Pi single-board computer was used to log wind and wave measurements from the instruments (sampling frequencies: WindMaster 20 Hz, CSAT 10 Hz, MaxiMet 1 Hz, ToughSonic 10 Hz, ILM 30 Hz) (Ahlers and Buckley, 2019) day and night.

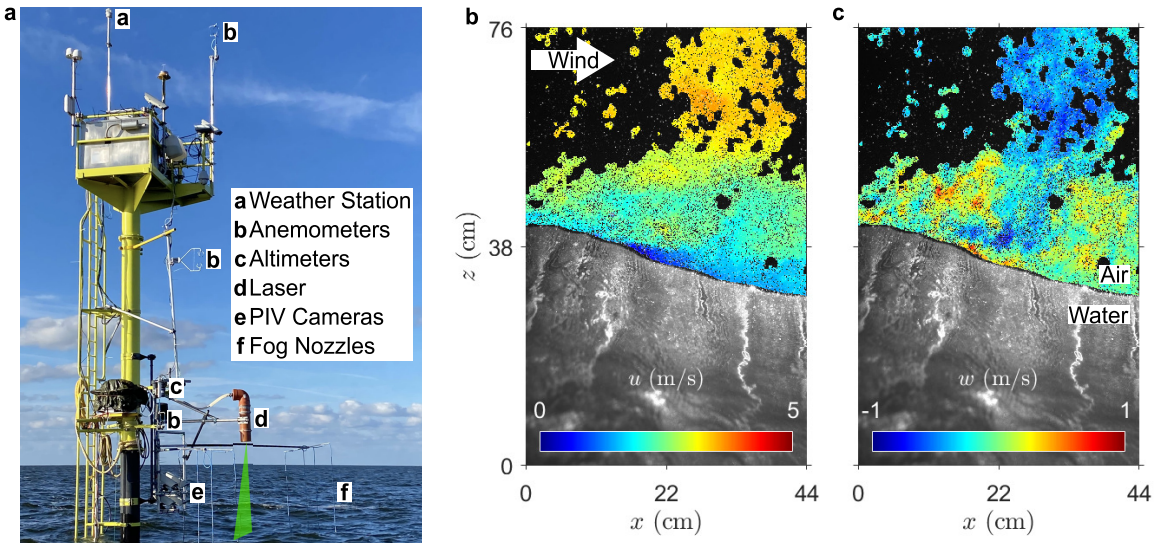

Figure 3.1: **a** Experimental set-up of the PIV system and meteorological measurements, and examples of instantaneous **b** horizontal u and **c** vertical w velocity fields. Wind and waves move from left to right. At that instant, the crest speed of this wave is approximately 1.27 m/s. Regions with no data due to insufficient seeding are shown in black.

3.4.2 PIV airflow measurements

A remote-controlled, high-resolution 2D PIV system was developed especially for this measurement campaign. The system was mounted on the pile near the water surface and had the ability to be rotated around the vertical axis, to measure the airflow velocities in a range of wind directions and fetches (20-25 km). Seeding (fog) particles (diameter 15-20 µm) were produced by pumping water from the lagoon through spray nozzles. These were illuminated by a high intensity green laser sheet generated by a pulsed Nd:YAG laser system (Quantel EverGreen EVG00200, 532 nm wavelength). The airflow tracers were imaged by four 12 MP digital cameras (IO Industries Victorem 120B68, 4112x3008 pixels, with a raw image resolution of 130 µm/px) mounted in two rows with overlapping fields of view. The cameras were tilted downward (with an angle ~ 23° from horizontal), to avoid shadowing effects from waves between the cameras and the laser sheet (Buckley and Veron, 2017). PIV image pairs were sampled at a frequency of 14 Hz.

The fog tracer particles are expected to track well the motions of the airflow, with a Stokes number of $St = \tau_p/\tau_k \ll 1$. The Stokes time scale of the largest particles is

τ_p = 1.3 ms. The Kolmogorov time scale, estimated in the bulk flow at a height of one wavelength, is 70 times larger with τ_k = 91.3 ms (Buckley and Veron, 2017).

The PIV laser and cameras were triggered by National Instruments software (LabVIEW) and hardware (PCIe 6612). In order to avoid optical noise from ambient sunlight, the PIV measurements were performed at night, with the PIV laser as the main light source. The PIV images were acquired using Streams 7 image acquisition software combined with digital video recorders (IO Industries), before being processed in MATLAB. For each run, the PIV system was rotated into the wind direction, fog was generated, and laser illumination and imaging were started.

For this study, two vertically adjacent images were stitched together by correlation (resulting in a final field of view of 3737x5775 pixels). PIV images were processed with final interrogation windows of 8x8 pixels, with 50 % window overlap, resulting in one velocity vector every 0.52 mm^2. The general processing procedure of the raw PIV images using MATLAB was: 1. project (dewarp) raw images into a vertical plane, 2. stitch adjacent images, 3. detect water surface manually, 4. mask out regions with insufficient seeding, 5. perform the PIV analysis using the PIVlab toolbox from Thielicke and Stamhuis (2014).

3.4.3 Coordinate transformation, phase detection, and decomposition

The instantaneous PIV velocity fields were mapped from a Cartesian coordinate system (x,z) to a flat surface coordinate system (x,ζ) by defining a vertical coordinate ζ that follows the wavy surface

$$\zeta = z - \eta(x, t) \tag{3.1}$$

where η is the surface elevation at time t in the plane of measurement.

Since a single PIV image may display only a fraction of the dominant wavelength, wave phases were estimated by applying Hilbert transforms to two time series of the water surface elevation, taken from the first (resp. last) 10 pixels (1.3 mm) on the upwind (resp. downwind) edge of the PIV field of view. Subsequent linear interpolation provided phase information for the entire PIV image, and allowed for wave-phase conditional averaging in 18 phase bins.

An instantaneous quantity, say q_{inst}, near the wavy interface can be decomposed into a phase-averaged component $\langle q \rangle$, which is the sum of a phase-independent mean $\bar{q}$ and a wave-coherent part $\tilde{q}$, and a turbulent perturbation q'_{inst} (Buckley and Veron, 2016)

$$\begin{aligned} q_{inst} &= \langle q \rangle + q'_{inst} \\ &= \bar{q} + \tilde{q} + q'_{inst}, \end{aligned} \tag{3.2}$$

where the subscript $inst$ stands for instantaneous. The instantaneous velocity fields obtained from the PIV analysis are decomposed accordingly to obtain wave-coherent horizontal and vertical velocities.

3.4.4 Experimental conditions

The measurements show a range of conditions, on average we find in a time interval of 105 s a wind speed at 10 m height U_{10} = 5.69 m/s and waves with an average amplitude a = 7.04 cm, significant wave height H_s = 19.92 cm, and wavelength λ = 5.53 m, giving a small slope ak_p = 0.08 with the peak wavenumber k_p. The mean water depth D was 4.1 m, such that $D/\lambda_p \sim 0.74$. More details on the experimental conditions are given in table 3.1.

A frequency analysis of the water surface elevation time series, measured by the ultrasonic altimeter, delivers an apparent (measured) peak frequency of $f_m = 0.55$ Hz. We note that the water surface elevations measured directly on the PIV images confirm this result (see the power spectral density (PSD) plots, figure 3.6).

The measured peak frequencies are Doppler shifted by the wind-induced drift u_d (Stewart and Joy, 1974; Smeltzer et al., 2019), following

$$2\pi f_m = \sigma + ku_d = k(c + u_d) \tag{3.3}$$

where σ denotes the intrinsic radial wave frequency. Using cross-spectral analysis on two adjacent optical wave gauge signals, the wind drift was estimated to be u_d = 0.09 ± 1.19 m/s and 1.6 % of U_{10} (Buckley et al., 2020; Tenhaus et al., 2024).

The peak wave age was found to be $c_p/u_* = 14.16$ ($c_p/U_{10} = 0.52$), where c_p is the peak wave speed and u_* the friction velocity. This indicates a growing, wind-driven sea state (Sullivan and McWilliams, 2010).

The water in the Odra Lagoon is mainly a mixture of Baltic Sea and Odra River water (Pein and Staneva, 2024), and is less salty than open ocean water, with a measured density of ρ_w = 1001.70 kg/m^3. Surfactants dampen the waves and affect the higher frequency components (tail) in the PSD. Nevertheless, we assume that our measurements are close to the reality in the open ocean, as we observe an airflow structure coupled to the waves.

3.5 Results and Discussion

3.5.1 Instantaneous 2D velocity fields

Instantaneous horizontal u and vertical w velocity fields resulting from the PIV analysis of one image pair as described above, are shown in figure 3.1. The airflow velocity fields are overlayed on the raw (stitched) PIV image. The water surface structure, including small capillary waves, is visible thanks to refracted laser light (Liu and Duncan, 2003; Buckley and Veron, 2016). We note that only a fraction of this wave (with a wavelength ~ 8.91 m) is captured by the PIV imaging system. Nonetheless, the horizontal velocity field shows a sheltering event past the wave crest, characterized by sharp decrease in the airflow velocity just downwind of the crest, near the surface. The vertical velocity field displays more spatial variability than the

horizontal one, with regions of upward and downward motions, in agreement with past (laboratory) observations (Buckley and Veron, 2016).

For a more complete overview of the airflow kinematics above an entire wave, 14 consecutive velocity fields are displayed side by side in figure 3.2, corresponding to 1 s of imaging. Time decreases from left to right, and wind and waves move from left to right. The horizontal wind speed is higher at the crest and lower on the windward and leeward sides of the wave. This indicates a boundary layer thinning on the crest and thickening upwind and downwind of it (Belcher and Hunt, 1998). We assume that there is a wake effect on the windward side, and that this is not the result of a sheltering event behind the following wave crest, because we observe an increase in surface speed between the two crests (not shown here). Since the measurements were taken for an intermediate wave age, we believe that this is a realistic event. For younger waves we would expect sheltering downwind of the crest, and for older waves the trend is reversed (Buckley and Veron, 2016). Here we observe both.

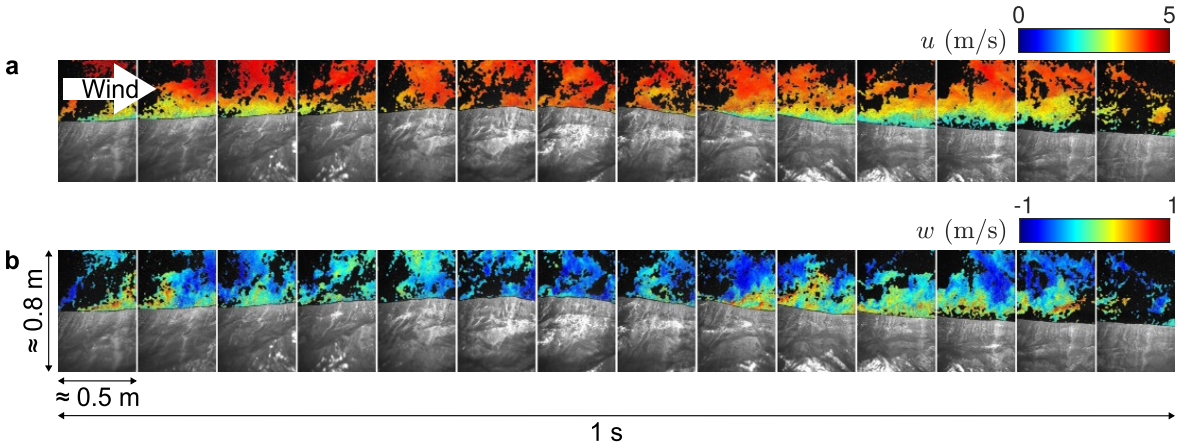

Figure 3.2: 14 snapshots of instantaneous 2D PIV **a** horizontal u and **b** vertical w airflow velocity fields, acquired over a 1 s time interval.

3.5.2 Phase-averaged velocities

Figure 3.3 shows the PIV phase-averaged wave-coherent velocities in a fixed frame of reference, obtained after subtracting the mean velocities from the phase-averaged velocities. We observe an alternating positive-negative pattern in the wave-coherent horizontal velocity field $\tilde{u}$, with increased velocities on the windward side and at wave crests, and a velocity reduction on the leeward side and at troughs. The dashed line indicates the height of the critical layer, defined as $\langle u(z_c) \rangle = c_p$.

The pattern of the wave-coherent vertical velocity $\tilde{w}$, unlike $\tilde{u}$, is not tilted downwind and remains vertical with height. It shows phase-locked characteristics: the air moves upward on positive wave slopes and downward on negative slopes. Within the critical layer the pattern is reversed, the air is forced upward on negative

wave slopes and downward on positive slopes, these motions are coherent with a forcing from underwater and following the wave orbitals.

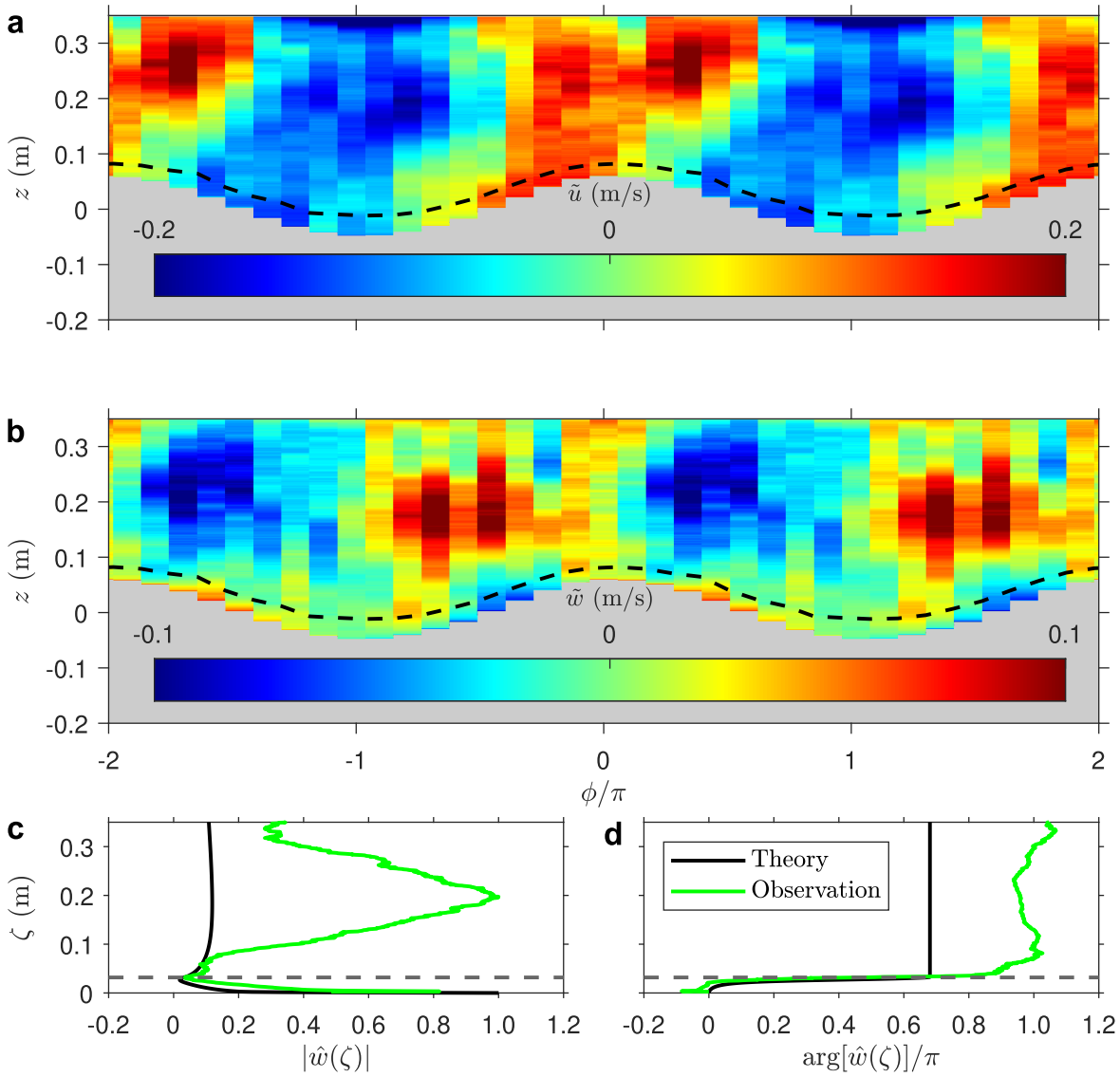

Figure 3.3: Phase-averaged wave-coherent **a** horizontal $\tilde{u}$ and **b** vertical $\tilde{w}$ velocity fields (105 s interval, 18 phase ϕ bins). **c** Amplitude and **d** phase of the vertical velocity eigenfunction $\hat{w}(\zeta)$. Dashed line indicates critical layer.

3.5.3 Comparison with recent studies and linear theory

The contours of the wave-coherent velocity fields are in good qualitative agreement with the DNS simulation results of Sullivan et al. (2000), albeit for younger waves ($c/u_* = 7.8$) but with a similar slope ($ak = 0.1$), as well as the laboratory measurements of Buckley and Veron (2016), Buckley and Veron (2017), and Buckley and Veron (2019).

The latter were compared to linear theory by Carpenter et al. (2022), for $c/u_* = 6.3$ and $ak = 0.07$, and found to be in good agreement.

In figure 3.3 the observed vertical eigenfunction, computed through the phase average by $\hat{w}(\zeta) = \int_0^{2\pi} \tilde{w}(\phi, \zeta) e^{-i\phi} \mathrm{d}\phi/\pi$, is compared with the prediction of linear theory. The linear result is found by solving the linear stability problem for the air-side, described by the Rayleigh equation

$$\hat{w}'' - \left(k^2 + \frac{U''}{U - c} \right) \hat{w} = 0 \tag{3.4}$$

coupled to a water surface boundary condition (the numerical method used follows Bonfils et al. (2023)). Here we denote the complex wave speed by c, using the measured mean wind profile U and the (peak) wavenumber k as input. We find that the shape and phase of the vertical velocity eigenfunction show partial agreement with Miles (1957) linear theory. Notably, the observed eigenfunction exhibits a rapid phase change at the critical height. However, the amplitude has a bump in it (at $\zeta \approx 0.2$ m) that is unaccounted for in the linear result, and at this height the wave-coherent momentum flux is high (not shown here). In the laboratory, Carpenter et al. (2022) found a phase shift of the vertical wave-coherent velocity of 140° for a wave age of $c/u_* = 6.3$ that was in close agreement with the linear prediction. Over the open ocean Hristov et al. (2003) observed a phase shift of 135° (resp. 90°) for $c/u_* = 12$ (resp. 19). We estimated 160-180° for $c_p/u_* = 14.16$.

The phase shift in $\hat{w}(\zeta)$ across the critical layer, which is optimal at $\pi/2$, leads to wave-coherent pressure forcing, resulting in energy transfer from wind to wave. The linear theory result above gives a dimensionless wave growth rate of $\beta_1 = 5.2 \cdot 10^{-4}$ by

$$\beta_1 = \frac{\rho_a}{\rho_w f} \operatorname{Im} \left\{ 2k \int_0^\infty \mathrm{e}^{-k\zeta} \frac{U'(\zeta)\hat{w}(\zeta)}{\hat{w}_0} \mathrm{d}\zeta \right\}, \tag{3.5}$$

where the subscript 0 represents the air-water interface, which is within the observations compiled by Komen et al. (1994), plotted in figure 3.4. However, these observations show considerable scatter of approximately one order of magnitude at these wave ages.

According to Buckley et al. (2020) and similar to Plant (1982), the dimensionless wave growth rate can also be written as

$$\beta_2 = 4\pi \frac{\rho_a}{\rho_w} \frac{\tau_w}{\rho_a u_*^2} \frac{u_*^2}{c^2} \frac{1}{(ak)^2} - 8\pi Re^{-1} \tag{3.6}$$

with the Reynolds number $Re = c/(\nu_w k)$ and expressing that the wave slope, wave age, and wave-coherent momentum flux τ_w are all essential components of the wave growth process. Using the maximum value of the wave-coherent momentum flux as input, we find $\beta_2 = 1.04 \cdot 10^{-3}$, which agrees well with the Komen et al. (1994) curve. We conclude that the departures from linear theory observed in the vertical velocity eigenfunction may have an influence on the wave growth.

Finally, we use the pressure reconstruction method described in Funke et al. (2021). The pressure p is reconstructed from the 2D phase-averaged wave-coherent velocity fields (figure 3.3, panels a and b), shown in figure 3.9. The pressure reconstruction of the phase-averaged velocity field assumes a periodic, sinusoidal water surface at the peak wavenumber with negligible velocity gradients above the PIV field of view. Viscous terms in the reconstruction have been neglected since they are expected to be small. A growth rate can be formulated based on the pressure of the airflow on the water surface (p_0) and the work it performs. This is given by

$$\beta_3 = -\frac{2}{\rho_w g a^2} \left\langle p_0 \left(w_0 - u_0 \frac{\partial \eta}{\partial x} \right) \right\rangle, \tag{3.7}$$

and found to be $\beta_3 = 3.6 \cdot 10^{-3}$. This result is close to the linear theory prediction.

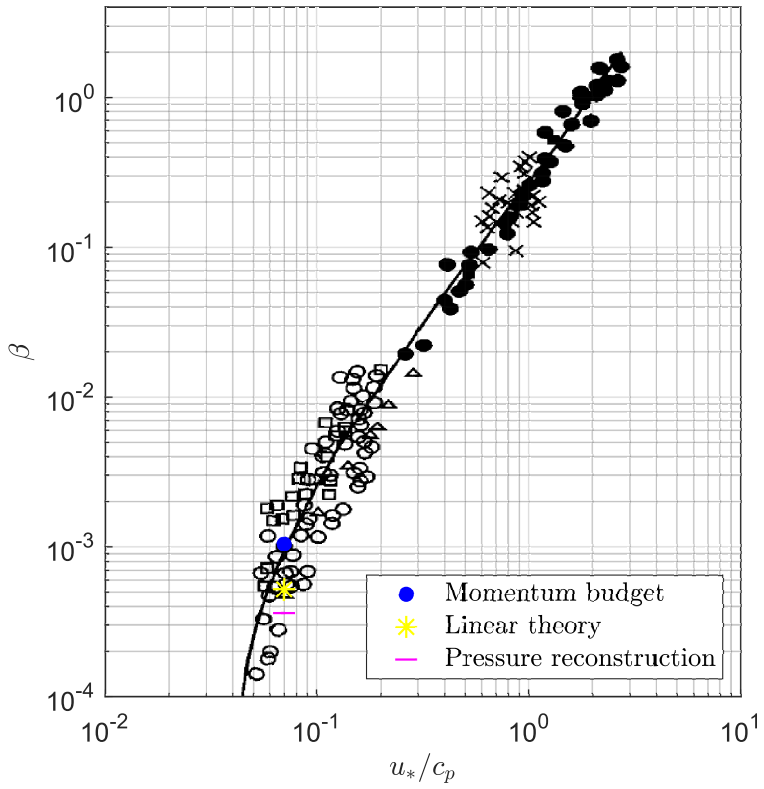

Figure 3.4: Dimensionless growth rate β for three methods is plotted onto the observations compiled by Komen et al. (1994).

3.6 Summary and Conclusions

Novel high-resolution in-situ airflow measurements over surface waves using PIV were conducted in the Odra Lagoon. In the instantaneous 2D velocity fields, we

observed sheltering events downwind of sharp wave crests. After averaging all instantaneous snapshots over one wave phase, we directly found, for the first time in the field, a critical layer where the wind speed equals the wave speed and the wave-coherent vertical velocity is phase shifted. The phase shift was compared with linear theory and showed some agreement with Miles (1957) wave growth mechanism. In addition, the dimensionless wave growth rate was estimated using three different methods and showed general consistency with previous observations. To our understanding, there must be a pressure difference to make the waves grow, the mechanism causing this asymmetry is still unclear, but it is not just Miles (1957).

Therefore, future work needs to look at different scenarios, since it is difficult to set the experimental conditions in the field, we will use two-phase flow simulations (Loft et al., 2023).

3.7 Supplementary Material

3.7.1 Detailed experimental conditions

Figure 3.5 shows the time series of wind speeds from the instruments, shown in figure 3.1 and described in subsection 3.4.1, for a 2 h period. On average, the velocity magnitudes increase with height. The two lowest anemometers, WindMaster2 and CSAT, show large fluctuations because they are most affected by the waves. Over the 2 h period, we observe a very minimal trend in the mean wind speed, suggesting that the wave field at the time and location of the measurements is fetch limited. During the processed PIV interval of 105 s, the running average of the wind speed is relatively constant. The mean wind speeds are measured by MaxiMet (10.5 m) 5.71 m/s, WindMaster1 (9.8 m) 5.71 m/s, CSAT (4.3 m) 4.88 m/s, and WindMaster2 (1.2 m) 1.95 m/s. Note that the lowest anemometer (WindMaster2) is not considered in the following as it is assumed to be in the wake of the pile for this wind direction.

A comparison of the PSD estimates of the water surface elevation time series for the 105 s period, measured with the ultrasonic altimeter (Toughsonic) and with the PIV images using the surface detection as a wave gauge, is shown in figure 3.6. These show a good agreement. They both have the same peak frequency $f_p = 0.55$ Hz. The tails of the frequency spectra follow the well-known f^{-4}-shape, that was first proposed by Toba (1973). This shows the good ability of the PIV images to serve as an optical wave gauge, with additional local water surface slope information (not shown here).

Table 3.1 provides the experimental conditions for the 105 s period.

3.7.2 Neutral wind speed, friction velocity, and roughness length

The air (from the MaxiMet weather station) and water (from FerryBox) temperatures during the day of the processed PIV interval are shown in figure 3.7. Due to technical

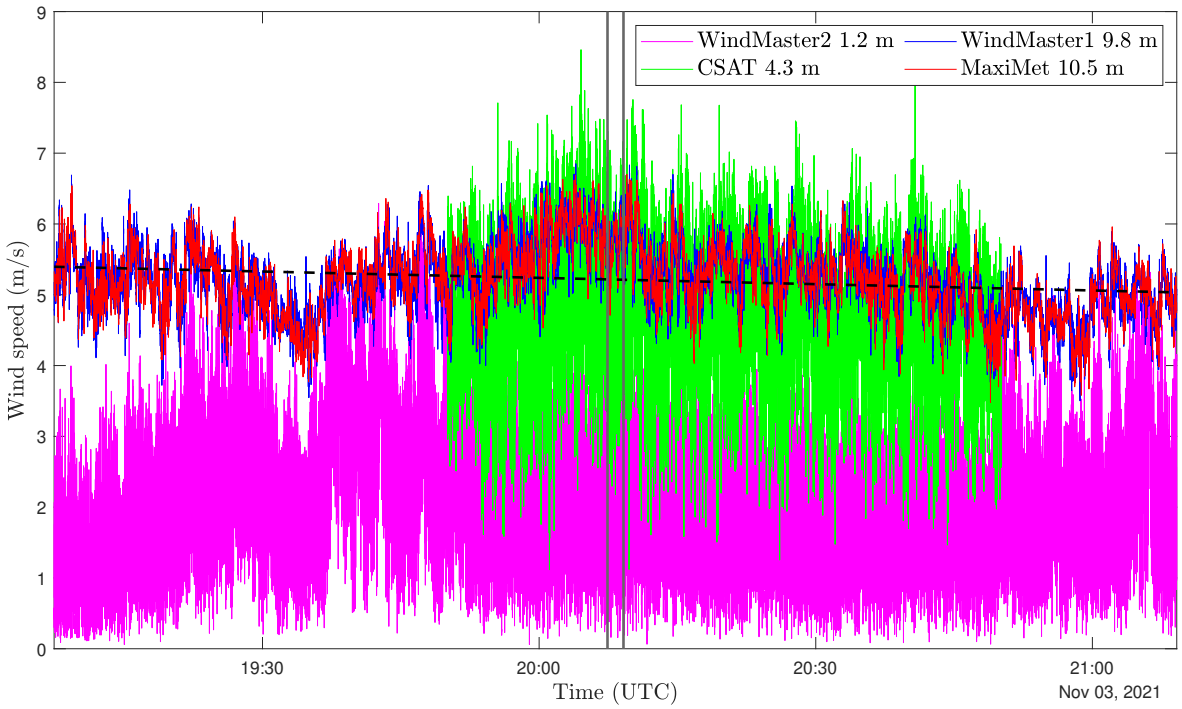

Figure 3.5: Wind speeds during a 2 h time interval from instruments mounted at different heights. Black dashed line is the linear trend of MaxiMet. Black vertical lines indicate the processed PIV interval.

issues, the water temperature measurements were stopped approximately three hours before the PIV acquisition. However, while the air temperature fluctuates during the day, the water temperature is relatively constant. Therefore, despite the lack of data, we assume that the water temperature remains constant during the PIV measurements.

Since there was a temperature difference between air (mean of 7.61°C during the 105 s PIV period) and water (mean of 9.33°C during the day), a neutral 10-m extrapolated velocity U_{N10} = 5.91 m/s was estimated for the 105 s PIV period using the COARE algorithm by Fairall et al. (2003) with the MaxiMet data, which is only

Table 3.1: Experimental conditions. The measured, apparent peak frequency f_p was obtained from the optical wave gauge frequency spectra. The intrinsic wave speed c_p and the wind drift u_d were extracted by cross-spectral analysis on two adjacent wave gauges. The wavelength λ_p and wavenumber k_p were derived by applying linear wave theory to f_p and c_p. The wave amplitude a was computed from the measured water surface elevation time series with $a = \sqrt{2}a_{rms}$. The wind speed at 10 m height U_{10} and the friction velocity u_* were calculated from the MaxiMet data using the COARE algorithm by Fairall et al. (2003).

U_{10}	u_*	f_p	c_p	u_d	λ_p	a	ak_p	c_p/u_*	c_p/U_{10}
m/s	cm/s	Hz	m/s	m/s	m	cm	-	-	-
5.69	20.75	0.55	2.94	0.09	5.53	7.04	0.08	14.16	0.52

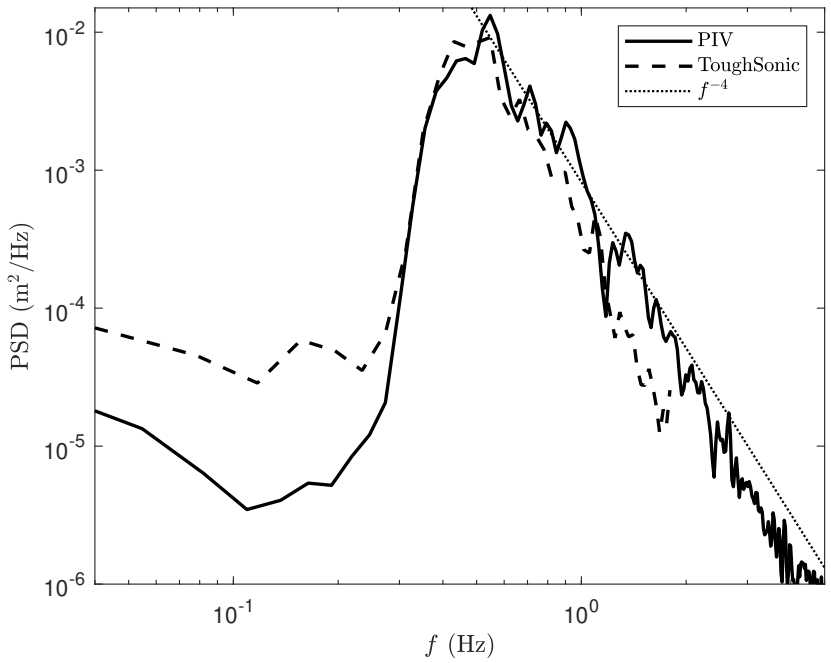

Figure 3.6: PSD estimates of water surface elevation time series measured with the ultrasonic altimeter (ToughSonic) and PIV images.

slightly higher than the non-neutral U_{10} = 5.69 m/s given in table 3.1 and was therefore neglected during processing. In addition, the friction velocity u_* and roughness length z_0 are important parameters to describe the airflow. Table 3.2 lists the results of different methods using a log-fit between two instruments or the COARE algorithm by Fairall et al. (2003) with input of wind speed and height for each anemometer, for the 105 s of sampling. The discrepancy in u_* is a result of convection due to non-neutral conditions, which is not accounted for by the log-fit method. In addition, the CSAT at 4.3 m height is assumed to be in the wave boundary layer.

Table 3.2: Neutral velocity U_{N10} at 10 m height compared to the extrapolated velocity U_{10} from measurements for a 105 s period. The friction velocity u_* and roughness length z_0 are given using different methods.

	U_{N10} m/s	U_{10} m/s	u_* cm/s	z_0 mm
log-fit CSAT MaxiMet	-	5.67	37.82	0.02
log-fit CSAT WindMaster1	-	5.72	40.57	0.03
COARE MaxiMet	5.91	5.69	20.63	0.09
COARE WindMaster1	5.93	5.71	20.69	0.09
COARE CSAT	5.34	5.10	18.42	0.08

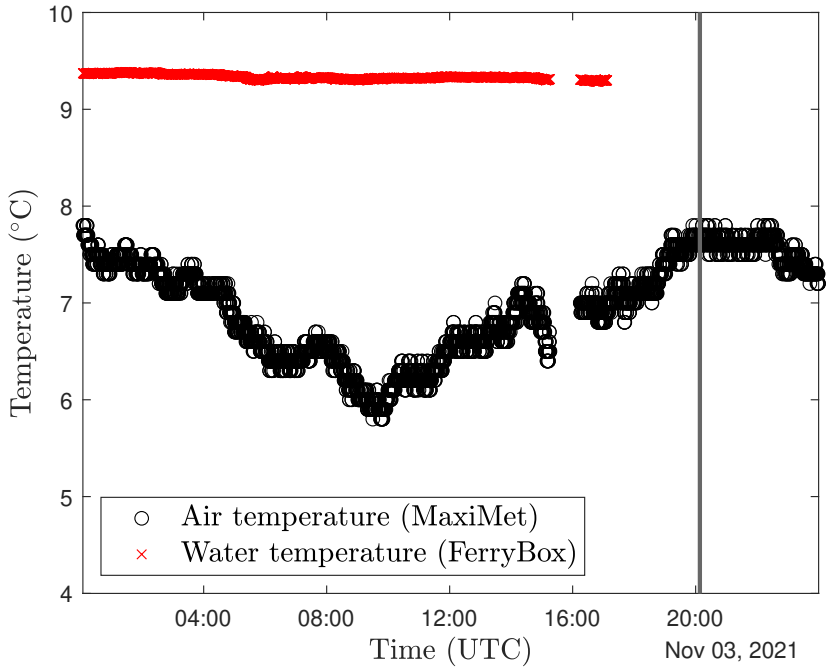

Figure 3.7: Air and water temperatures measured using a MaxiMet and a FerryBox, respectively, during a day. Black lines indicate the processed PIV interval.

3.7.3 Phase-averaged velocities

Figure 3.8 shows the PIV phase-averaged horizontal and vertical velocities in a fixed frame of reference. The horizontal velocity is higher with increasing height above the water surface. A fit of the mean horizontal profile shown in panel b is used in equations 3.4 and 3.5. The phase-averaged $\langle w \rangle$ and wave-coherent $\tilde{w}$ vertical velocities should be equal assuming that the waves are aligned with the mean wind direction and that the sampling time is sufficiently long, but we find that the mean vertical velocity $\bar{w}$ is not zero and overall negative. Using the Stokes number (calculated in subsection 3.4.2), we can assume that the fog tracer particles follow the airflow well and do not fall down. Since the mean is subtracted from the phase-averaged field, the pattern of the wave-coherent velocity field is assumed to be correct.

Note that the laser sheet was remotely rotated into the wind direction, so we cannot rule out the possibility that it was not perfectly aligned. This would result in a non-zero spanwise velocity component, not captured by the planar 2D PIV technique developed for this study.

3.7.4 Pressure reconstruction

Figure 3.9 shows the pressure field obtained using the pressure reconstruction method recently developed by Funke et al. (2021), on the 2D phase-averaged velocity fields. The pressure field is nearly in phase with the water surface elevation, but with a

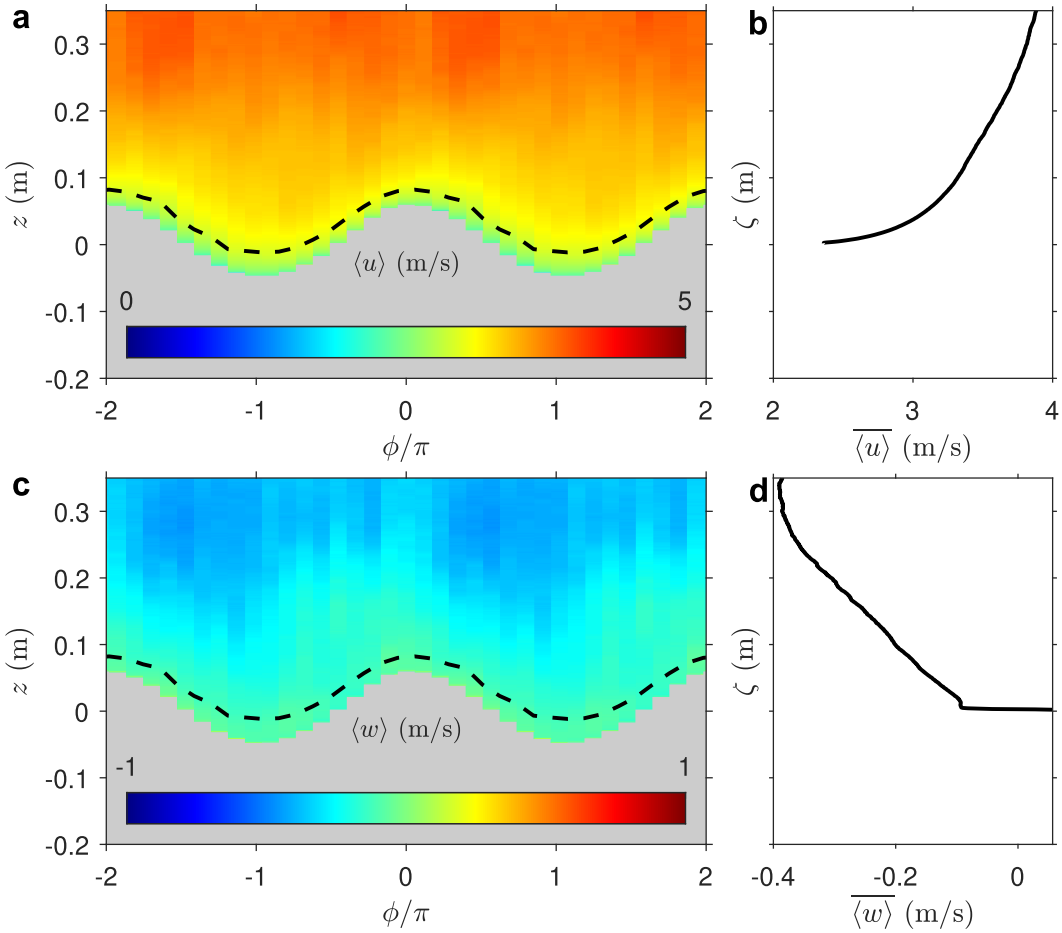

Figure 3.8: **a** Phase-averaged horizontal velocity field, **b** mean horizontal velocity, **c** phase-averaged vertical velocity field, and **d** mean vertical velocity (105 s interval, 18 phase ϕ bins). Dashed line indicates critical layer.

very slight downwind phase shift, which is favorable to wave growth. The peak wavelength is used to convert wave phases to a spatial scale.

3.7.5 Comparison to model

Figure 3.10 compares the Cahn-Hilliard Volume-of-Fluid (CH-VoF) model from Loft et al. (2023) for the horizontal wave-coherent velocity and the wave-coherent stress with the PIV measurements. The model shows the same patterns as the measurements, but with different magnitudes.

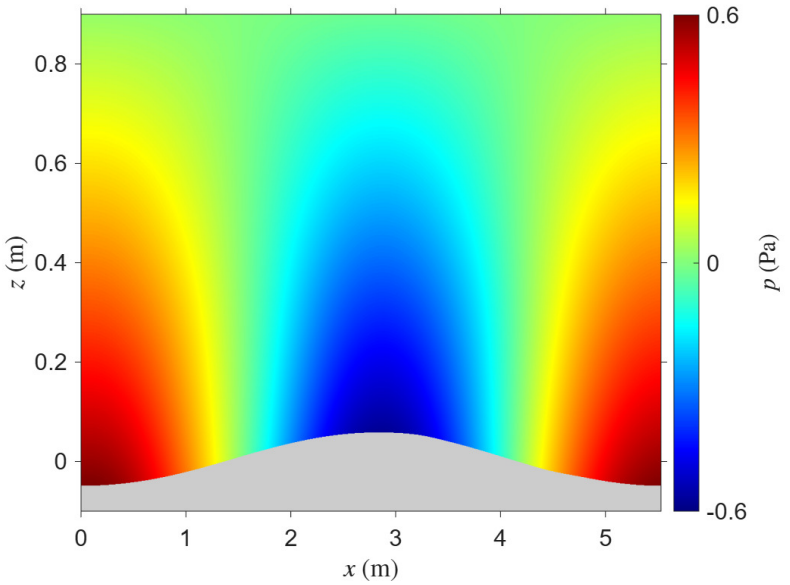

Figure 3.9: Phase-averaged pressure field plotted above the peak wavelength.

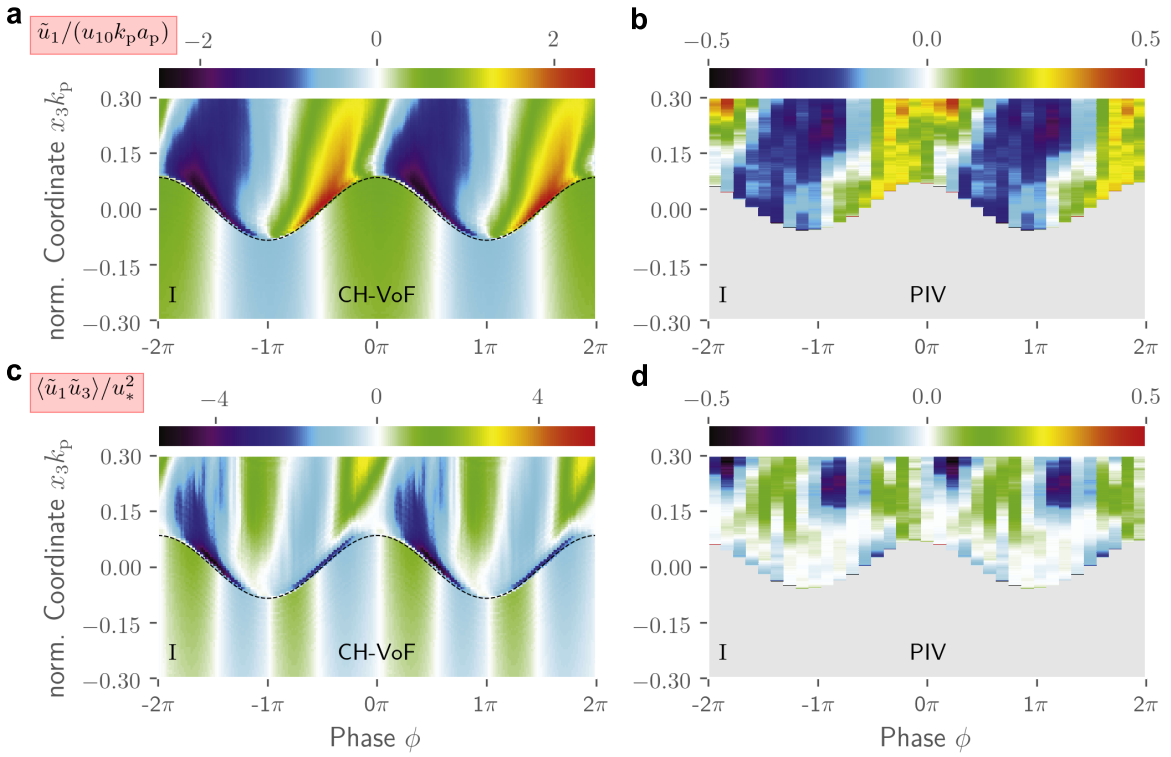

Figure 3.10: Results of CH-VoF model (**a**,**c**) and PIV measurements (**b**,**d**). **a**,**b** Normalized wave-coherent horizontal velocity. **c**,**d** Normalized wave-coherent stress.

4

Viscous and Turbulent Stress Measurements above and below Laboratory Wind Waves

This chapter is a reprint of the manuscript *"Viscous and turbulent stress measurements above and below laboratory wind waves"* published in *Experiments in Fluids*.

Minor changes have been made to the published text for the purpose of consistency throughout this dissertation.

Citation: Tenhaus, J., Buckley, M. P., Matt, S., Savelyev, I. B. Viscous and turbulent stress measurements above and below laboratory wind waves. Exp Fluids 65, 174 (2024). https://doi.org/10.1007/s00348-024-03898-7 [1]

Key Points

- Instantaneous velocity and vorticity fields are resolved within the first millimeters above and below laboratory wind waves
- Phase-averaged viscous stresses on both sides of the interface show strong along-wave modulations, with less asymmetry on the water side than on the air side
- In the event of airflow separation, the viscous stress sporadically drops to negative values and the turbulent stress is increased

4.1 Abstract

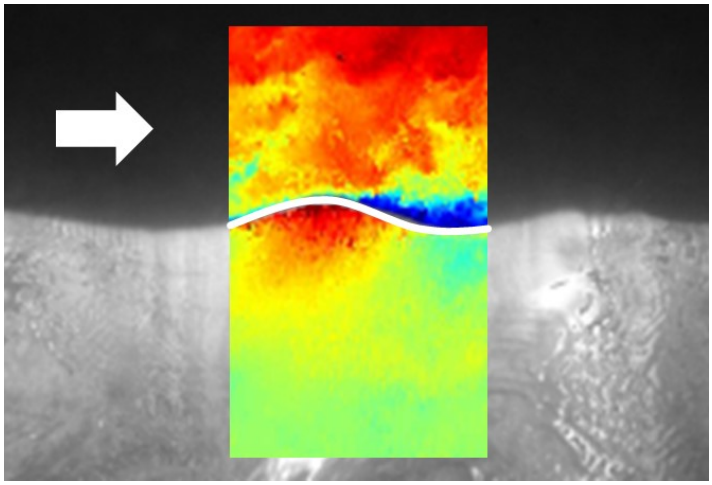

The influence of wind stress, wind drift, and wind wave (microscale) breaking on the coupled air-sea boundary layer is poorly understood. We performed high-resolution planar and stereo velocity measurements within the first micrometers to centimeters above and below surface gravity waves at the University of Miami's SUSTAIN air-sea interaction facility. A particle image velocimetry (PIV) system was adapted and installed in the large (18 m long, 6 m wide) wind-wave tunnel at a fetch of approximately 10 m. In addition, wave field properties were captured by laser-induced fluorescence (LIF). Experiments were conducted with wind waves and wind over mechanically generated swell. In this work, we focus on rather smooth, young, wind-generated waves. We present instantaneous velocity and vorticity fields above and below the air-water interface for the same wind-wave conditions. Both instantaneous and phase-averaged fields show strong along-wave modulations in viscous stress. For steeper waves, we observe airflow separation and increased negative turbulent stress below crests, accompanied by sporadic drops in viscous stress below zero. We describe the wave-induced modulations of the airflow structure

as well as the wind-induced water dynamics, and discuss the importance of the viscous stress for the total momentum budget.

4.2 Introduction

Momentum and mechanical energy exchanges across the air-sea interface are influenced by near-surface dynamics, including those within the coupled air-water viscous sublayers. The detailed structure of viscous stress and specifically its role in the development of waves and surface currents are not fully understood, due to the technically challenging nature of detailed observations in the presence of wind waves. Airflow separation and wave breaking events play an important role for the momentum flux between the atmosphere and the ocean (Sullivan and McWilliams, 2010), as they dramatically modify the structure of the wind stress, above (Buckley and Veron, 2019) and below the air-water interface. The coupling mechanisms between wind stress, wind drift, and wind wave (microscale) breaking have been a topic of interest for decades.

Banner and Phillips (1974) and Phillips and Banner (1974) argued theoretically and experimentally that incipient breaking is characterized by the occurrence of stagnation points at wave crests, while surface wind drift reduces the maximum wave height and wave orbital velocity that can be attained before breaking. Later, Banner and Melville (1976) investigated the air side and concluded that airflow separation requires a stagnation point corresponding to the onset of wave breaking. A numerical model by Gent and Taylor (1977) supported the theory that airflow separation occurs only in conjunction with wave breaking.

The roles of viscous stress and form drag for wave growth and the momentum flux into surface currents have also been the focus of a number of experimental studies. Using hydrogen bubbles as flow tracers, Okuda et al. (1977) found that the shear stress is the dominant momentum flux mechanism in very short, strongly forced wind-wave conditions. Two decades later, Peirson (1997) and Banner and Peirson (1998) used the technological advancement of particle image velocimetry (PIV) to estimate the water-side tangential stress of wind-forced microscale breaking waves. They found that the contribution of tangential stress to the total stress decreases as waves develop and grow steeper.

Most recent experimental studies have examined either the water or the air side. On the water side, for example, Melville et al. (2002) studied the velocity field under laboratory breaking waves using water-side PIV measurements and found that breaking generates at least one coherent vortex. Siddiqui and Loewen (2007) and Siddiqui and Loewen (2010) showed that turbulence is most intense under the crests of microscale breaking waves and coherent structures were observed. Savelyev et al. (2020) found the effect of increasing wave steepness on turbulent kinetic energy (TKE) to be negative at higher wind speeds and interpreted this as an effect of airflow separation.

Using air-side PIV measurements above wind-generated waves, Veron et al. (2007) observed a separation of the viscous sublayer from the surface past the wave crest, leading to a drop of viscous stress and near surface velocity. Grare et al. (2013b) conducted single point airflow velocity measurements using a hot wire anemometer above wind waves and found that substantial levels of viscous stress persist at moderate wind speeds. Airflow velocity measurements 100 µm above the air-water interface using combined PIV and laser-induced fluorescence (LIF) for mechanically and wind-generated waves by Buckley and Veron (2019) and Buckley et al. (2020) revealed that airflow separation past young wave crests increases the average intensity of the turbulence, while airflow separation is rare for low wind speeds and small slopes. Airflow separation events are accompanied by a dramatic drop in tangential viscous stress past wave crests. They concluded that viscous stress (resp. form drag) dominates at low (resp. high) wave slopes.

Simultaneous PIV measurements on both sides of the interface for breaking waves in the absence of wind were performed by Belden and Techet (2011) and showed the steadily increasing vorticity throughout the breaking process. André and Bardet (2015) conducted air-water PIV measurements in a canonical flow and showed that the shear at the interface is continuous.

In order to investigate the aforementioned longstanding questions on the coupling of the air-water viscous and turbulent boundary layers above and below the wavy interface, a novel air and water PIV/LIF measurement system was developed. The system was able to sequentially capture the dynamics of the air and water flow micrometers to centimeters above and below wind-generated surface waves using 2D/stereo PIV, as well as the evolution of the air-water interface using LIF. Importantly, the combination of a large-field-of-view, surface-detecting LIF system with a high-resolution PIV imaging of the air or water flow makes it possible to identify the influence of the position of individual waves within wind wave groups on the dynamical coupling between the air and the water.

4.3 Experimental Methods

4.3.1 Experimental set-up

The experiments presented here were developed and conducted at the Alfred C. Glassell, Jr. SUSTAIN (SUrge-STructure-Atmosphere INteraction) Laboratory at the Rosenstiel School of Marine and Atmospheric Science, University of Miami. The wind-wave tank is 18 m long, 6 m wide, and 2 m high. The PIV and LIF set-ups, shown in figure 4.1, were installed at a fetch of 10 m and measured wind and wave dynamics inside the tank at a distance of 0.8 m from the side wall. The tank was filled with fresh water with a constant mean depth of $D = 0.7$ m. Mechanical waves were generated by a piston-type wavemaker consisting of 12 paddles. Winds were generated by SUSTAIN's large axial fan. Waves were absorbed at the downwind end

by an energy-dissipating beach to eliminate reflections.

4.3.2 Air-side 2D PIV measurements

A planar PIV system was developed to measure along-tank 2D airflow velocity fields above surface waves. The airflow was seeded with fog droplets (diameter 12 μm) generated by pumping fresh water with a commercial-grade pressure washer (RYOBI 2700 PSI electric pressure washer) located above the tank, through 26 fog nozzles (AFT ECO 0.20 mm UNC) arranged in 4 rows (about 1 m wide, 0.6 m high). A pressure regulation system was developed and fitted to the pressure washer, allowing the pressure to remain at a constant value of 80 bar. The fog generating system was mounted close to the water surface at a fetch of 5 m. Two 6 MP CCD cameras (Dantec Dynamics FlowSense EO 6M-25, 2208x2756 pixels) were vertically stacked on top of one another. The cameras were slightly tilted downward (bottom $\sim 7°$, top $\sim 9°$). The bottom camera was fitted with a 105 mm lens (Sigma 105 mm F2.8), the top one with a 90 mm lens (Elicar Super Macro V-HQ 90 mm F2.5). The particles were illuminated by a green light sheet oriented in the along-wind direction, generated by a Nd:Yag laser flashing from above the tank (Litron Nano L 135 mJ - 15 Hz PIV, 532 nm wavelength) and equipped with sheet-generating optics. PIV image pairs were sampled at a frequency of 12 Hz, and accessed via Dantec DynamicStudio 6.7 before being processed in DynamicStudio and MATLAB. PIV images were processed with final interrogation windows of 8x8 pixels, resulting in a velocity field of 275x343 vectors per pair. The fog particles are expected to closely follow the airflow streamlines, with a Stokes number $St = \tau_p/\tau_k \ll 1$, a particle relaxation time of $\tau_p = 0.4$ ms, and an estimated Kolmogorov time scale τ_k that is 30 times larger in the bulk flow at the height of one wavelength.

4.3.3 Water-side 2D and stereo PIV measurements

Three 6 MP CCD cameras (Dantec Dynamics FlowSense EO 6M-25, 2756x2208 pixels) were mounted side-by-side on a Scheimpflug camera mount to measure along-tank 2D velocity fields below surface waves as well as the cross-tank velocity component. The two outer cameras were used for stereo PIV imaging, while the middle camera was used for planar PIV measurements. All three cameras were equipped with 50 mm lenses (Zeiss 50 mm f/1.4), bandpass green filters (Kentek ACRX-IR3B, with 0.73 optical density (OD) at 532 nm) to filter out all wavelengths except that of the PIV laser, and were slightly tilted upward ($\sim 5°$). The water was seeded with polyamide particles (Orgasol, diameter 10 μm) and illuminated by a second laser (Litron Nano L 145 mJ - 15 Hz PIV, 532 nm wavelength) flashing from below the tank. Water-side PIV image pairs were sampled at a frequency of 10 Hz and processed with final interrogation windows of 8x8 pixels, resulting in a velocity field of 317x266 vectors per pair for stereo PIV.

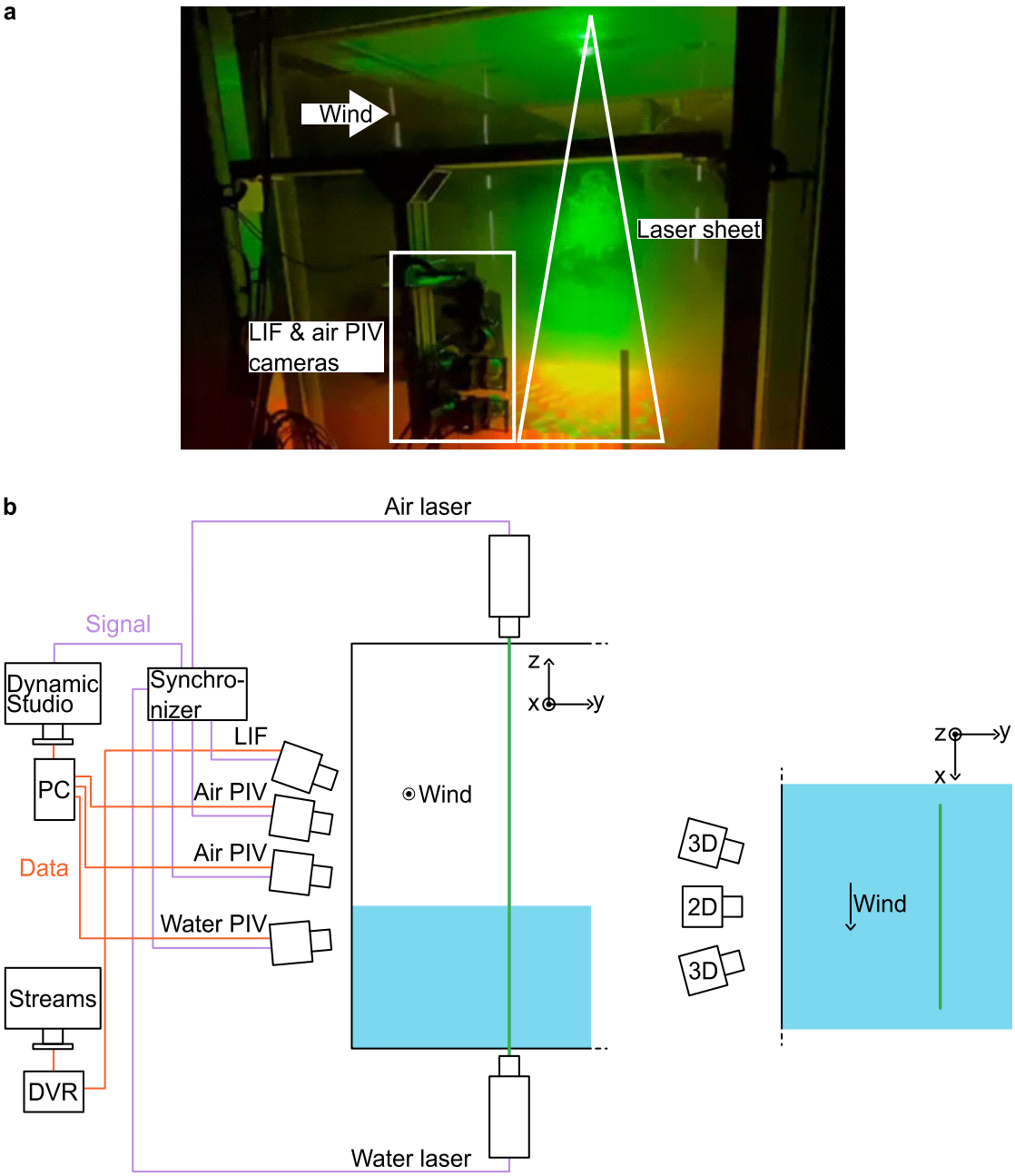

Figure 4.1: **a** Experimental set-up of air-side PIV at a fetch of 10 m, turbulent structures in the fog are visible. **b** Sketch of experimental set-up: side view (left), top view of water-side PIV (right).

4.3.4 LIF measurements

Wave field properties were captured by LIF simultaneously with the PIV. For this purpose, Rhodamine dye WT was added to the water. One 12 MP CMOS camera (IO Industries Victorem 120B68, 4112x3008 pixels) was mounted above the air-side PIV cameras and tilted downward ($\sim 19°$). The camera was fitted with a 24 mm lens (Canon macro 0.16m/0.52ft) and an amber acrylic bandpass optical filter (LASERVISION P1N01, with OD5+ at 532-535 nm) to make the green-light reflecting fog particles invisible to the camera. The images were transferred to hard drives via IO Industries digital video recorders (DVR Express Core 2) and accessed by Streams 7 software (IO Industries) before being processed in MATLAB.

4.3.5 Experimental procedure

Air-side and water-side experiments were performed successively for the same wind-wave conditions. Experiments were conducted with wind waves and wind over mechanically generated swell. The wind blower and wave maker were controlled by a separate PC (LabVIEW and HR Wallingford software). All cameras and lasers were synchronized and triggered by a Dantec Dynamics Synchronizer. The time between pulses for each PIV image pair was set individually for each run (8-32 runs per experimental condition), varying between 80 (air-side) and 20000 µs (water-side). For the air-side measurements, the PIV and LIF cameras sampled at a frequency of 12 Hz, resulting in 500 consecutive images, and for the water-side measurements, the cameras sampled at 10 Hz, resulting in 300 consecutive images. Raw PIV and LIF images are shown in figure 4.2.

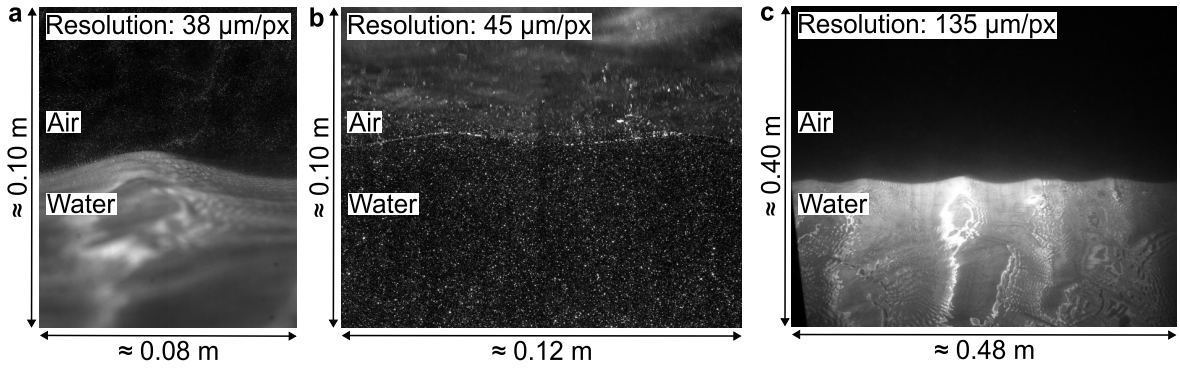

Figure 4.2: **a** Raw air-side PIV, **b** water-side PIV, and **c** air-side LIF images. Particles in air (**a**) and water (**b**) are visible.

4.3.6 Experimental conditions

In this work, we focus on a single set of experimental conditions with young, short, wind-generated gravity capillary waves and neutral conditions with air and water

temperatures of 23°C. Results are shown from a 15 s run for the air-side PIV, and a 30 s run for the water side (i.e., 180 image pairs for the air side and 300 for the water side). We use a larger time interval for the water side because a portion of the images were discarded due to occasional shadowing of the region under wave crests.

Thanks to the relatively large field of view of the LIF measurements and the short wind-wave wavelengths, the wavenumber spectra shown in figure 4.3 could be directly computed from a series of spatial snapshots of the water surface. We observe a good agreement between the wavenumber spectra of the two experiments. The observed differences may be attributed to the effect of the fog tracer particles in one case, and their absence in the other. At the peak wavenumber, the relative difference in the power spectral density (PSD) is approximately 15 %. We estimate that this difference is minimal and supports the assumption that the two experiments can be considered to have very similar wind-wave conditions. In addition, the frequency spectra are shown to compare the air-side and water-side measurements (panel b). These were obtained by extracting the time series of the water surface elevation from a fixed along-tank location ($x = const$) within the LIF snapshots. We note here that the sampling frequencies (10 and 12 Hz for the water-side and air-side runs, respectively) are slightly too small to obtain comparable spectral distributions. This explains the mismatch in the energy density at the peak. However, with a peak around 4.5 Hz, these sampling rates are likely sufficient for a reliable estimate of the peak frequency.

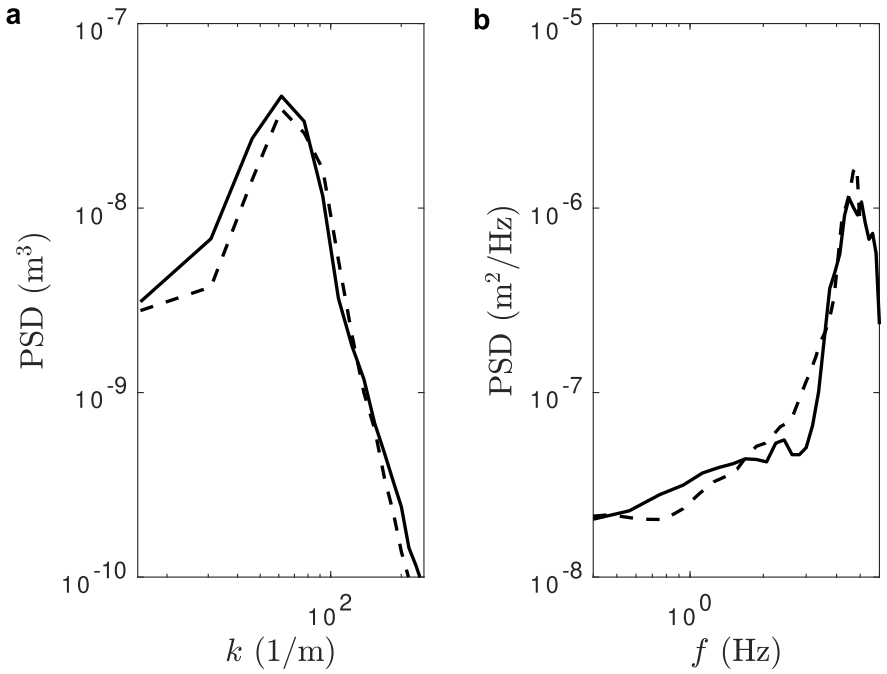

Figure 4.3: PSD estimates of water surface elevations computed from LIF. **a** Wavenumber spectra **b** Frequency spectra. Solid lines represent air-side measurements, while dashed lines represent the water-side.

The measured peak frequencies are Doppler shifted by the wind-induced drift u_d (Stewart and Joy, 1974; Smeltzer et al., 2019; Buckley et al., 2020)

$$\omega_m = \sigma + k u_d = k(c + u_d). \tag{4.1}$$

The approach to calculate the intrinsic wave speed c was as follows: 1. Use the dispersion relation $\sigma = \sqrt{(g + \gamma k^2/\rho)k \tanh(kD)}$, considering the air-water surface tension γ, with the peak wavenumber k_p from the wavenumber spectrum to calculate the intrinsic wave frequency σ, 2. Calculate the measured apparent wave frequency $\omega_m = 2\pi f_m$ with the peak frequency f_p from the frequency spectrum, 3. Calculate the wind drift $u_d = (\omega_m - \sigma)/k$, 4. Calculate the intrinsic wave speed either directly or with $c = c_m - u_d$ using cross-correlation on the LIF fields to obtain the measured apparent wave speed c_m. The wind drift was estimated to be $u_d = 0.06$ m/s, i.e., 0.8 % of U_{10}, and the intrinsic wave speed was directly estimated to be $c_p = 0.40$ m/s. By applying a cross-correlation to the LIF fields, we obtain $c_p = 0.38$ m/s. These results further demonstrate the versatility of LIF measurements. We note that the calculated wind drift velocity broadly matches the value of the water-side PIV horizontal velocity profile at the surface (not explicitly shown here).

Table 4.1 provides a list of the experimental conditions. The mean wind profile $U(z)$ follows the law of the wall with a viscous sublayer, buffer, and logarithmic layers (e.g., Kundu and Cohen, 2008). The friction velocity u_* was calculated by fitting the logarithmic part of the air-side PIV profile with

$$U(z) = \frac{u_*}{\kappa} \ln\left(\frac{z u_*}{\nu}\right) + const = \frac{u_*}{\kappa} \ln\left(\frac{z}{z_0}\right) \tag{4.2}$$

where κ is the *von Kármán constant*, ν is the kinematic viscosity, and z_0 is the roughness length. The mean air velocity at 10 m height U_{10} was obtained by extrapolating the profile. The airflow was found to be aerodynamically smooth to transitional according to Kitaigorodskii and Donelan (1984) with a roughness Reynolds number of $Re_r = u_* z_0/\nu = 0.11$.

Table 4.1: Experimental conditions. The mean air velocity at 10 m height U_{10}, the friction velocity u_*, and the roughness length z_0 were calculated by fitting the logarithmic part of the air-side PIV profile. The peak wavenumber k_p and apparent peak frequency f_p were obtained from the optical wave gauge spectra. The intrinsic wave speed c_p and the wind drift u_d were extracted using equation 4.1. The wavelength λ_p was derived by applying linear wave theory to k_p. The wave amplitude a was computed from the measured water surface elevation time series with $a = \sqrt{2} a_{rms}$. Note that the air-side and water-side parameters are similar.

U_{10} m/s	u_* m/s	z_0 mm	k_p 1/m	f_p Hz	c_p m/s	u_d m/s	λ_p m	a mm	ak_p -	c_p/U_{10} -	c_p/u_* -
7.20	0.21	0.01	61.62	4.50	0.40	0.05	0.10	1.90	0.12	0.06	1.92

4.4 Results and Discussion

4.4.1 Instantaneous 2D velocity and vorticity fields

The instantaneous horizontal u, vertical w velocity, and vorticity $\omega = -\partial w/\partial x + \partial u/\partial z$ fields resulting from PIV analysis of one image pair for the air (bottom camera) and water (middle camera) sides are shown in figure 4.4. Using the larger field of view of the LIF measurements, local wave properties such as wave steepness or crest speed could be obtained (see caption of figure 4.4), which are higher than the peak values in both cases (see table 4.1). In the air, the horizontal velocity drops dramatically to near zero values downwind of the wave crest. The vertical velocity is rather positive (upward) upwind of the crest, with a negative patch (downward velocity) downwind of the crest. The spanwise vorticity field shows a layer of high vorticity (defined as positive in the clockwise direction) that detaches from the surface past the crest of the wave. This detached vorticity layer indicates airflow separation (Buckley et al., 2020). These air-side observations are in general agreement with previous laboratory measurements from Buckley and Veron (2016) and Buckley and Veron (2017), and more recently from Do et al. (2024) and Abu Rowin et al. (2024). In the water, the wave-induced orbital motions dominate near the surface and decay with increasing water depth. Note that the velocity magnitudes are larger in the air than in the water, as expected for such strongly forced young wind waves.

4.4.2 Triple decomposition of instantaneous velocity fields

An instantaneous quantity q_{inst} (e.g., the horizontal and vertical velocities) near the wavy air-water interface can be decomposed into a phase-averaged quantity $\langle q \rangle$, which is the sum of a phase-independent mean $\bar{q}$ and a wave-coherent part $\tilde{q}$, and a turbulent perturbation q'_{inst} (e.g., Buckley and Veron, 2016)

$$\begin{aligned} q_{inst} &= \langle q \rangle + q'_{inst} \\ &= \bar{q} + \tilde{q} + q'_{inst}. \end{aligned} \tag{4.3}$$

The instantaneous PIV velocity fields were transformed and interpolated from a Cartesian coordinate system (x,z) to a flat surface coordinate system (x,ζ) by defining a vertical coordinate ζ that follows the wavy surface

$$\zeta = z - \eta(x, t) \tag{4.4}$$

where η is the surface elevation at time t and the horizontal coordinate x is kept.

Wave phase detection was performed on the PIV surface elevation using Hilbert transforms (Buckley and Veron, 2017). Since the surface detection must be very accurate for the calculation of viscous stresses, the surface for the air side was determined manually, while we used LIF to automatically detect the surface for the water side, where visual detection of the interface on the PIV images was more

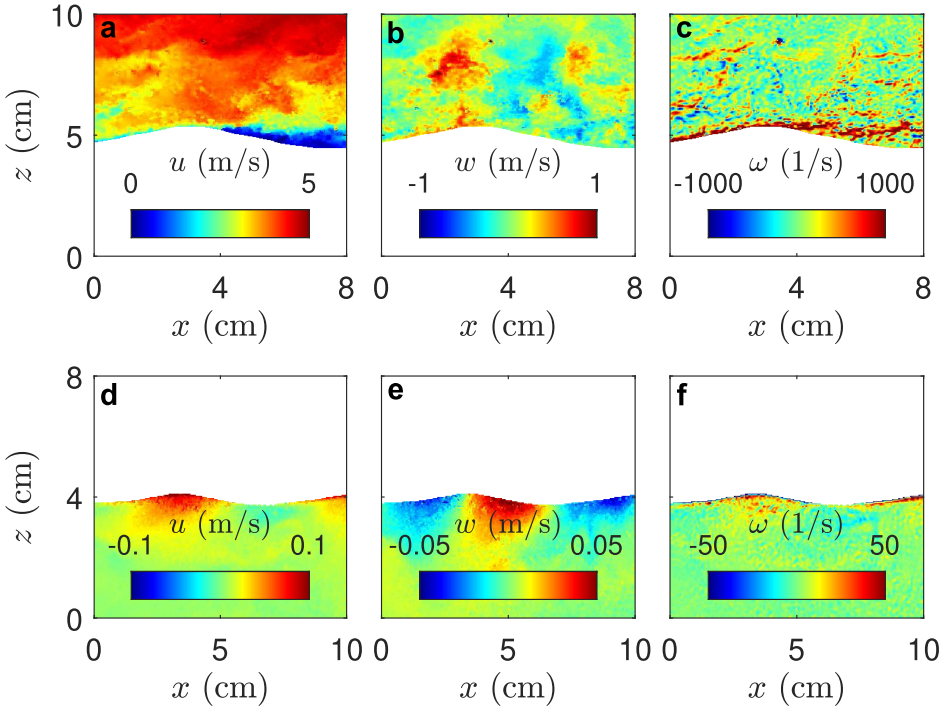

Figure 4.4: Examples of instantaneous horizontal u (**a**,**d**), vertical w (**b**,**e**) velocity, and vorticity ω (**c**,**f**) fields for the air (**a**-**c**) and water (**d**-**f**) sides. Local wave properties (with wave height H and zero-crossing wavelength L): air-side $(H/L)_a = 0.07$ and $c_a = 0.47$ m/s, water-side $(H/L)_w = 0.05$ and $c_w = 0.45$ m/s. The wind blows from left to right.

difficult. Surface detection on the LIF images was automated by developing and using an edge detection algorithm based on grayscale intensity gradients within the image.

Figure 4.5 shows an example of the decomposition of the horizontal velocity in the air. The phase-averaged velocity fields (panels a and b) show a clear (on average non-separated) sheltering pattern, or positive asymmetry, in accordance with previous work (Belcher and Hunt, 1998; Buckley and Veron, 2016). The instantaneous airflow is separated behind the wave crest, causing a large reduction in velocity that results in a negative turbulent velocity u' behind the wave crest. A positive velocity perturbation is observed along the upwind face of the wave. This result is in qualitative agreement with Buckley and Veron (2019).

4.4.3 Viscous stresses at the air-water interface

The total momentum flux τ_0 is partitioned at the air-water interface between tangential stress (skin friction drag) and normal stress (form drag). The stress is continuous across the air-sea boundary layer and momentum is conserved in both fluids ($\rho_a u_{*,a}^2 = \rho_w u_{*,w}^2$) (Pizzo et al., 2021).

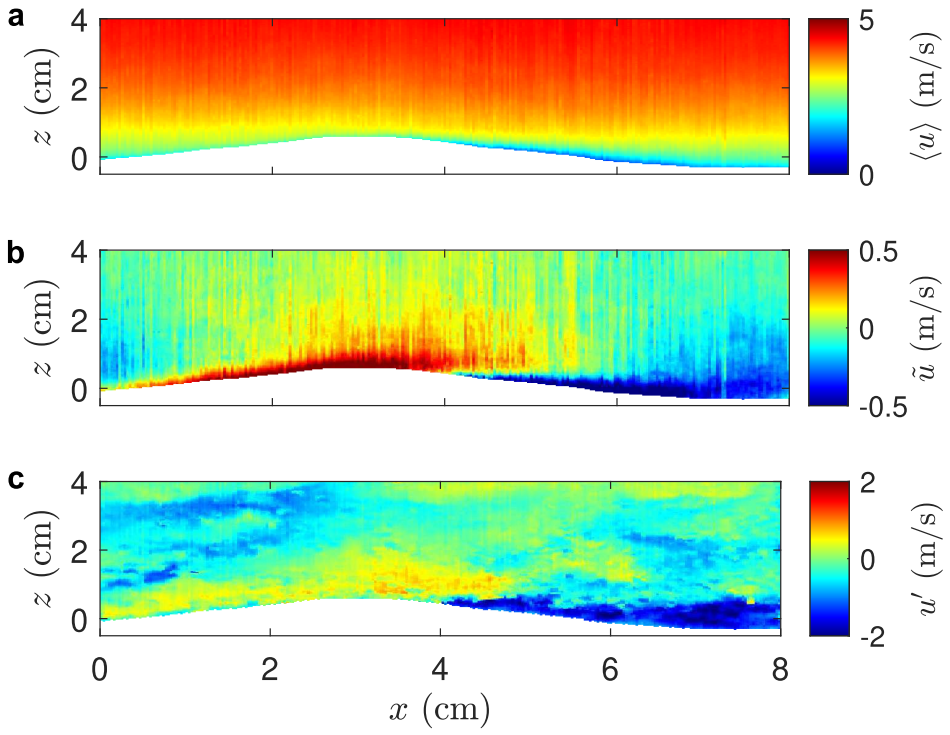

Figure 4.5: Example of a triple decomposed instantaneous horizontal velocity field. **a** Phase-averaged $\langle u \rangle$, **b** wave-coherent $\tilde{u}$, and **c** turbulent u' horizontal velocities. The wind blows from left to right.

We define the surface tangential viscous stress τ_v as

$$\tau_v = \mu \left(\frac{\partial u}{\partial \zeta} + \frac{\partial w}{\partial x} \right) \tag{4.5}$$

where μ is the dynamic viscosity of air or water. The thickness of the viscous sublayer in both fluids can be estimated using (Phillips, 1977; Kundu and Cohen, 2008)

$$z^+ = \frac{u_* z}{\nu} = 5 - 10 \tag{4.6}$$

where ν is the kinematic viscosity which gives a maximum viscous layer thickness of $z_{v,a} \approx 740$ µm for the air side and $z_{v,w} \approx 1227$ µm for the water side. Due to the limitations of the PIV interrogation area, the viscous stress is calculated in the following by averaging the first three points, i.e., 912 µm above and 1080 µm below the surface.

Figure 4.6 shows two waves of different steepness within one wave group. The steeper wave causes the airflow to separate behind the wave crest and shows a dramatic drop in viscous stress down to negative values, while the following less steep wave shows non-airflow separating behavior, with a drop in surface viscous stress that is less significant for both the air and water sides.

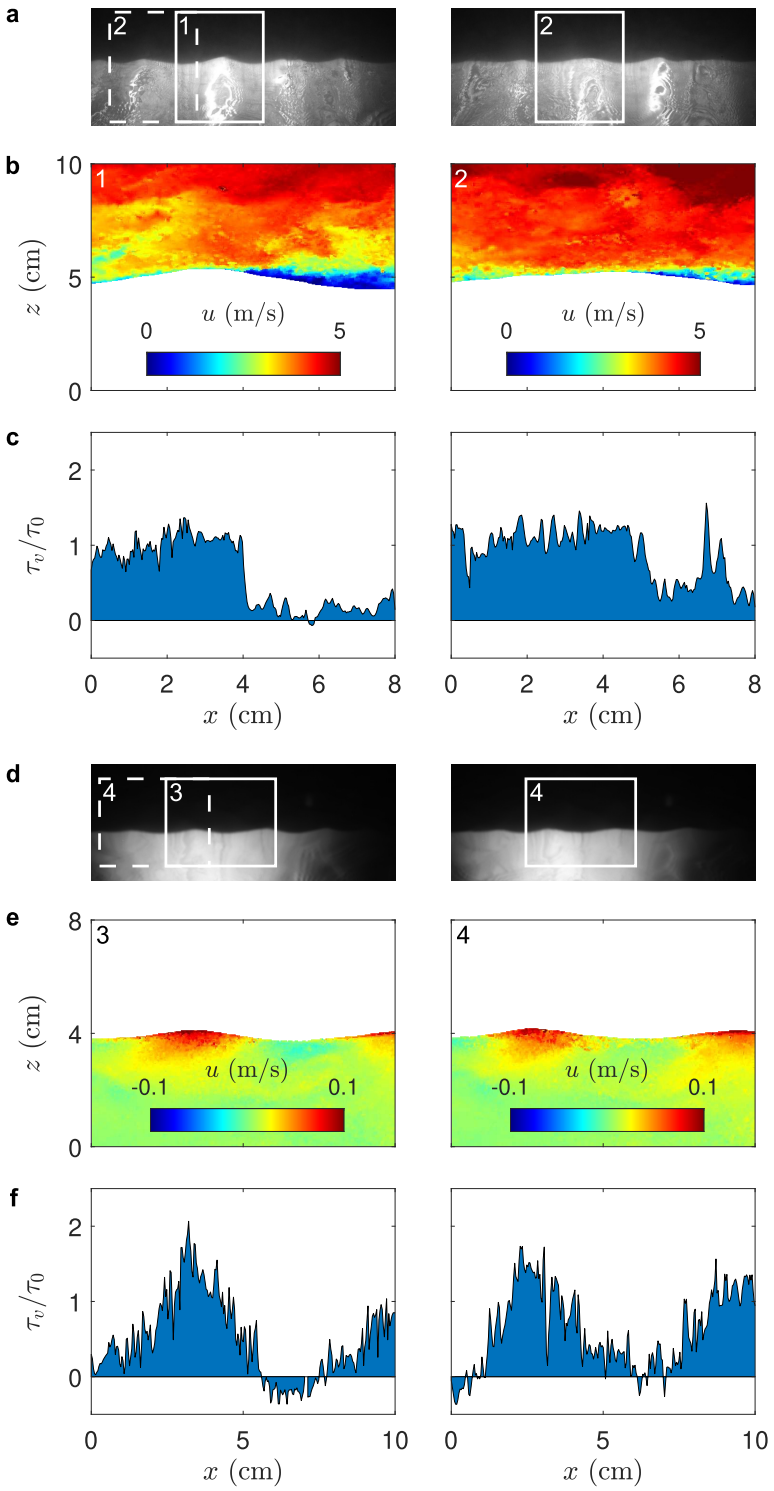

Figure 4.6: Viscous stresses within a wave group for successive steeper (1 & 3 with $ak_a = 0.2198$ & $ak_w = 0.1509$) and less steep (2 & 4 with $ak_a = 0.1453$ & $ak_w = 0.1459$) waves. Raw LIF images (**a**,**d**), horizontal velocities (**b**,**e**), viscous stresses (**c**,**f**). The wind blows from left to right.

Following the same procedure as for the velocity fields, the viscous stresses for the air and water sides were averaged with respect to wave phase using 48 phase bins (figure 4.7, panel a). The air-side viscous stress normalized by the total stress has a maximum at the wave crest and a minimum downwind of it, and remains positive for all wave phases. The viscous stress profile shows a strong vertical asymmetry, likely caused by the sheltering (on average non-separated) of the airflow past the wave crests. Similar to the air side, the water viscous stress has a maximum in the vicinity of the wave crest, but with a very slight downwind shift. The water-side along-wave stress profile is rather symmetrical when compared to the air-side one. In panel b of figure 4.7, we show the standard deviation of the viscous stress measurements for each phase bin. On the air side, we observe a significant increase (up to a factor of 2) in air-side viscous stress variability past the wave crest. We attribute this to the frequent separated and non-separated sheltering events past wave crests, whereby the viscous sublayer either thickens or detaches from the surface. On the water side, the standard deviation is highest at the crest which is in strong contrast with the air-side measurement. This is likely due to the frequent occurrence of microscale breaking events, which are accompanied by intense turbulence just below the crest (see for example Siddiqui and Loewen (2007)). We find a mean viscous stress of $\tau_{v,a} = 0.045$ Pa for the air side and $\tau_{v,w} = 0.028$ Pa for the water side, with both sides being equal only downwind of the wave crest. The magnitudes broadly agree with the Banner and Peirson (1998) finding of $\tau_{v,w} = 0.051$ Pa, albeit at a shorter fetch of 4.35 m, but for a similar wind speed of $U_{10} = 7.2$ m/s. We note that the observed discrepancies between the mean and along-wave air-side and water-side viscous stress estimates are significant. The mean values differ by 38 %, while the phase averages differ the most near wave troughs. An in depth investigation of the reasons for this mismatch is beyond the scope of this study and will be addressed in detail in future work. Nonetheless, two possible explanations can be mentioned here. First, we note that the crest to trough height of the phase-averaged water surface elevation is larger for the air-side PIV experiment than for the water-side one (figure 4.7, panel a). Since the viscous stress increases with increasing wave slope (e.g., Buckley et al., 2020), the slight difference in wave conditions could cause a mismatch in the mean viscous stress. Second, the along-wave variations in the normalized air-water viscous stress differential are likely caused by the important along-wave variations in the thickness of the viscous sublayer (here taken as constant, equal to 10 wall units, see equation 4.6 above). Further work will include an estimate of these variations and a wave-phase sensitive analysis of the thickness of the viscous sublayer.

4.4.4 Airflow separation and wave breaking

The Reynolds or turbulent stresses τ_t are important for the vertical transfer of horizontal momentum into the water column (Melville et al., 2002)

$$\tau_t = -\rho\overline{u'w'}. \tag{4.7}$$

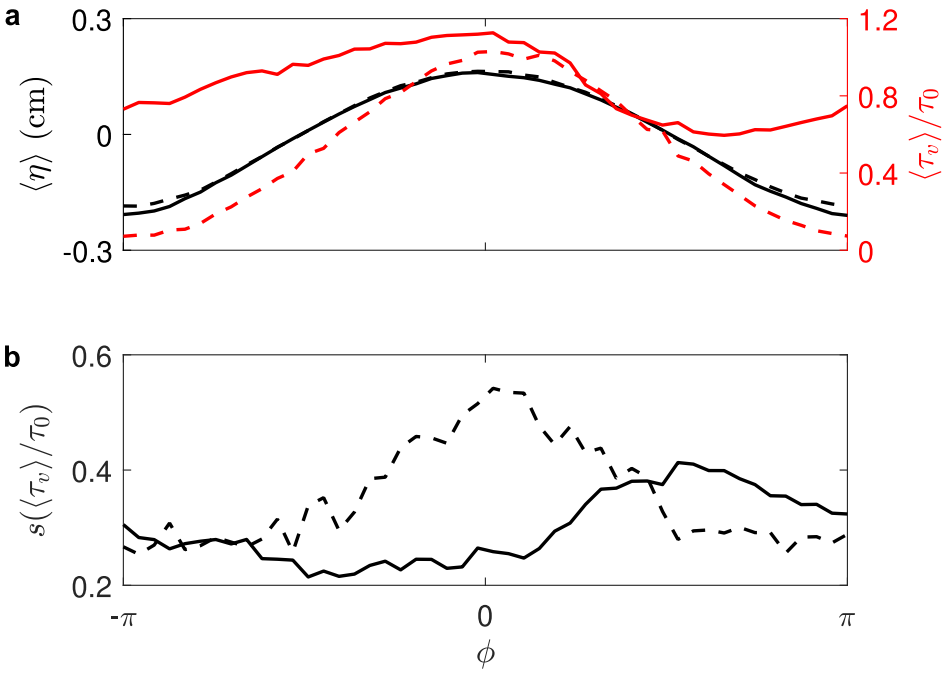

Figure 4.7: **a** Phase-averaged (48 bins) surface elevations and viscous stresses normalized by the total stress. **b** Standard deviations of viscous stresses normalized by the total stress. Solid lines represent air-side measurements, while dashed lines represent the water-side.

Figure 4.8 compares the turbulent stresses for the two successive waves of different slopes for the air and water sides. The air side shows a strong positive negative pattern in the airflow's separated region, while the non-airflow separated wave shows less turbulent stress. On the water side, we observe an increased negative turbulent stress below the wave crest for the steeper wave, indicating likely wave microscale breaking. It is to be noted that in the experimental conditions considered here, no air-entraining wave breaking events were observed. Microscale breaking waves, whose typical characteristics are parasitic capillaries downwind of wave crests (e.g., Banner and Phillips, 1974; Longuet-Higgins, 1992; Jessup et al., 1997), and increased turbulence under wave crests (Siddiqui et al., 2001), were observed frequently. The less steep wave shows lower turbulent stress values.

4.4.5 Phase-averaged wave-coherent air and water velocities

The phase-averaged wave-coherent 2D (planar) velocity fields for the air side (bottom camera) and planar and stereo velocities for the water side (middle camera/outer cameras) are shown in figure 4.9. In all fields we observe alternating positive and negative patterns. Acceleration occurs on the windward side and at the crest of the wave and deceleration occurs on the leeward side and at the troughs for both the air-side and water-side wave-coherent horizontal $\tilde{u}$ fields. While the pattern of $\tilde{u}$ for the air-side is tilted downwind, $\tilde{w}$ remains vertical with height. The underwater

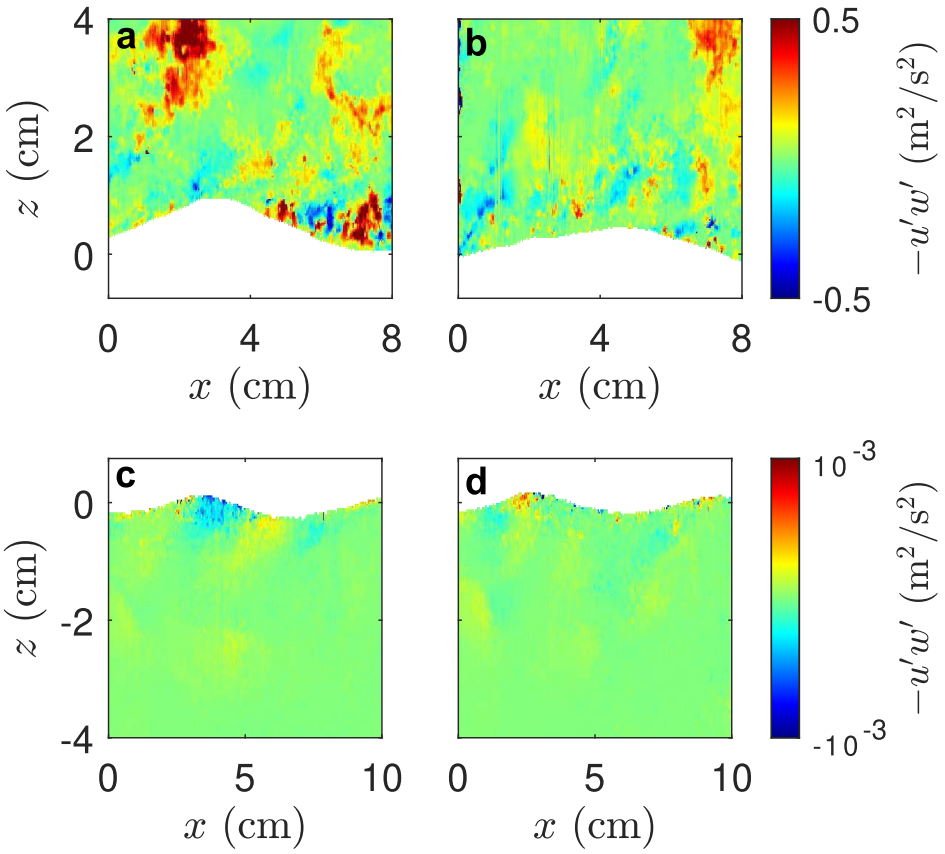

Figure 4.8: Turbulent stresses within a wave group for successive waves with different slopes. **a** Airflow separation ($ak_a = 0.2198$) **b** Non-airflow separation ($ak_a = 0.1453$) **c** Probably (microscale) wave breaking ($ak_w = 0.1509$) **d** Non-breaking ($ak_w = 0.1459$). The wind blows from left to right.

motions are weaker than the air-side motions. There is no obvious matching of the airflow with the underwater motions because the critical layer, where the wind speed equals the wave speed, is at the surface.

In addition, we compare the 2D results along the tank from the water-side middle camera (30 s interval) obtained using LIF surface detection with the water-side stereo PIV measurements (15 s interval) where the surface was manually detected. Although we find similar values and patterns, there is a discrepancy. The cross-tank component v shows a stronger signal than expected. Possible reasons for the non-zero values of $\tilde{v}$ are less than perfect verticality of the PIV laser sheet, or nonlinear wave-wave interactions causing roll circulations (Suzuki, 2019).

4.5 Conclusions

Thanks to a novel combination of air-side and water-side high-resolution PIV and large-field-of-view LIF, we were able to resolve near-surface velocities and viscous

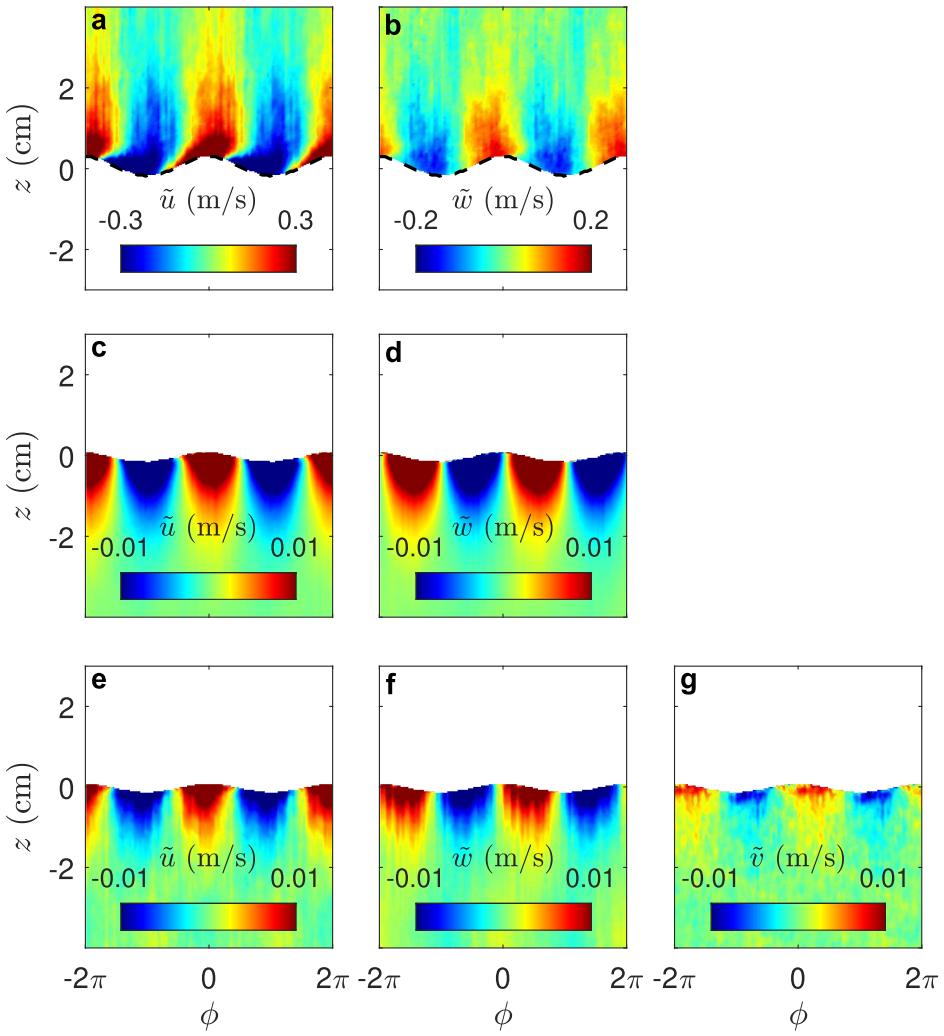

Figure 4.9: Phase-averaged (48 bins) wave-coherent horizontal (**a**,**c**,**e**), vertical (**b**,**d**,**f**), and cross-tank (**g**) velocity fields. Panels **a**,**b** are from the air-side bottom camera for a 15 s interval, panels **c**,**d** are from the water-side middle camera for a 30 s interval, and panels **e-g** are from the water-side outer cameras for a 15 s interval. Dashed line indicates critical layer.

stresses above and below laboratory young wind-generated gravity capillary waves within the exact same wind-wave conditions. We were able to directly observe strong along-wave modulations of both the air-side and water-side viscous stresses. On the air side, the modulation presents a clear horizontal asymmetry accompanied by an increase in the standard deviation past the wave crest caused by airflow separation events. This is in agreement with the measurements of Buckley et al. (2020). In contrast, the water-side phase-averaged viscous stress shows less asymmetry and the standard deviation peaks just at the crest. We conclude that this is a result of microscale wave breaking (Siddiqui and Loewen, 2007). In addition, the relatively large field of view of the LIF measurements allowed us to determine individual wave properties and to find waves with similar properties for air and water PIV

experiments. It was therefore possible to compare the instantaneous viscous and turbulent stresses for two consecutive waves of a wave group with different slopes, on the air and water sides of the interface. We observe airflow separation and increased turbulence below the steeper waves, which occurs in concert with a dramatic drop of the viscous stress below zero.

The techniques presented here have provided us with a unique and extensive high-resolution dataset for a range of different wind-wave conditions. This measurement system and dataset should prove useful to further investigate the influence of waves on the dynamical coupling of the air-water viscous and turbulent boundary layers. Specifically, using the large-field-of-view spatial snapshots (LIF), the role of individual wave properties such as steepness, asymmetry, skewness, will be used to parameterize the observed air and water dynamics.

4.6 Supplementary Material

4.6.1 Viscous sublayer

Figure 4.10 compares the viscous sublayer above the water surface for a wind speed of $U_{10} = 7.20$ m/s (analyzed in the previous sections) and below the water surface for the lowest measured wind speed of $U_{10} = 3.86$ m/s, which did not generate waves and results in the largest viscous sublayer thickness (see equation 4.6). Assuming that the velocity profile within the viscous sublayer is linear given a constant viscous stress (Kundu and Cohen, 2008), the left side of figure 4.10 shows the velocity profiles for both wind speeds (resp. sides of the water surface) and the linear fit of the points measured within the viscous sublayer. The right side compares the viscous stress estimates using the linear fit method ($\partial u/\partial\zeta$) with the measurements ($\partial u/\partial\zeta + \partial w/\partial x$). While the viscous stress tends to be constant for the smaller wind speed (except for the first three points), the air-side measurements of the higher wind speed do not show this behavior. Both profiles converge to zero with increasing height/depth. Note that $\partial w/\partial x$ is expected to be vanishingly small on average, but airflow separation events induce local, instantaneous near-surface streamwise and vertical variability in the flow field. In addition, w scales with the wave orbital velocity, and $\partial w/\partial x$ thus also scales with the wave slope (Buckley et al., 2020). We conclude that when waves are present, the profile cannot be fully viscous because of roughness elements that affect the wind profile.

Figure 4.11 shows the difference in phase-averaged viscous stress when using a flat Cartesian or curvilinear coordinate system (mentioned in section 2.1 and sketched in figure 2.1)

$$\begin{aligned} \tau_{v,cart} &= \mu\left(\frac{\partial u}{\partial \zeta} + \frac{\partial w}{\partial x}\right) \\ \tau_{v,curvi} &= \mu\left(\frac{\partial U}{\partial Z} + \frac{\partial W}{\partial X}\right), \end{aligned} \tag{4.8}$$

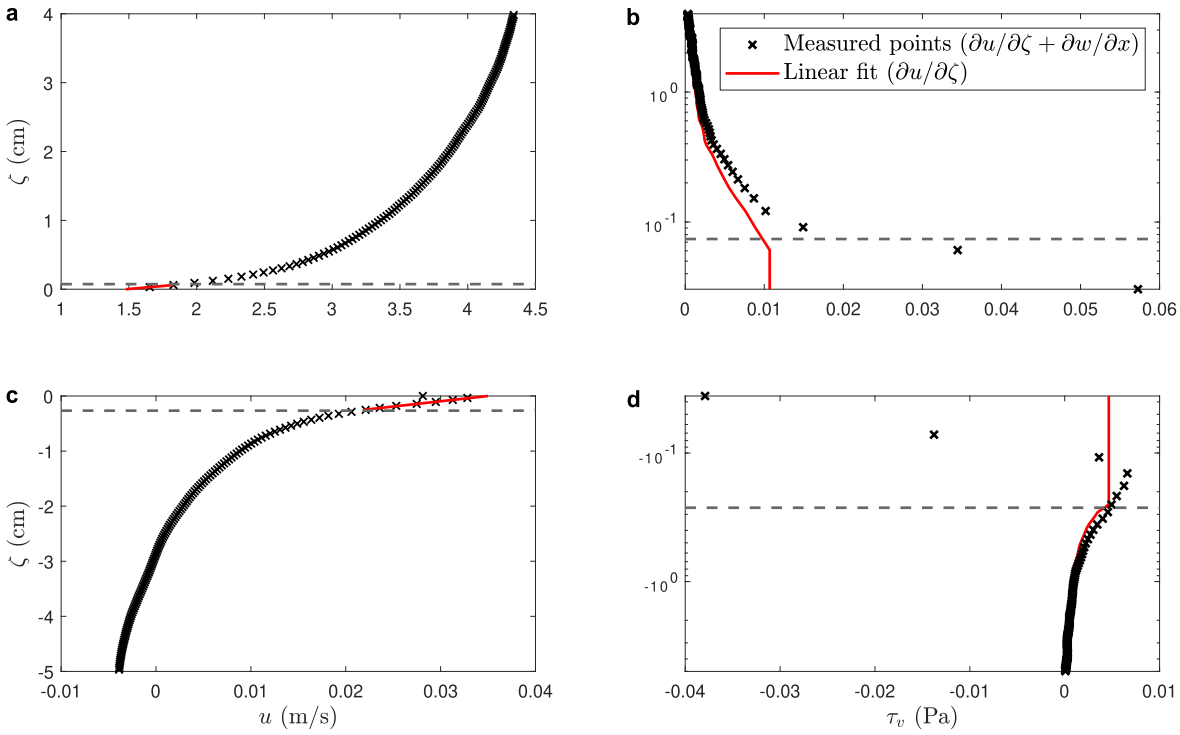

Figure 4.10: Horizontal wind speed and linear fit within the viscous sublayer (**a**,**c**). Comparison of viscous stress estimates from the linear fit with gradients computed from the measured velocity fields (**b**,**d**). Top and bottom panels show air (wind speed U_{10} = 7.20 m/s) and water side (wind speed U_{10} = 3.86 m/s), respectively. Dashed lines indicate viscous sublayer height.

where the measured variables u and w are the horizontal and vertical components of the velocity in the flat Cartesian coordinate system ((x, ζ), see equation 4.4). U and W are the curvilinear (X, Z) components, which are tangential and normal to the surface, respectively. Since the wave amplitude and slope are small at a wind speed of U_{10} = 7.20 m/s, both coordinate systems provide similar estimates along the wave.

4.6.2 Phase-averaged viscous stress lower wind speed

The phase-averaged air-side viscous stresses for wind speeds of U_{10} = 3.86 m/s and U_{10} = 7.20 m/s are shown in figure 4.12. The viscous stress is smaller for the lower wind speed, which did not generate waves, and therefore no along wave modulation is visible, and the viscous stress is relatively constant. The magnitude and shape for both wind speeds are qualitatively consistent with Buckley (2015).

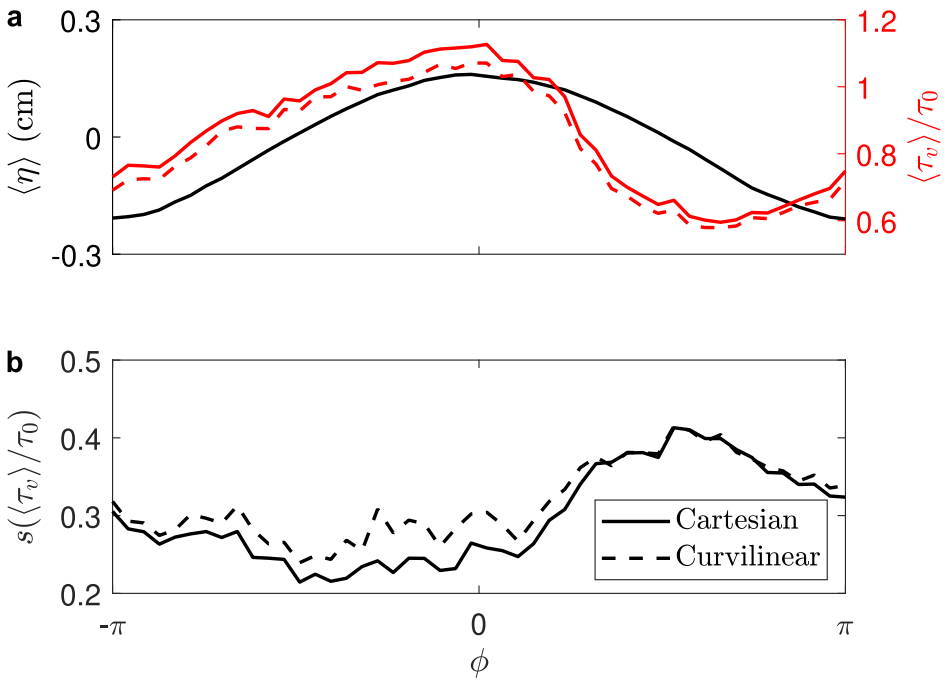

Figure 4.11: **a** Phase-averaged (48 bins) surface elevations and viscous stresses normalized by the total stress. **b** Standard deviations of viscous stresses normalized by the total stress. Solid lines represent the estimates using the Cartesian coordinate system, while dashed lines represent the curvilinear system.

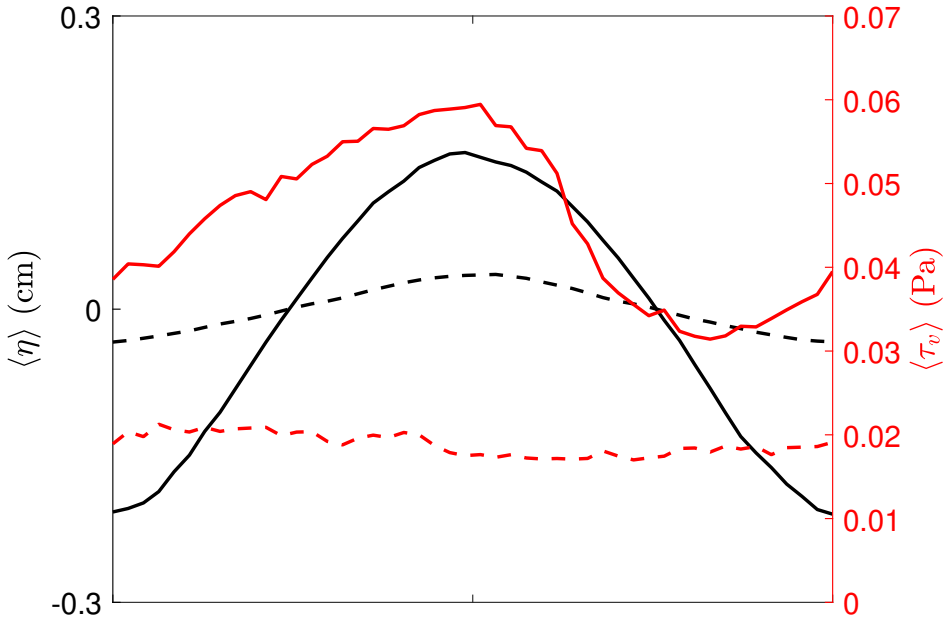

Figure 4.12: Phase-averaged (48 bins) surface elevations and viscous stresses. Solid lines represent U_{10} = 7.20 m/s, while dashed lines represent U_{10} = 3.86 m/s.

5

Influence of Individual Wave Slope on Mean Viscous and Turbulent Stress

This chapter is a reprint of the manuscript *"Influence of individual wave slope on mean viscous and turbulent stress"*, which is in preparation for submission.

Citation: Tenhaus, J., Buckley, M. P. Influence of individual wave slope on mean viscous and turbulent stress. In preparation for submission (2025).

Key Points

- Laboratory wind waves are divided into two groups of different slopes for the same experimental condition
- Similar turbulent horizontal velocities, except for regions downwind of airflow separating crests, are observed
- While viscous stress has a dominant contribution to surface currents in flat wave conditions, it contributes mostly to wave growth as waves steepen

5.1 Abstract

Individual wave characteristics are rarely considered when studying wave growth, (microscale) breaking, and surface currents. However, they play an important role in the physical processes that take place directly at the air-water interface. We performed high-resolution planar velocity measurements within the first micrometers to centimeters above surface gravity waves at the University of Miami's SUSTAIN air-sea interaction facility. A combined particle image velocimetry (PIV) and laser-induced fluorescence (LIF) system was adapted and installed in the large (18 m long, 6 m wide) wind-wave tunnel at a fetch of about 10 m. This work focuses on the influence of individual wave properties, such as wave slope and asymmetries, on viscous and turbulent stresses. By dividing the waves into two ensembles of different slopes (flat and steep waves), we find that both exhibit similar turbulent horizontal velocities, except for regions downwind of airflow separating crests. There, magnitude of turbulent quantities is strongly dependent upon the ensemble chosen to define them. The phase-averaged viscous stresses are the same for the flat and steep waves just upwind of the crests, and differ most downwind of the crests, due to the effects of individual sheltering events on the mean. With increasing wave slope, the contribution of viscous forces to wave growth increases, while the contribution to currents decreases, whereas the wind input term from viscosity becomes less significant.

5.2 Introduction

Wind energy input into the upper ocean is largely controlled by wave-related processes, including wave growth and subsequent breaking (Wunsch and Ferrari, 2004). However, our understanding of the small-scale dynamics at the air-sea interface remains incomplete, in spite of extensive efforts within the past decades (Sullivan and McWilliams, 2010; Ayet and Chapron, 2022).

One hundred years ago, Jeffreys (1925) introduced the separated sheltering mechanism, according to which waves grow due to a pressure asymmetry caused by airflow separation on the leeward side of the wave. Miles (1957) generalized the

problem for a later stage of wave growth using linear stability analysis and showed that at the critical height, where the wind speed is equal to the wave speed, an instability occurs caused by the coupling of the airflow shear with the water wave. This process can remove energy and momentum from the wind and impart them to the waves. Belcher and Hunt (1993) argued that for short waves, where the critical height is very close to the surface, Miles (1957) inviscid theory is inappropriate, and extended Jeffreys (1925) sheltering mechanism, calling it non-separated sheltering. A detailed summary of existing wave growth theories is given by Ayet and Chapron (2022).

Wind waves are often classified by their wave age, c/u_* or c/U_{10}, where c is the wave speed, u_* is the friction velocity, and U_{10} is the wind speed at 10 m height, as it is a direct indicator of the coupling between wind and waves. Sheltering mechanisms are assumed to dominate the momentum transfer from the wind for young (small wave age, $c/u_* \lesssim 15$) and old waves ($25 \lesssim c/u_*$), whereas the critical layer theory may be important for wave growth for intermediate wave ages, where $15 \lesssim c/u_* \lesssim 25$ (Belcher and Hunt, 1998; Grare et al., 2013a). In addition to the wave age, the individual wave slope is an important factor in controlling the sheltering past strongly forced wind waves and can lead to airflow separation. Banner and Melville (1976) conducted flow visualization studies and established, on theoretical grounds derived from the earlier work of Banner and Phillips (1974) studying incipient breaking wave conditions, that airflow separation over a surface gravity wave occurs concurrently with breaking (see also the work of Gent and Taylor (1977)). Bonmarin (1989) and Bonmarin et al. (1989) investigated steep waves using visualization techniques and parameters such as crest front steepness and horizontal (resp. vertical) asymmetry factors introduced in Kjeldsen and Myrhaug (1980). It was shown that there is a relationship between the rate of growth of wave asymmetry and the type of breaker, e.g., spilling or plunging breakers. Parameters describing the breaking wave geometry were also calculated in Reul et al. (1999) and Reul et al. (2008), who conducted the first two-dimensional airflow measurements over mechanically generated waves using particle image velocimetry (PIV). They showed that waves with similar crest heights and wavelengths can have different crest front steepness and horizontal wave asymmetry factors, leading to airflow separation events past wave crests or not, and concluded that the separation process can only be sustained in the early stages of breaking if the wave crest geometry is highly asymmetric with high local slopes downwind of the crest.

Using the triple decomposition, (see for example Phillips (1977)), that separates the instantaneous velocity near a wavy interface into a mean, wave-coherent and turbulent part, Hsu et al. (1981) identified wave-induced modulations of the airflow turbulence (over monochromatic laboratory waves) as a key component of the wind-wave coupling. Mastenbroek et al. (1996) found evidence that rapid distortion of the turbulence occurs above the critical height, which has important implications for turbulence closure models. Buckley and Veron (2016) observed intense phase-locked turbulence downwind of wave crests, where airflow sheltering takes place.

To understand the turbulent structure below wind-generated surface waves, Thais and Magnaudet (1996) performed Laser Doppler Velocimetry (LDV) measurements in a wind-water tunnel. They used a nonlinear triple decomposition method to decompose the velocity into three contributions: potential and rotational wave-related components and the remaining turbulent contribution. In spite of these important advances, identifying turbulent quantities in the vicinity of broadbanded ocean surface waves remains subject of debate, due to the lack of clear scale separation between turbulence and small-scale wave-coherent motions, especially in the case of a broadbanded wave spectrum.

Buckley et al. (2020) investigated the behavior of viscous stress for (non) airflow separating waves using PIV and laser-induced fluorescence (LIF). By partitioning the air-water momentum flux between viscous stress and form drag at the interface, they found that viscous stress (resp. form drag) dominates at low (resp. high) wave slopes, and that tangential viscous forcing makes a small contribution to wave growth. Yousefi et al. (2020) and Yousefi et al. (2021) used the same dataset for more detailed investigations of the turbulent and wave kinetic energy budgets. They observed that the mean profile of the wave-induced stress decreases to a negative minimum far from the surface, where the turbulent stress is nearly equal to the total stress. Near the interface, the wave-induced stress increases to a positive value where the turbulent stress is reduced, very close to the surface both stresses vanish, and the stress is supported by viscosity. In addition, the interactions between the wave and turbulent perturbations showed an energy transfer from the wave to the turbulence in the bulk of the wave boundary layer and from the turbulence to the wave in a thin layer near the interface.

To identify the influence of individual wave properties on the dynamical coupling of the air–water viscous and turbulent boundary layers, we use a combination of a large-field-of-view, surface-detecting LIF system with a high-resolution PIV imaging of the airflow above surface gravity waves. We divide the waves into two groups with different slopes and study the influence on phase-averaged properties such as turbulent and viscous stress. In addition, we discuss the difficulty of quantifying the influence of wave-coherent effects on the air–sea momentum and energy fluxes and distinguishing them from turbulent contributions.

5.3 Experimental Methods

The experiments presented here were developed and conducted at the Alfred C. Glassell, Jr. SUSTAIN (SUrge-STructure-Atmosphere INteraction) Laboratory at the Rosenstiel School of Marine and Atmospheric Science, University of Miami. The wind-wave tank is 18 m long, 6 m wide, and 2 m high. The PIV and LIF set-ups, shown in figure 5.1, were installed at a fetch of 10 m and measured wind and wave dynamics inside the tank at a distance of 0.8 m from the side wall. The tank was filled with fresh water with a constant mean depth of 0.7 m. Neutral conditions

were established with air and water temperatures of 23°C. Winds were generated by SUSTAIN's large axial fan, controlled by a program written in LabVIEW. Waves were absorbed at the downwind end by an energy-dissipating beach to eliminate reflections. In this paper, we focus on one particular wind-wave condition of wave age $c_p/u_* = 1.92$ and $c_p/U_{10} = 0.06$ with $U_{10} = 7.2$ m/s, wave slope $ak_p = 0.12$, peak frequency $f_p = 4.5$ Hz, peak wavenumber $k_p = 61.62$ 1/m, and wavelength $\lambda_p = 0.1$ m, which is described in detail in Tenhaus et al. (2024).

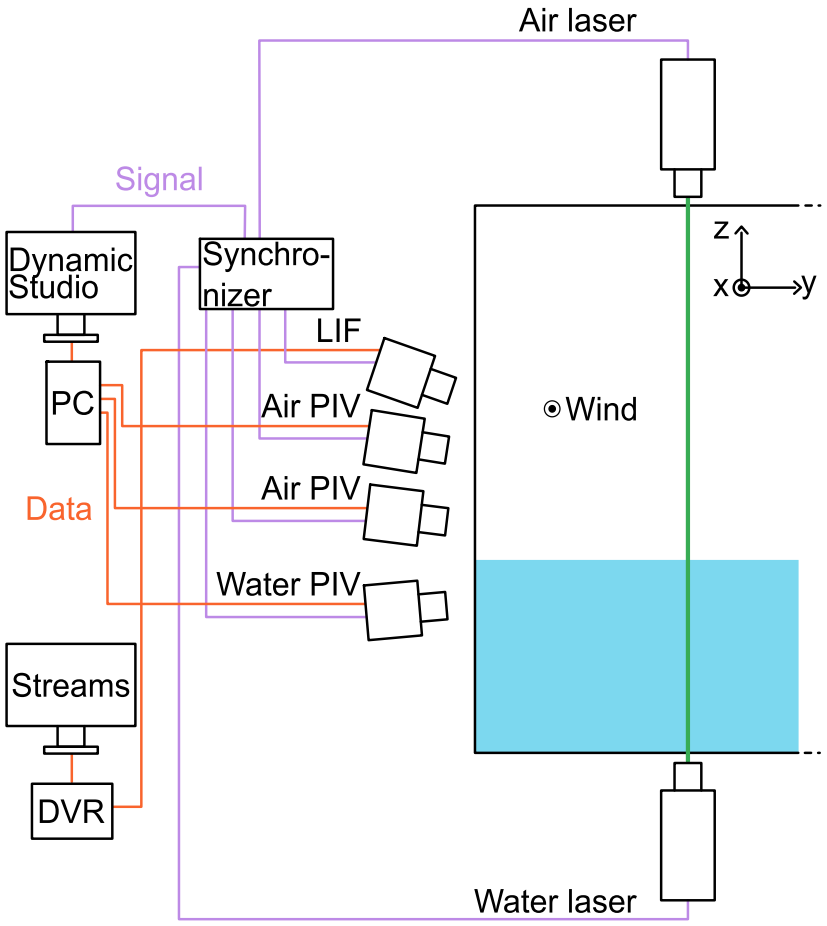

Figure 5.1: Sketch of experimental set-up (side view).

5.3.1 Airflow velocity measurements

A planar PIV system was developed to measure along-tank 2D airflow velocity fields above surface waves. The airflow was seeded with fog droplets (diameter 12 µm) generated by pumping fresh water with a commercial-grade pressure washer (RYOBI 2700 PSI electric pressure washer) located above the tank, through 26 fog nozzles (AFT ECO 0.20 mm UNC) arranged in 4 rows (about 1 m wide, 0.6 m high). A pressure regulation system was developed and fitted to the pressure washer, allowing

the pressure to remain at a constant value of 80 bar. The fog generating system was mounted close to the water surface at a fetch of 5 m. Two 6 MP CCD cameras (Dantec Dynamics FlowSense EO 6M-25, 2208x2756 pixels) were vertically stacked on top of one another. The cameras were slightly tilted downward (bottom ~ 7°, top ~ 9°). The bottom camera was fitted with a 105 mm lens (Sigma 105 mm F2.8), the top one with a 90 mm lens (Elicar Super Macro V-HQ 90 mm F2.5). The particles were illuminated by a green light sheet oriented in the along-wind direction, generated by a Nd:Yag laser flashing from above the tank (Litron Nano L 135 mJ - 15 Hz PIV, 532 nm wavelength) and equipped with sheet-generating optics. All cameras and lasers were synchronized and triggered by a Dantec Dynamics Synchronizer. The time between pulses for each PIV image pair was set individually for each run (8-32 runs per experimental condition) and was set to 100 µs for the run processed in this study. PIV image pairs were sampled at a frequency of 12 Hz, and accessed via Dantec DynamicStudio 6.7 before being processed in DynamicStudio and MATLAB. PIV images were processed with final interrogation windows of 8x8 pixels, resulting in a velocity field of 275x343 vectors per pair. The fog particles are expected to closely follow the airflow streamlines, with a Stokes number $St = \tau_p/\tau_k \ll 1$, a particle relaxation time of $\tau_p = 0.4$ ms, and an estimated Kolmogorov time scale τ_k that is 30 times larger in the bulk flow at the height of one wavelength.

5.3.2 Wave measurements

Wave field properties were captured by LIF simultaneously with the PIV. For this purpose, Rhodamine dye WT was added to the water. One 12 MP CMOS camera (IO Industries Victorem 120B68, 4112x3008 pixels) was mounted above the air-side PIV cameras and tilted downward (~ 19°). The camera was fitted with a 24 mm lens (Canon macro 0.16m/0.52ft) and an amber acrylic bandpass optical filter (LASERVISION P1N01, with OD5+ at 532-535 nm) to make the green-light reflecting fog particles invisible to the camera. The LIF camera sampled, as the PIV cameras, at a frequency of 12 Hz, resulting in 500 consecutive images. The images were transferred to hard drives via IO Industries digital video recorders (DVR Express Core 2) and accessed by Streams 7 software (IO Industries) before being processed in MATLAB.

5.4 Results and Discussion

5.4.1 Wave characteristics

The large-field-of-view LIF measurements allow us to automatically detect individual waves, as shown in figure 5.2. Here, four full waves (beginning and ending with a zero-upcrossing) were identified in the instantaneous LIF snapshot by developing and using an edge detection algorithm based on grayscale intensity gradients within the image. This method, called zero-downcross analysis, uses the trough and subsequent

crest (waves move from left to right here) in the definition of a single wave, and defines the wave height H as the difference between these water levels. As described by Kjeldsen and Myrhaug (1980), the zero-downcross analysis is believed to be the only analysis that represents the physical conditions relevant to breaking waves, while the zero-upcross analysis provides a wave height behind and not ahead of a potentially breaking wave.

Since the PIV field of view, indicated by the gray area, is much smaller than the large (LIF) field of view, only the first wave closest to the PIV field is used in the following. Individual wave properties such as wave slope $ak = \pi H/L$ (noted WS hereafter), crest front steepness $\epsilon = \eta'/L'$ (CFST), horizontal wave asymmetry $\mu = \eta'/H$ (HWA), and vertical crest asymmetry $\lambda = L''/L'$ (VCA) can be calculated, where n' is the crest elevation measured from the mean water level and L' and L'' are the horizontal distances defining the position of the wave crest relative to the zero-crossing points (Kjeldsen and Myrhaug, 1980). The relative probability of the characteristics over 1203 waves is shown in figure 5.2.

The relative probability of WS is evenly distributed, suggesting that steeper waves break more frequently. We find most waves (17.8 %) in the interval 0.18-0.21 during three runs (42 s each) of imaging. The normal distribution function has a maximum at a wave slope of $ak = 0.155$, which we will use as a cutoff to partition the waves into two different groups: flat and steep waves. In addition, the relative probability of CFST shows slightly larger values than WS, and we also observe a high vertical crest asymmetry, where a value greater than 1 means that the waves are tilted forward.

The instantaneous LIF snapshot already shows that the waves are not evenly distributed about the still water level, but rather show peaked crests and flat troughs, with the crests farther above the mean water level than the troughs are below this level, typical for so-called Stokes waves (Young, 1999). This observation is emphasized by the horizontal wave asymmetry factor, which is 0.5 for symmetric waves. On average, the measurements show waves with HWA larger than 0.5, indicating peaked crests. While Bonmarin (1989) observed an increase in horizontal asymmetry of up to 0.90 for plunging breaking waves, only 2 % of the waves studied here reach this limit, supporting the assumption that mainly microscale breaking takes place.

5.4.2 Phase-averaged horizontal velocity, turbulent and viscous stress

Using the wave slope $ak = 0.155$ as a cutoff, we can compute the phase-averaged horizontal velocity, turbulent and viscous stress (see Tenhaus et al. (2024)) for all, flat, and steep waves. This allows us to split a wind-wave condition into two with different wave slopes, but without changing the (mean) wind speed.

Figure 5.3 shows the phase-averaged horizontal velocity $\langle u \rangle$ in the air above the waves in a frame of reference moving at the peak intrinsic wave speed c_p normalized by the wind speed at 10 m height U_{10} (calculated in Tenhaus et al. (2024)) for the three groups. Overall, the velocity is highest above the crest, slower downwind of it, and accelerates upwind of the crest, indicating thinning and thickening of the

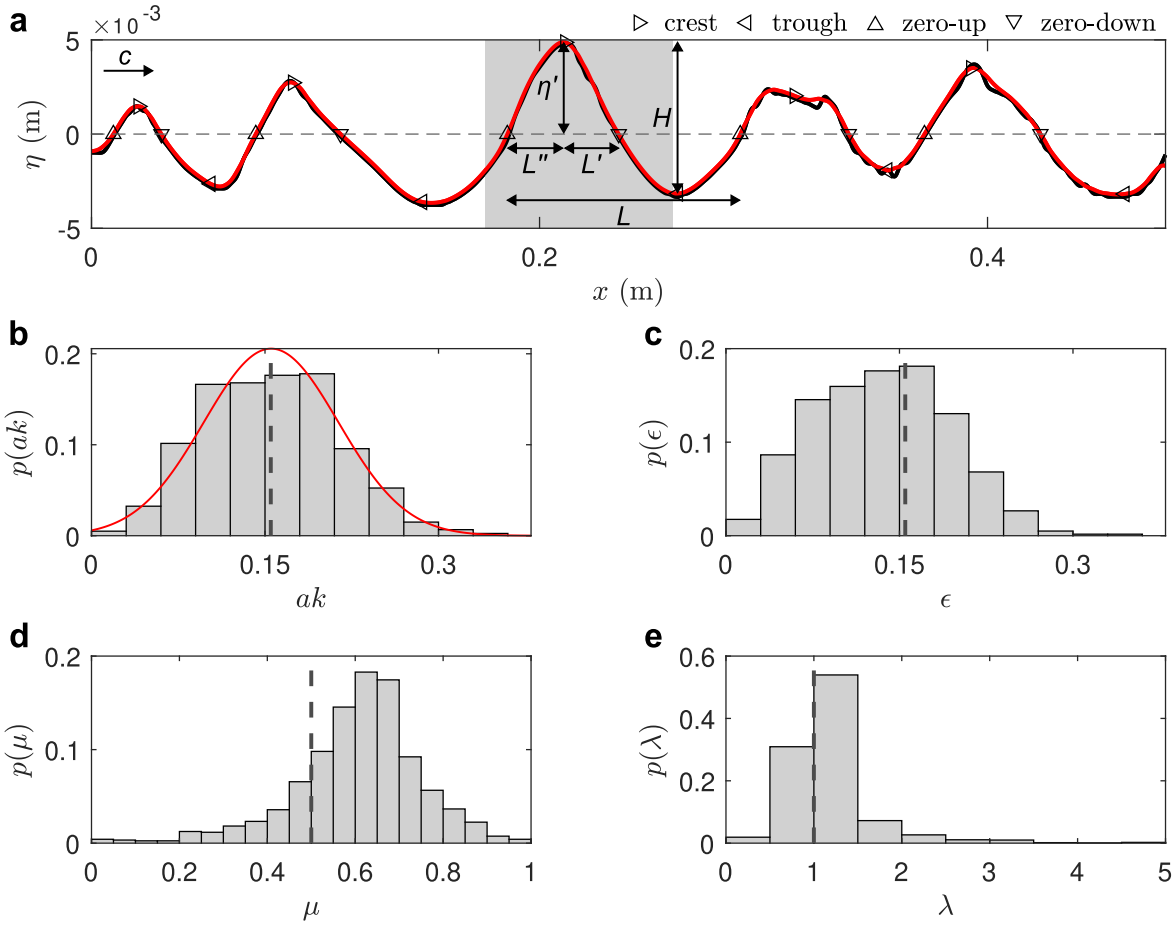

Figure 5.2: **a** Detected surface elevation using LIF in black and smoothed surface in red. Relative probability of **b** wave slope with cutoff 0.155 and normal distribution function in red, **c** crest front steepness, **d** horizontal wave asymmetry with 0.5 indicating symmetry, **e** vertical crest asymmetry with 1 indicating symmetry.

boundary layer. The airflow is most sheltered behind the steep waves, characterized by a sharp decrease in the airflow velocity just downwind of the crest near the surface, and a jet of low-velocity fluid ejected up to a higher height than for the other cases. Nevertheless, $\langle u \rangle - c_p$ is positive overall and (on average) does not separate from the surface.

The dotted line shows the (thin) inner layer z_i (Belcher and Hunt, 1993), computed using the time scales of the eddy evolution ($\kappa z_i / u_*$) and the mean flow advection ($1/(k_p|\langle u \rangle(z_i) - c_p|)$) at each phase bin

$$k_p z_i |\langle u \rangle(z_i) - c_p| = 2\kappa u_* \tag{5.1}$$

where κ is the *von Kármán constant* and k_p is the peak wavenumber obtained from power spectral density (PSD) estimates of water surface elevations computed from LIF, while the dashed line indicates the mean inner layer. In the inner region, turbulent eddies are assumed to be in local equilibrium with the mean flow, dissipating energy

faster than they are advected. Above, in the outer region, the advection of the turbulent eddies by the mean wave-coherent airflow must be considered to close the TKE budget (Belcher and Hunt, 1993; Belcher and Hunt, 1998; Grare et al., 2013a; Buckley and Veron, 2016; Ayet and Chapron, 2022; Carpenter et al., 2022). We observe that the inner layer thickens downwind of the wave crest, especially for the steeper waves, due to the effect of shear stress in the inner region, leading to pressure asymmetry in the outer region (not shown here). The steeper the waves, the more the inner layer deviates from its mean value, while it is significantly smaller above the crest and larger downwind of it. According to Belcher and Hunt (1998), for slow and fast waves, the critical layer, where the wind speed equals the wave speed ($\langle u(z_c)\rangle = c_p$), does not play a dynamical role and the momentum transfer between wind and waves is controlled by the non-separated sheltering mechanism in the inner region. Note that we do not observe a critical layer because it is too close to the surface.

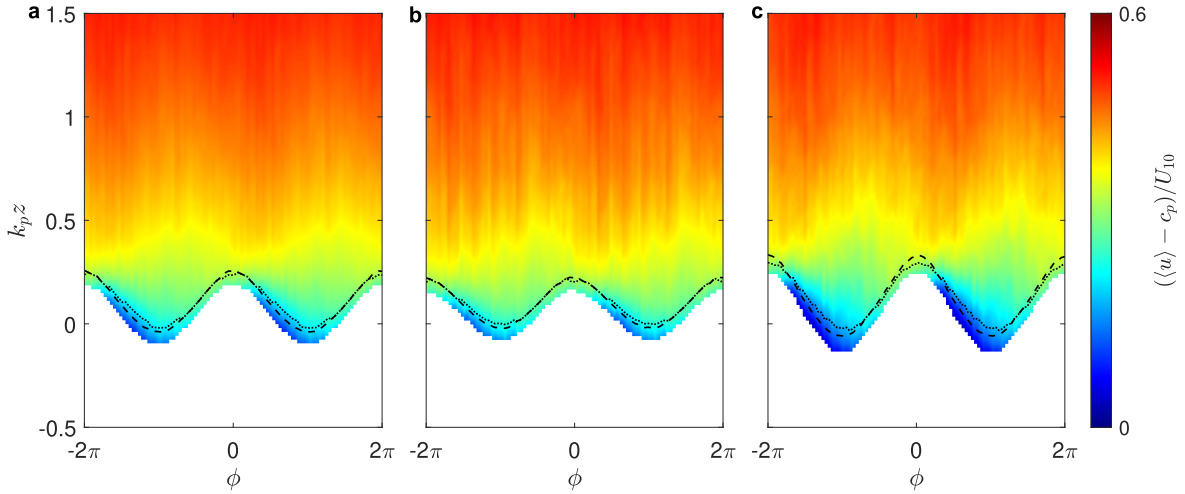

Figure 5.3: Phase-averaged (48 bins) horizontal velocity for **a** all waves, **b** flat waves with $ak < 0.155$, and **c** steep waves with $ak \geq 0.155$. Dotted line indicates the inner layer, dashed line indicates its mean.

The phase-averaged turbulent stress $-\langle u'w'\rangle$ (also known as Reynolds stress R_{13}), a stress exerted by the turbulent fluctuations on the mean flow, is shown in figure 5.4. In concert with the decrease in horizontal velocity downwind of the wave crest, where the boundary layer thickens, we find a large positive turbulent stress, especially behind the steep waves, which is on average 1.46 times larger than that of the flat waves, within a dimensionless height of $k_p\zeta = 0.5$, corresponding to a downward momentum flux with u' and w' of opposite sign. For both groups, we observe a region of negative turbulent stress (upward flux) near the surface on the upwind phase and above the crest, suggesting that the airflow tends to stabilize and become less turbulent as it approaches the wave crest, with a ratio of positive to negative turbulent stress of 3.8 for the steep waves. These observations are in qualitative agreement with the results of Buckley and Veron (2016), who attributed the 'phase-locked jet

of turbulence' to sporadic airflow separation events that are sufficiently intense to dominate the average, whereby high shear layers intermittently detach from the crest of steep waves. Interestingly, these low stress regions extend beyond the height of the inner layer. However, the portion that is outside the inner layer, extends farther upwind for the flat waves (figure 5.4, panel a), compared to that for the steep waves, where it remains concentrated above the crest. Since we expect less relaminarization over the upwind face of flat waves compared with steep waves, this result suggests that low turbulent stress should not necessarily be associated with relaminarization of the airflow. This departs from the results of Buckley (2015). The mean vertical profiles of the turbulent fluxes show that below $k_p\zeta \sim 0.25$ the turbulent flux exceeds the total flux above the steep waves, while for the flat waves it is less than 1. This is consistent with the results of Buckley and Veron (2019) and Yousefi et al. (2020) that the contribution of turbulent stress to wind stress increases with wind speed. Near the surface, within the mean inner layer, the turbulent flux drops to zero for both groups and converges to the total flux at a height of about $k_p\zeta \sim 1.5$.

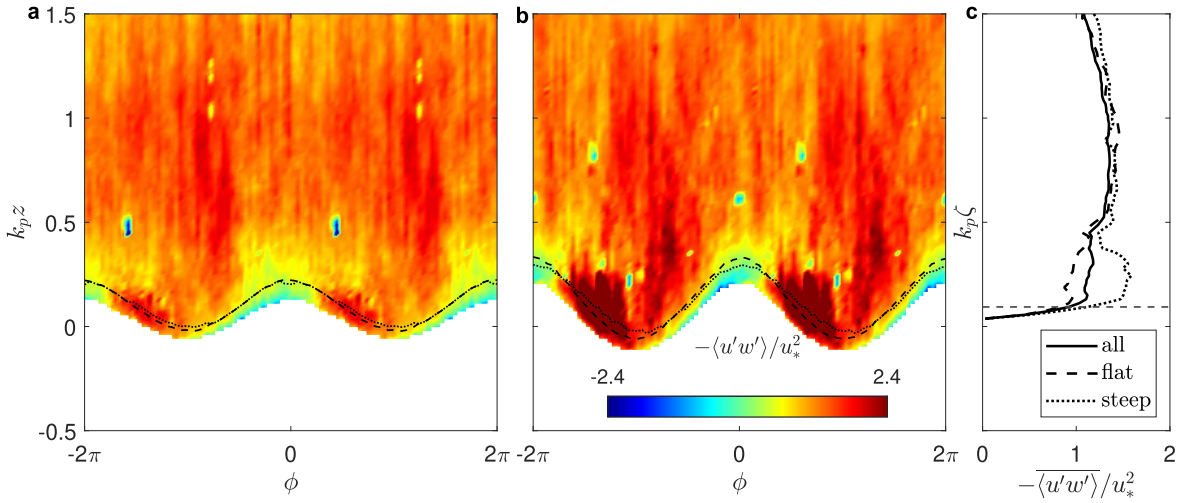

Figure 5.4: Phase-averaged (48 bins) turbulent stress for **a** flat waves with $ak < 0.155$ and **b** steep waves with $ak \geq 0.155$. **c** Total mean (for all phases) turbulent stress $-\overline{\langle u'w' \rangle}/u_*^2$. Dotted line indicates the inner layer, dashed line indicates its mean.

As in Tenhaus et al. (2024), we compute the phase-averaged viscous stress for the different groups, shown in figure 5.5. For all three cases, the viscous stress has a maximum at the wave crest and a minimum downwind of it. The stresses are equal just (upwind) of the crest, while they differ the most downwind of it, where the steeper waves show the lowest viscous stress estimates, coinciding with the sharp decrease in airflow velocity caused by sheltering, and the standard deviation peaks just where the viscous stress decreases rapidly. In general, the standard deviations are lower for the flat and steep waves, as expected after partitioning waves with similar characteristics.

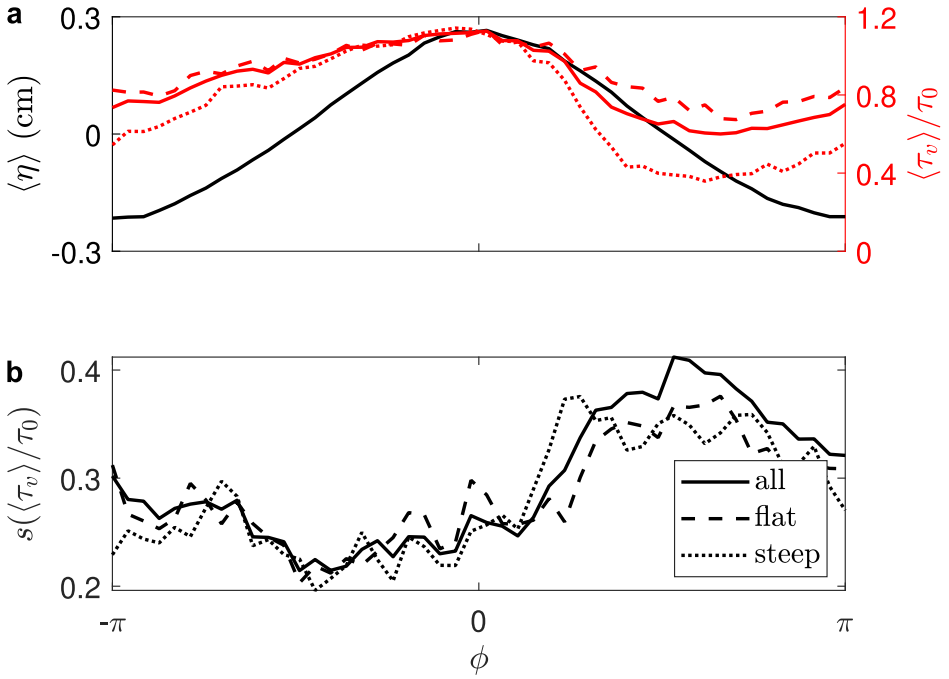

Figure 5.5: **a** Phase-averaged (48 bins) surface elevations and viscous stresses $\tau_v = \mu\,(\partial u/\partial\zeta + \partial w/\partial x)$ normalized by the total stress $\tau_0 = \rho u_*^2$ for all, flat, and steep waves partitioned by a cutoff of 0.155. **b** Standard deviations of viscous stresses normalized by the total stress.

5.4.3 Influence of wave slope on instantaneous turbulent velocity

While in figure 5.4 the turbulent stress is calculated before the phase-averaged velocities are divided into different groups so that

$$\langle u'w'\rangle_{f,s} = \frac{1}{N_{f,s}}\sum_{n=1}^{N_{f,s}}(u-\langle u\rangle)_n(w-\langle w\rangle)_n, \tag{5.2}$$

where the subscript f stands for flat waves with $ak < 0.155$ and s for steep waves with $ak \geq 0.155$, the influence of the wave slope partitioning on the instantaneous turbulent horizontal velocity u' is now investigated. Therefore, the phase-averaged velocity $\langle u\rangle_{f,s}$ for the flat and steep waves, respectively, is subtracted from an instantaneous field

$$u'_{f,s} = u - \langle u\rangle_{f,s}. \tag{5.3}$$

Figure 5.6 shows an example of the instantaneous horizontal velocity u plotted in a frame of reference moving at the wave speed, where the airflow separates behind the wave crest, causing a large decrease in velocity and a layer of high vorticity (defined as positive in the clockwise direction) that detaches from the surface. This results in a negative turbulent velocity behind the wave crest, regardless of whether the average of the flat or steep waves is used (not explicitly shown here), up to -2.6 m/s subtracting the phase-averaged velocity of all waves. The difference between using

the phase-averaged velocity of the flat and steep waves shows good overall agreement, except for the region behind the wave crest where we find a maximum difference of -1.15 m/s, with the average of the flat waves resulting in higher turbulent values. This result demonstrates that for airflow separation events, i.e., higher wind speeds and steeper waves, the partition is much more important to obtain reliable estimates of turbulence, and that extracting turbulent quantities embedded in the periodicity of the wave-coherent motions is non-trivial.

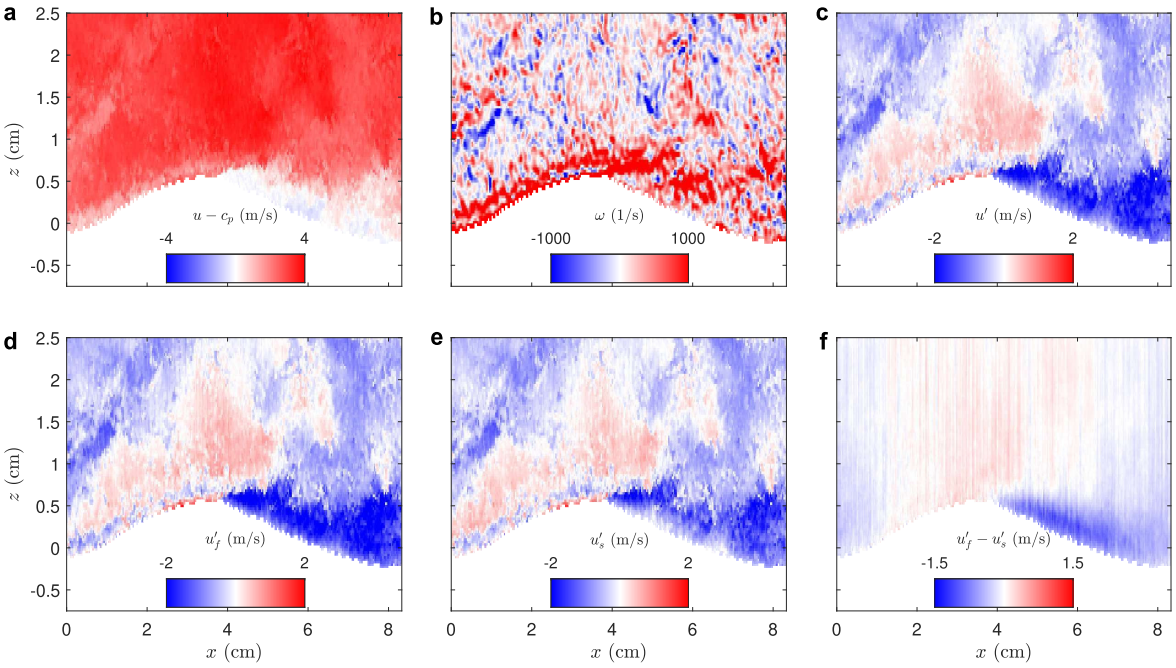

Figure 5.6: **a** Instantaneous horizontal velocity in a frame of reference moving at the peak intrinsic wave speed and **b** vorticity. Turbulent horizontal velocity obtained after subtracting the phase average for **c** all waves, **d** flat waves, **e** steep waves from the instantaneous field. **f** Difference of turbulent horizontal velocity obtained after subtracting the phase average for the flat and steep waves, respectively, from the instantaneous field.

5.4.4 Influence of wave slope on viscous forces

Following Buckley et al. (2020), we can compute the wind input term from the viscous force S_v into surface current (wind drift) S_{vc} and wave growth S_{vw} by decomposing the surface viscous stress τ_v and the horizontal surface velocity u_s into mean and wave-coherent components

$$\begin{aligned} S_v &= \overline{\tau_v u_s} \\ &= S_{vc} + S_{vw} \\ &= \bar{\tau}_v \bar{u}_s + \overline{\tilde{\tau}_v \tilde{u}_s} \end{aligned} \tag{5.4}$$

for the flat and steep waves to investigate the influence of the wave slope partitioning. The surface velocity u_s is obtained by linear extrapolation within the viscous sublayer

(probably a bit overestimated) of the phase-averaged horizontal velocity $\langle u \rangle$ at each phase bin (48 bins in total). The wave-coherent viscous stress $\tilde{\tau}_v$ and the surface velocity $\tilde{u}_s$ are then obtained by subtracting the mean from the phase average. Figure 5.7 shows the results for mean wave slopes of all $ak = 0.11$, flat $ak = 0.06$, and steep $ak = 0.20$ waves. With increasing wave slope, the contribution to waves increases while the contribution to currents decreases. These results show a good agreement with those of Buckley et al. (2020), especially for small ak, but increasingly depart from their results as the waves get steeper. Note that as the slope of the waves increases, the relative viscosity effects become less significant and the form drag dominates the total surface stress, whereas Buckley et al. (2020) found that for small slopes of $ak \sim 0.1$, 35 % of the total energy to the surface comes from the viscous forces. However, at these small slopes, most of the viscous input term contributes to surface currents rather than wave growth.

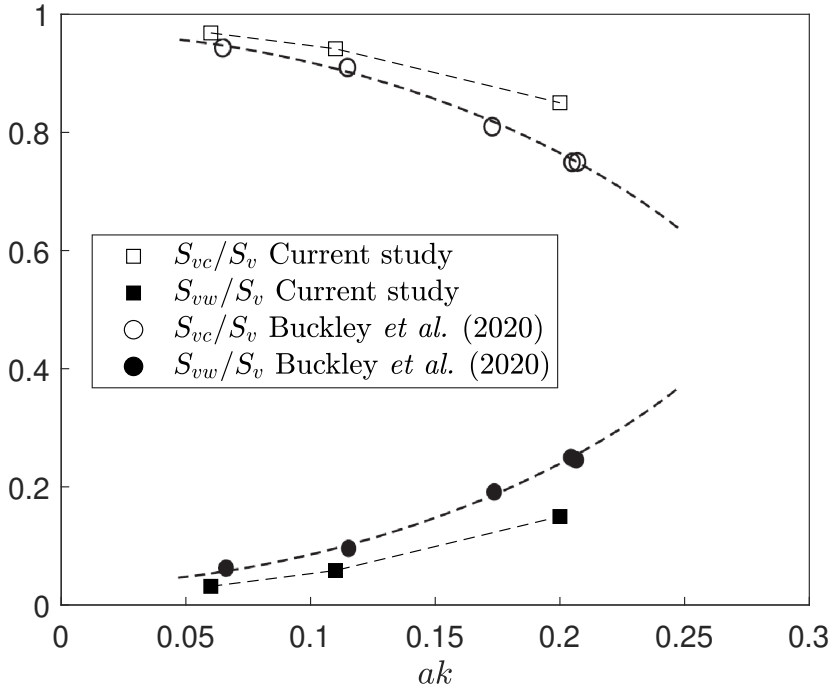

Figure 5.7: Wind input terms from viscosity contributing to currents S_{vc} and waves S_{vw} normalized by the total viscous forcing S_v for flat, all, and steep waves, respectively, plotted onto the observations from Buckley et al. (2020).

5.5 Summary and Conclusions

In this paper, we have presented high-resolution PIV measurements of the airflow above wind-generated surface waves, combined with LIF wave imagery. We focused on a particular wind-wave condition and were able to obtain individual wave characteristics, e.g., wave slope and asymmetries, thanks to the LIF measurements.

Dividing the waves into two different groups using the maximum of the normal distribution of the wave slope resulted in two conditions (flat and steep waves) without changing the wind speed.

We found that, in general, instantaneous and phase-averaged quantities such as horizontal velocity and turbulent stress are qualitatively consistent for both groups and do not deviate much from averages using all waves. The phase-averaged viscous stress is even the same just upwind of the crest. However, downwind of the crest, where the airflow is sheltered and occasionally separates from the surface, the groups behave differently, with the steeper waves showing a significant drop in viscous stress and larger turbulence.

The results highlighted that the extraction of turbulent quantities is non-trivial, since the continuous change of wave profiles in space and time leads to periodic wave-coherent motions. This raised the question of (re-)defining turbulence (see also Thais and Magnaudet (1995)). Waves come in groups, and the groupiness depends on the width of the spectrum. For typical wind-sea conditions (with a JONSWAP spectrum), the mean distance between two consecutive groups of high waves is approximately seven (Holthuijsen, 2007; Janssen, 2009). We propose that the periodicity in groups should be excluded from the definition of turbulence, rather than the average of all individual waves.

Using the large-field-of-view spatial snapshots (LIF), the role of individual wave properties such as steepness, asymmetry, and skewness will be used in future work to parameterize the observed air and water dynamics. In addition, simultaneous air- and water-side measurements will provide clarity on how much energy goes into wind drift currents from breaking and non-breaking waves (airflow separating vs. non-separating waves).

5.6 Supplementary Material

5.6.1 Phase-averaged horizontal velocity higher wind speed

Previously, by isolating two wave slope partitions within one experiment, we were able to assess the affects of wave slope on the airflow dynamics, with constant wind speed. Here, by considering an ensemble of small wave slope results at a higher wind speed, we are able to vary wind speed without varying wave slope, therefore isolating the influence of wind speed alone on the dynamics. Figure 5.8 compares the phase-averaged horizontal velocity of figure 5.3, panel b for flat waves with $ak < 0.155$ to a higher wind speed of $U_{10} = 9.5$ m/s (smaller wave age $c_p/u_* = 1.52$, higher mean wave slope $ak_p = 0.19$) using the same slope cutoff. The increase in wind speed for the same range of wave slopes results in more sheltering downwind of the wave crest. The vertical profiles at the zero-up and -down crossings (see also figure 5.2 for their definition) of the normalized phase-averaged horizontal velocity for the lower (black) and higher (red) wind speeds are shown in panel c. Upwind of the wave crest, the

profiles of both wind speeds differ only near the surface because the reattachment of the airflow is less pronounced than at the lower wind speed. Downwind of the wave crest, the profiles already differ at a higher height due to the increased sheltering. In general, the difference between the profiles of the zero-up and -down crossings for each wind speed is almost similar. At a height of $k_p\zeta \sim 0.3$ all four profiles converge. The mean inner layer height increases with increasing wind speed.

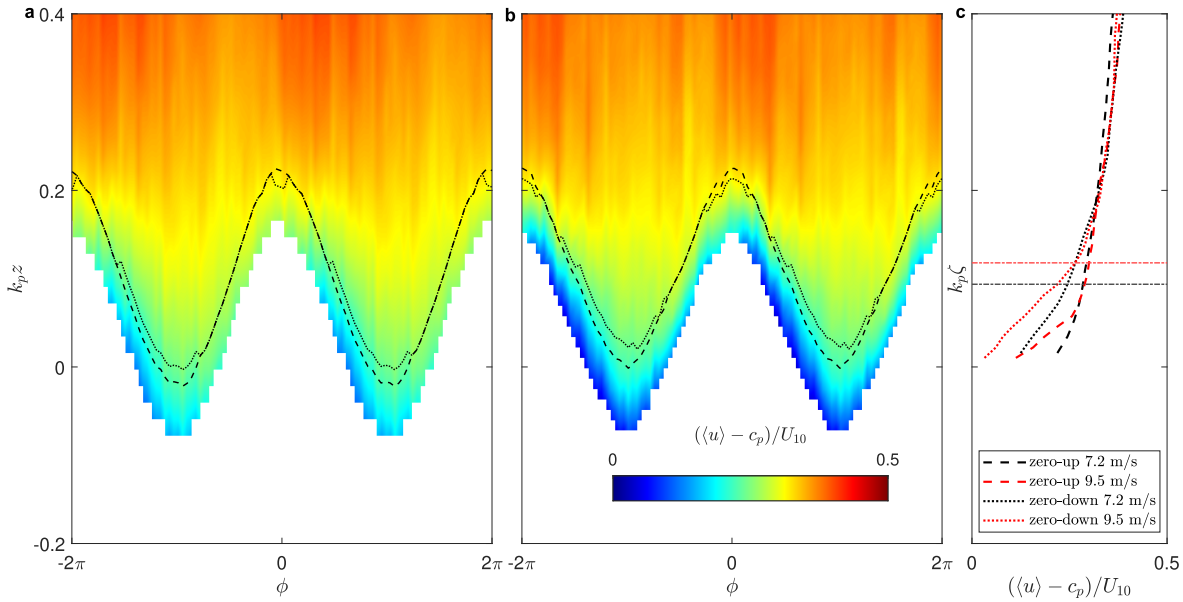

Figure 5.8: Phase-averaged (48 phase bins) horizontal velocity for flat waves with $ak < 0.155$ for a wind speed of **a** $U_{10} = 7.2$ m/s and **b** $U_{10} = 9.5$ m/s. **c** Vertical profiles of the wind speed at the zero-up and zero-down crossings, respectively, for both wind speeds. Red and black dashed dotted lines indicate the mean inner layer height for $U_{10} = 7.2$ m/s and $U_{10} = 9.5$ m/s, respectively.

5.6.2 Phase-averaged turbulent stress water side

The phase-averaged turbulent stress for the water side for $U_{10} = 7.2$ m/s is shown in figure 5.9. To normalize the stress, u_* is obtained from assuming that the stress is continuous across the air-water boundary layer. This allows us to use the air-side wind profile to estimate u_*. A positive turbulent stress is mainly found upwind of the wave crest, corresponding to the downward transport of positive horizontal momentum as in Melville et al. (2002) (opposite coordinate system). Downwind of the wave crest, a negative stress is dominating as is also observed in the instantaneous field in figure 4.8.

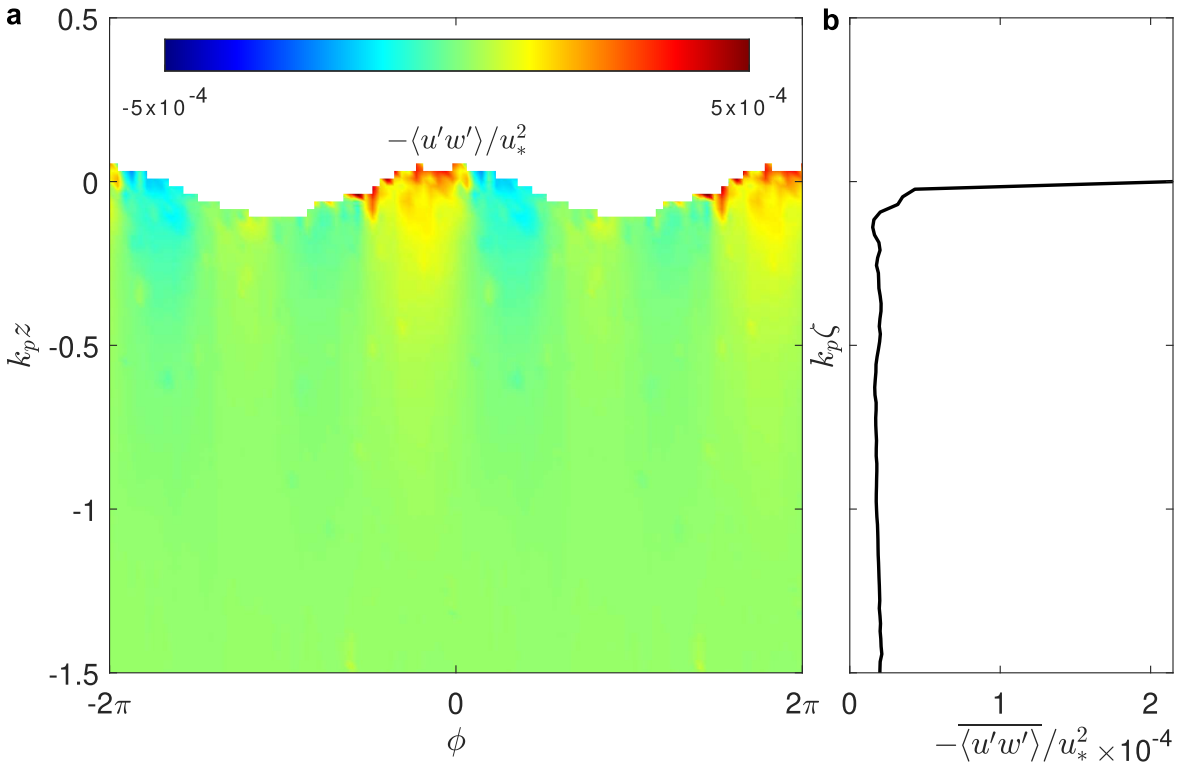

Figure 5.9: **a** Phase-averaged (48 phase bins) turbulent stress $-\langle u'w'\rangle/u_*^2$. **b** Total mean (for all phases) turbulent stress $-\overline{\langle u'w'\rangle}/u_*^2$.

6

Conclusions and Outlook

6.1 Summary

Motivated to gain a better understanding of the small-scale processes within the atmosphere-ocean boundary layer that control energy and momentum fluxes, the present thesis started with novel high-resolution in-situ airflow measurements over surface waves using particle image velocimetry (PIV) in the Odra Lagoon, Germany. Focusing on a peak wave age $c_p/u_* = 14.16$, wave slope $ak_p = 0.08$, and 10-m wind speed of 5.69 m/s, we observed small sheltering events downwind of wave crests. We directly found, for the first time in the field, a critical layer where the wind speed equals the wave speed and the wave-coherent vertical velocity is phase shifted. The phase shift was compared with linear theory and showed some agreement with Miles (1957) wave growth mechanism.

While limited to airflow measurements in the field, we were able to resolve near-surface velocities and viscous stresses above and below young wind-generated gravity waves at the University of Miami's SUSTAIN air-sea interaction facility, thanks to a novel combination of air-side and water-side high-resolution PIV and large-field-of-view laser-induced fluorescence (LIF). Strong along-wave modulations of both the air-side and water-side viscous stresses were directly observed for a peak wave age $c_p/u_* = 1.92$, wave slope $ak_p = 0.12$, and 10-m wind speed of 7.20 m/s. On the air side, the modulation exhibited a clear horizontal asymmetry accompanied by an increase in the standard deviation past the wave crest caused by airflow separation events. This is consistent with the measurements of Buckley et al. (2020). In contrast, the water-side phase-averaged viscous stress showed less asymmetry and the standard deviation peaked just at the crest, a possible result of microscale wave breaking (Siddiqui and Loewen, 2007). Although the air- and water-side experiments were not performed simultaneously but within the exact same wind-wave conditions, the large field of view allowed us to estimate individual wave properties and compare the instantaneous viscous and turbulent stresses for two consecutive waves with different slopes. For the steeper waves, we observed airflow separation and increased turbulence for both sides of the interface, which occurs in concert with a dramatic

drop in viscous stress below zero. In addition, simultaneous stereo PIV measurements provided estimates for the cross-tank component, albeit higher than expected.

Using the LIF wave images, we further focused on the influence of individual wave properties, such as wave slope and asymmetries, on viscous and turbulent stresses. By dividing the waves into two ensembles of different slopes (flat and steep waves), we found that both exhibit similar turbulent horizontal velocities, except for regions downwind of airflow separating crests. There, the magnitude of the turbulent quantities was strongly dependent upon the ensemble chosen to define them. The phase-averaged viscous stresses were the same for the flat and steep waves just upwind of the crests, and differed most downwind of the crests, due to the effects of individual sheltering events on the mean. With increasing wave slope, the contribution of viscous forces to wave growth increased, while the contribution to currents decreased, whereas the wind input term from viscosity becomes less significant.

6.2 Future Work

The techniques presented here have provided us with a unique and extensive high-resolution dataset for a range of different wind-wave conditions in the field and in the laboratory, including mechanically generated waves and non-neutral conditions that were outside the scope of the present work. The dataset should prove useful to further investigate the influence of waves on the dynamical coupling of the air-water viscous and turbulent boundary layers. However, future work must also consider different scenarios and use two-phase flow simulations (see, for example, Loft et al. (2023)) to parameterize the observed air and water dynamics.

While this thesis focused on two-dimensional velocity fields, the stereo PIV measurements already pointed to the three-dimensionality of the problem. Waves are horseshoe-shaped (Adrian, 2007), and both boundary layers are known to have important 3D turbulent structures that are likely to influence the coupling between the atmosphere and the ocean. In addition, the scales of turbulence in the laboratory differ from those in the field, where large eddies in the atmosphere feed energy to smaller eddies near the surface, leading to gustiness that has not (yet) been investigated in controlled laboratory experiments.

Once waves are of finite steepness, they grow from a pressure difference, whereby the pressure is higher on the upwind face and lower on the downwind face of the wave (this is described, for example, by Hristov et al. (2003)). The present work showed the contribution of Miles (1957) wave growth mechanism to the pressure perturbation in certain conditions. However, the competing roles of linear theory and wave-induced modulations of the turbulent stresses remain to be determined. In fact, it was highlighted that defining such wave-coherent motions is not a trivial task, especially for broadbanded wind waves. We suggest that the periodicity in groups should be included in the definition of turbulent quantities, rather than the average

of all individual waves.

The directly measured (non-separated) sheltering events presented throughout the thesis may be useful to better parameterize the sheltering coefficient, that is often used in numerical models and set between 0 and 1 (Donelan et al., 2012; Tan et al., 2023) (see also Janssen and Bidlot (2023) for a new definition). In general, understanding wave growth is important for sea state forecasting; measurements at high wind speeds are needed to better predict hurricanes.

Finally, simultaneous air- and water-side measurements using similar high-resolution two-dimensional techniques as those presented here, will provide clarity on how much energy goes into wind drift currents from breaking and non-breaking waves (airflow separating vs. non-separating waves).

Acknowledgements

This dissertation was supported by the Collaborative Research Centre TRR 181 "Energy Transfers in Atmosphere and Ocean" funded by the Deutsche Forschungsgemeinschaft (DFG, German Research Foundation) - Project number 27476265, for which I am sincerely grateful.

I would like to thank my supervisor, Marc Buckley, for giving me the opportunity. His extensive knowledge and expertise guided me through this work. The measurement campaigns with him were a pleasure and taught me a lot. Thank you also for sending me on the RV METEOR expedition M180 with a bunch of instruments that I had no idea I could handle. He was always supportive and his sense of humor kept me going through difficult times.

Thanks to my advisory committee members Carsten Eden, Martin Gade, Jeffrey Carpenter, and Anthony Bonfils. Thanks also to my colleague Malte Loft for all the discussions and good laughs.

Last but not least, I would like to thank my family for their endless love, even though they are always wondering when I will start working for real. Thanks also to my self-chosen Tohuus in Hamburg and now partly in Bielefeld, and to my friends, most of whom have been with me for more than half of my life.

References

Abu Rowin, W. et al. (2024). "High-resolution PIV measurement over wind-generated waves". In: *Experiments in Fluids* 65.5. 77. ISSN: 0723-4864. DOI: 10.1007/s00348-024-03815-y.

Adrian, R. J. (2007). "Hairpin vortex organization in wall turbulence". In: *Physics of Fluids* 19.4. 041301. ISSN: 1070-6631. DOI: 10.1063/1.2717527.

Ahlers, C. and Buckley, M. P. (2019). *Python scripts for sampling Gill anemometer and weather serial data*. DOI: 10.5281/zenodo.2548604.

André, M. A. and Bardet, P. M. (2015). "Interfacial shear stress measurement using high spatial resolution multiphase PIV". In: *Experiments in Fluids* 56.6. 132. ISSN: 0723-4864. DOI: 10.1007/s00348-015-2006-7.

Ayet, A. and Chapron, B. (2022). "The Dynamical Coupling of Wind-Waves and Atmospheric Turbulence: A Review of Theoretical and Phenomenological Models". In: *Boundary-Layer Meteorology* 183.1, pp. 1–33. ISSN: 0006-8314. DOI: 10.1007/s10546-021-00666-6.

Banner, M. L. (1990). "The influence of wave breaking on the surface pressure distribution in wind-wave interactions". In: *Journal of Fluid Mechanics* 211, pp. 463–495. ISSN: 0022-1120. DOI: 10.1017/S0022112090001653.

Banner, M. L. and Melville, W. K. (1976). "On the separation of air flow over water waves". In: *Journal of Fluid Mechanics* 77.4, pp. 825–842. ISSN: 0022-1120. DOI: 10.1017/S0022112076002905.

Banner, M. L. and Peirson, W. L. (1998). "Tangential stress beneath wind-driven air–water interfaces". In: *Journal of Fluid Mechanics* 364, pp. 115–145. ISSN: 0022-1120. DOI: 10.1017/S0022112098001128.

Banner, M. L. and Peregrine, D. H. (1993). "Wave Breaking in Deep Water". In: *Annual Review of Fluid Mechanics* 25, pp. 373–397. ISSN: 0066-4189. DOI: 10.1146/annurev.fl.25.010193.002105.

Banner, M. L. and Phillips, O. M. (1974). "On the incipient breaking of small scale waves". In: *Journal of Fluid Mechanics* 65.4, pp. 647–656. ISSN: 0022-1120. DOI: 10.1017/S0022112074001583.

Barnett, T. P. and Kenyon, K. E. (1975). "Recent advances in the study of wind waves". In: *Reports on Progress in Physics* Volume 38.6. DOI: 10.1088/0034-4885/38/6/001.

Belcher, S. E. and Hunt, J. C. R. (1993). "Turbulent shear flow over slowly moving waves". In: *Journal of Fluid Mechanics* 251, pp. 109–148. ISSN: 0022-1120. DOI: 10.1017/S0022112093003350.

Belcher, S. E. and Hunt, J. C. R. (1998). "Turbulent flow over hills and waves". In: *Annual Review of Fluid Mechanics* 30, pp. 507–538. ISSN: 0066-4189. DOI: 10.1146/annurev.fluid.30.1.507.

Belden, J. and Techet, A. H. (2011). "Simultaneous quantitative flow measurement using PIV on both sides of the air–water interface for breaking waves". In: *Experiments in Fluids* 50.1, pp. 149–161. ISSN: 0723-4864. DOI: 10.1007/s00348-010-0901-5.

Bonfils, A. F. et al. (2022). "Asymptotic interpretation of the Miles mechanism of wind-wave instability". In: *Journal of Fluid Mechanics* 944. A8. ISSN: 0022-1120. DOI: 10.1017/jfm.2022.441.

Bonfils, A. F. et al. (2023). "Flow-driven interfacial waves: an inviscid asymptotic study". In: *Journal of Fluid Mechanics* 976. A19. ISSN: 0022-1120. DOI: 10.1017/jfm.2023.906.

Bonmarin, P. (1989). "Geometric properties of deep-water breaking waves". In: *Journal of Fluid Mechanics* 209, pp. 405–433. ISSN: 0022-1120. DOI: 10.1017/S0022112089003162.

Bonmarin, P., Rochefort, R., and Bourguel, M. (1989). "Surface wave profile measurement by image analysis". In: *Experiments in Fluids* 7.1, pp. 17–24. ISSN: 0723-4864. DOI: 10.1007/BF00226592.

Buckley, M. P. (2015). "Structure of the Airflow above Surface Waves". Dissertation. University of Delaware. URL: http://udspace.udel.edu/handle/19716/17475.

Buckley, M. P. and Veron, F. (2016). "Structure of the Airflow above Surface Waves". In: *Journal of Physical Oceanography* 46.5, pp. 1377–1397. ISSN: 0022-3670. DOI: 10.1175/JPO-D-15-0135.1.

Buckley, M. P. and Veron, F. (2017). "Airflow measurements at a wavy air–water interface using PIV and LIF". In: *Experiments in Fluids* 58.11. 161. ISSN: 0723-4864. DOI: 10.1007/s00348-017-2439-2.

Buckley, M. P. and Veron, F. (2019). "The turbulent airflow over wind generated surface waves". In: *European Journal of Mechanics - B/Fluids* 73, pp. 132–143. ISSN: 09977546. DOI: 10.1016/j.euromechflu.2018.04.003.

Buckley, M. P., Veron, F., and Yousefi, K. (2020). "Surface viscous stress over wind-driven waves with intermittent airflow separation". In: *Journal of Fluid Mechanics* 905. A31. ISSN: 0022-1120. DOI: 10.1017/jfm.2020.760.

Callaghan, A. H., Deane, G. B., and Stokes, M. D. (2016). "Laboratory air-entraining breaking waves: Imaging visible foam signatures to estimate energy dissipation".

In: *Geophysical Research Letters* 43.21, pp. 11, 320–11, 328. ISSN: 0094-8276. DOI: 10.1002/2016GL071226.

Callaghan, A. H. and White, M. (2009). "Automated Processing of Sea Surface Images for the Determination of Whitecap Coverage". In: *Journal of Atmospheric and Oceanic Technology* 26.2, pp. 383–394. ISSN: 0739-0572. DOI: 10.1175/2008JTECHO634.1.

Carpenter, J. R., Buckley, M. P., and Veron, F. (2022). "Evidence of the critical layer mechanism in growing wind waves". In: *Journal of Fluid Mechanics* 948. A26. ISSN: 0022-1120. DOI: 10.1017/jfm.2022.714.

Carpenter, J. R., Guha, A., and Heifetz, E. (2017). "A Physical Interpretation of the Wind-Wave Instability as Interacting Waves". In: *Journal of Physical Oceanography* 47.6, pp. 1441–1455. ISSN: 0022-3670. DOI: 10.1175/JPO-D-16-0206.1.

Do, J., Wang, B., and Chang, K.-A. (2024). "Turbulence over young wind waves dominated by capillaries and micro-breakers". In: *Journal of Fluid Mechanics* 985. A22. ISSN: 0022-1120. DOI: 10.1017/jfm.2024.308.

Donelan, M. A. et al. (2012). "Modeling waves and wind stress". In: *Journal of Geophysical Research* 117.C11. ISSN: 0148-0227. DOI: 10.1029/2011JC007787.

Fairall, C. W. et al. (2003). "Bulk Parameterization of Air–Sea Fluxes: Updates and Verification for the COARE Algorithm". In: *Journal of Climate* 16.4, pp. 571–591. ISSN: 0894-8755. DOI: 10.1175/1520-0442(2003)016<0571:BPOASF>2.0.CO;2.

Funke, C. S. et al. (2021). "Pressure fields in the airflow over wind-generated surface waves". In: *Journal of Physical Oceanography* 51.11, pp. 3449–3460. ISSN: 0022-3670. DOI: 10.1175/JPO-D-20-0311.1.

Gent, P. R. and Taylor, P. A. (1977). "A note on 'separation' over short wind waves". In: *Boundary-Layer Meteorology* 11.1, pp. 65–87. ISSN: 0006-8314. DOI: 10.1007/BF00221825.

Grare, L., Lenain, L., and Melville, W. K. (2013a). "Wave-Coherent Airflow and Critical Layers over Ocean Waves". In: *Journal of Physical Oceanography* 43.10, pp. 2156–2172. ISSN: 0022-3670. DOI: 10.1175/JPO-D-13-056.1.

Grare, L., Lenain, L., and Melville, W. K. (2018). "Vertical Profiles of the Wave-Induced Airflow above Ocean Surface Waves". In: *Journal of Physical Oceanography* 48.12, pp. 2901–2922. ISSN: 0022-3670. DOI: 10.1175/JPO-D-18-0121.1.

Grare, L. et al. (2013b). "Growth and dissipation of wind-forced, deep-water waves". In: *Journal of Fluid Mechanics* 722, pp. 5–50. ISSN: 0022-1120. DOI: 10.1017/jfm.2013.88.

Hara, T. and Sullivan, P. P. (2015). "Wave Boundary Layer Turbulence over Surface Waves in a Strongly Forced Condition". In: *Journal of Physical Oceanography* 45.3, pp. 868–883. ISSN: 0022-3670. DOI: 10.1175/JPO-D-14-0116.1.

Holthuijsen, L. H. (2007). *Waves in oceanic and coastal waters*. Cambridge University Press. ISBN: 9780521860284.

Hristov, T. S., Miller, S. D., and Friehe, C. A. (2003). "Dynamical coupling of wind and ocean waves through wave-induced air flow". In: *Nature* 422.6927, pp. 55–58. ISSN: 0028-0836. DOI: 10.1038/nature01382.

Hsu, C.-T., Hsu, E. Y., and Street, R. L. (1981). "On the structure of turbulent flow over a progressive water wave: theory and experiment in a transformed, wave-following co-ordinate system". In: *Journal of Fluid Mechanics* 105, pp. 87–117. ISSN: 0022-1120. DOI: 10.1017/S0022112081003121.

Husain, N. T. et al. (2019). "Boundary Layer Turbulence over Surface Waves in a Strongly Forced Condition: LES and Observation". In: *Journal of Physical Oceanography* 49.8, pp. 1997–2015. ISSN: 0022-3670. DOI: 10.1175/JPO-D-19-0070.1.

Janssen, P. A. E. M. (2008). "Progress in ocean wave forecasting". In: *Journal of Computational Physics* 227.7, pp. 3572–3594. ISSN: 00219991. DOI: 10.1016/j.jcp.2007.04.029.

Janssen, P. A. E. M. (2009). *The Interaction of Ocean Waves and Wind*. Cambridge University Press. ISBN: 9780521465403.

Janssen, P. A. E. M. and Bidlot, J.-R. (2023). "Wind–Wave Interaction for Strong Winds". In: *Journal of Physical Oceanography* 53.3, pp. 779–804. ISSN: 0022-3670. DOI: 10.1175/JPO-D-21-0293.1.

Janssen, P. A. E. M. et al. (2001). "Impact and feedback of ocean waves on the atmosphere". In: *ECMWF Technical Memoranda* 341. DOI: 10.21957/c1ey8zifx.

Jeffreys, H. (1925). "On the formation of water waves by wind". In: *Proceedings of the Royal Society of London. Series A, Containing Papers of a Mathematical and Physical Character* 107.742, pp. 189–206. ISSN: 0950-1207. DOI: 10.1098/rspa.1925.0015.

Jessup, A. T., Zappa, C. J., and Yeh, H. (1997). "Defining and quantifying microscale wave breaking with infrared imagery". In: *Journal of Geophysical Research* 102.C10, pp. 23145–23153. ISSN: 0148-0227. DOI: 10.1029/97JC01449.

Kihara, N. et al. (2007). "Relationship between airflow at the critical height and momentum transfer to the traveling waves". In: *Physics of Fluids* 19.1. 015102. ISSN: 1070-6631. DOI: 10.1063/1.2409736.

Kitaigorodskii, S. A. and Donelan, M. A. (1984). "Wind-Wave Effects on Gas Transfer". In: *Gas Transfer at Water Surfaces*. Ed. by W. Brutsaert and G. H. Jirka. Dordrecht: Springer Netherlands, pp. 147–170. ISBN: 9789048183937. DOI: 10.1007/978-94-017-1660-4_14.

Kjeldsen, S. P. and Myrhaug, D. (1980). "Wave-Wave Interactions, Current-Wave Interactions and Resulting Extreme Waves and Breaking Waves". In: *Coastal*

Engineering 1980. Ed. by B. L. Edge. New York, NY: American Society of Civil Engineers, pp. 2277–2303. ISBN: 9780872622647. DOI: 10.1061/9780872622647.137.

Komen, G. J. et al. (1994). *Dynamics and Modelling of Ocean Waves*. Cambridge University Press. ISBN: 9780521577816.

Kudryavtsev, V. and Chapron, B. (2016). "On Growth Rate of Wind Waves: Impact of Short-Scale Breaking Modulations". In: *Journal of Physical Oceanography* 46.1, pp. 349–360. ISSN: 0022-3670. DOI: 10.1175/JPO-D-14-0216.1.

Kudryavtsev, V., Chapron, B., and Makin, V. K. (2014). "Impact of wind waves on the air–sea fluxes: A coupled model". In: *Journal of Geophysical Research: Oceans* 119.2, pp. 1217–1236. ISSN: 2169-9275. DOI: 10.1002/2013JC009412.

Kundu, P. K. and Cohen, I. M. (2008). *Fluid mechanics*. 4th ed. Amsterdam and Boston: Academic Press. ISBN: 0123737354.

Li, T. and Shen, L. (2025). "A theoretical study of the upper bound of surface elevation variance in the Phillips initial stage during wind-wave generation". In: *Journal of Fluid Mechanics* 1006. A8. ISSN: 0022-1120. DOI: 10.1017/jfm.2025.13.

Lighthill, M. J. (1962). "Physical interpretation of the mathematical theory of wave generation by wind". In: *Journal of Fluid Mechanics* 14.3, pp. 385–398. ISSN: 0022-1120. DOI: 10.1017/S0022112062001305.

Liu, X. and Duncan, J. H. (2003). "The effects of surfactants on spilling breaking waves". In: *Nature* 421.6922, pp. 520–523. ISSN: 0028-0836. DOI: 10.1038/nature01357.

Loft, M. et al. (2023). "Two-phase flow simulations of surface waves in wind-forced conditions". In: *Physics of Fluids* 35.7. 072108. ISSN: 1070-6631. DOI: 10.1063/5.0156963.

Longuet-Higgins, M. S. (1992). "Capillary rollers and bores". In: *Journal of Fluid Mechanics* 240, pp. 659–679. ISSN: 0022-1120. DOI: 10.1017/S0022112092000259.

Mastenbroek, C. et al. (1996). "Experimental evidence of the rapid distortion of turbulence in the air flow over water waves". In: *Journal of Fluid Mechanics* 318, pp. 273–302. ISSN: 0022-1120. DOI: 10.1017/S0022112096007124.

McWilliams, J. C., Sullivan, P. P., and Moeng, C.-H. (1997). "Langmuir turbulence in the ocean". In: *Journal of Fluid Mechanics* 334, pp. 1–30. ISSN: 0022-1120. DOI: 10.1017/S0022112096004375.

Melville, W. K. (1996). "The Role of Surface-Wave Breaking in Air-Sea Interaction". In: *Annual Review of Fluid Mechanics* 28, pp. 279–321. ISSN: 0066-4189. DOI: 10.1146/annurev.fl.28.010196.001431.

Melville, W. K., Veron, F., and White, C. J. (2002). "The velocity field under breaking waves: coherent structures and turbulence". In: *Journal of Fluid Mechanics* 454, pp. 203–233. ISSN: 0022-1120. DOI: 10.1017/S0022112001007078.

Miles, J. W. (1957). "On the generation of surface waves by shear flows". In: *Journal of Fluid Mechanics* 3.02, pp. 185–204. ISSN: 0022-1120. DOI: 10.1017/S0022112057000567.

Okuda, K., Kawai, S., and Toba, Y. (1977). "Measurement of skin friction distribution along the surface of wind waves". In: *Journal of the Oceanographical Society of Japan* 33, pp. 190–198. DOI: 10.1007/BF02109691.

Pein, J. and Staneva, J. (2024). "Eutrophication hotspots, nitrogen fluxes and climate impacts in estuarine ecosystems: A model study of the Odra estuary system". In: *Ocean Dynamics* 74.4, pp. 335–354. ISSN: 1616-7341. DOI: 10.1007/s10236-024-01607-w.

Peirson, W. L. (1997). "Measurement of surface velocities and shears at a wavy air-water interface using particle image velocimetry". In: *Experiments in Fluids* 23.5, pp. 427–437. ISSN: 0723-4864. DOI: 10.1007/s003480050131.

Phillips, O. M. (1957). "On the generation of waves by turbulent wind". In: *Journal of Fluid Mechanics* 2.05, pp. 417–445. ISSN: 0022-1120. DOI: 10.1017/S0022112057000233.

Phillips, O. M. (1977). *The dynamics of the upper ocean*. 2. ed. Cambridge monographs on mechanics and applied mathematics. Cambridge University Press. ISBN: 9780521214216.

Phillips, O. M. and Banner, M. L. (1974). "Wave breaking in the presence of wind drift and swell". In: *Journal of Fluid Mechanics* 66.4, pp. 625–640. ISSN: 0022-1120. DOI: 10.1017/S0022112074000413.

Pizzo, N. E., Deike, L., and Ayet, A. (2021). "How does the wind generate waves?" In: *Physics Today* 74.11, pp. 38–43. ISSN: 0031-9228. DOI: 10.1063/PT.3.4880.

Plant, W. J. (1982). "A relationship between wind stress and wave slope". In: *Journal of Geophysical Research* 87.C3, pp. 1961–1967. ISSN: 0148-0227. DOI: 10.1029/JC087iC03p01961.

Reul, N., Branger, H., and Giovanangeli, J.-P. (1999). "Air flow separation over unsteady breaking waves". In: *Physics of Fluids* 11.7, pp. 1959–1961. ISSN: 1070-6631. DOI: 10.1063/1.870058.

Reul, N., Branger, H., and Giovanangeli, J.-P. (2008). "Air Flow Structure Over Short-gravity Breaking Water Waves". In: *Boundary-Layer Meteorology* 126.3, pp. 477–505. ISSN: 0006-8314. DOI: 10.1007/s10546-007-9240-3.

Savelyev, I. B., Buckley, M. P., and Haus, B. K. (2020). "The Impact of Nonbreaking Waves on Wind–Driven Ocean Surface Turbulence". In: *Journal of Geophysical Research: Oceans* 125.1. ISSN: 2169-9275. DOI: 10.1029/2019JC015573.

Siddiqui, M. H. K. and Loewen, M. R. (2007). "Characteristics of the wind drift layer and microscale breaking waves". In: *Journal of Fluid Mechanics* 573, pp. 417–456. ISSN: 0022-1120. DOI: 10.1017/S0022112006003892.

Siddiqui, M. H. K. and Loewen, M. R. (2010). "Phase-Averaged Flow Properties Beneath Microscale Breaking Waves". In: *Boundary-Layer Meteorology* 134.3, pp. 499–523. ISSN: 0006-8314. DOI: 10.1007/s10546-009-9447-6.

Siddiqui, M. H. K. et al. (2001). "Simultaneous particle image velocimetry and infrared imagery of microscale breaking waves". In: *Physics of Fluids* 13.7, pp. 1891–1903. ISSN: 1070-6631. DOI: 10.1063/1.1375144.

Smeltzer, B. K. et al. (2019). "An Improved Method for Determining Near–Surface Currents From Wave Dispersion Measurements". In: *Journal of Geophysical Research: Oceans* 124.12, pp. 8832–8851. ISSN: 2169-9275. DOI: 10.1029/2019JC015202.

Stewart, R. H. and Joy, J. W. (1974). "HF radio measurements of surface currents". In: *Deep Sea Research and Oceanographic Abstracts* 21.12, pp. 1039–1049. ISSN: 00117471. DOI: 10.1016/0011-7471(74)90066-7.

Sullivan, P. P. and McWilliams, J. C. (2010). "Dynamics of Winds and Currents Coupled to Surface Waves". In: *Annual Review of Fluid Mechanics* 42, pp. 19–42. ISSN: 0066-4189. DOI: 10.1146/annurev-fluid-121108-145541.

Sullivan, P. P., McWilliams, J. C., and Melville, W. K. (2007). "Surface gravity wave effects in the oceanic boundary layer: large-eddy simulation with vortex force and stochastic breakers". In: *Journal of Fluid Mechanics* 593, pp. 405–452. ISSN: 0022-1120. DOI: 10.1017/S002211200700897X.

Sullivan, P. P., McWilliams, J. C., and Moeng, C.-H. (2000). "Simulation of turbulent flow over idealized water waves". In: *Journal of Fluid Mechanics* 404, pp. 47–85. ISSN: 0022-1120. DOI: 10.1017/S0022112099006965.

Sutherland, P. and Melville, W. K. (2013). "Field measurements and scaling of ocean surface wave–breaking statistics". In: *Geophysical Research Letters* 40.12, pp. 3074–3079. ISSN: 0094-8276. DOI: 10.1002/grl.50584.

Sutherland, P. and Melville, W. K. (2015). "Field Measurements of Surface and Near-Surface Turbulence in the Presence of Breaking Waves". In: *Journal of Physical Oceanography* 45.4, pp. 943–965. ISSN: 0022-3670. DOI: 10.1175/JPO-D-14-0133.1.

Suzuki, N. (2019). "On the physical mechanisms of the two-way coupling between a surface wave field and a circulation consisting of a roll and streak". In: *Journal of Fluid Mechanics* 881, pp. 906–950. ISSN: 0022-1120. DOI: 10.1017/jfm.2019.752.

Tan, P. et al. (2023). "Laboratory Wave and Stress Measurements Quantify the Aerodynamic Sheltering in Extreme Winds". In: *Journal of Geophysical Research: Oceans* 128.4. ISSN: 2169-9275. DOI: 10.1029/2022JC019505.

Tan, P. et al. (2025). "Wind–Wave Momentum Flux in Steep, Strongly Forced, Surface Gravity Wave Conditions". In: *Journal of Geophysical Research: Oceans* 130.1. ISSN: 2169-9275. DOI: 10.1029/2024JC021616.

Tenhaus, J. et al. (2024). "Viscous and turbulent stress measurements above and below laboratory wind waves". In: *Experiments in Fluids* 65.12. 174. ISSN: 0723-4864. DOI: 10.1007/s00348-024-03898-7.

Thais, L. and Magnaudet, J. (1995). "A triple decomposition of the fluctuating motion below laboratory wind water waves". In: *Journal of Geophysical Research* 100.C1, pp. 741–755. ISSN: 0148-0227. DOI: 10.1029/94JC02714.

Thais, L. and Magnaudet, J. (1996). "Turbulent structure beneath surface gravity waves sheared by the wind". In: *Journal of Fluid Mechanics* 328, pp. 313–344. ISSN: 0022-1120. DOI: 10.1017/S0022112096008749.

Thielicke, W. and Stamhuis, E. J. (2014). "PIVlab – Towards User-friendly, Affordable and Accurate Digital Particle Image Velocimetry in MATLAB". In: *Journal of Open Research Software* 2. DOI: 10.5334/jors.bl.

Toba, Y. (1973). "Local balance in the air-sea boundary processes". In: *Journal of the Oceanographical Society of Japan* 29, pp. 209–220. DOI: 10.1007/BF02108528.

Veron, F., Saxena, G., and Misra, S. (2007). "Measurements of the viscous tangential stress in the airflow above wind waves". In: *Geophysical Research Letters* 34.19. ISSN: 0094-8276. DOI: 10.1029/2007GL031242.

Wunsch, C. and Ferrari, R. (2004). "VERTICAL MIXING, ENERGY, AND THE GENERAL CIRCULATION OF THE OCEANS". In: *Annual Review of Fluid Mechanics* 36, pp. 281–314. ISSN: 0066-4189. DOI: 10.1146/annurev.fluid.36.050802.122121.

Young, I. R. (1999). *Wind generated ocean waves*. First edition. Vol. 2. Elsevier ocean engineering book series. Amsterdam et al.: Elsevier. ISBN: 0080433170.

Yousefi, K., Veron, F., and Buckley, M. P. (2020). "Momentum flux measurements in the airflow over wind-generated surface waves". In: *Journal of Fluid Mechanics* 895. A15. ISSN: 0022-1120. DOI: 10.1017/jfm.2020.276.

Yousefi, K., Veron, F., and Buckley, M. P. (2021). "Turbulent and wave kinetic energy budgets in the airflow over wind-generated surface waves". In: *Journal of Fluid Mechanics* 920. A33. ISSN: 0022-1120. DOI: 10.1017/jfm.2021.377.

Zappa, C. J., Asher, W. E., and Jessup, A. T. (2001). "Microscale wave breaking and air–water gas transfer". In: *Journal of Geophysical Research* 106.C5, pp. 9385–9391. ISSN: 0148-0227. DOI: 10.1029/2000JC000262.

Zavadsky, A. and Shemer, L. (2017). "Water waves excited by near-impulsive wind forcing". In: *Journal of Fluid Mechanics* 828, pp. 459–495. ISSN: 0022-1120. DOI: 10.1017/jfm.2017.521.